Order Number 9410176

Proton transport and auroral optical emissions

Shen, Deli, Ph.D.

University of Alaska Fairbanks, 1993

U·M·I
300 N. Zeeb Rd.
Ann Arbor, MI 48106

Proton Transport and Auroral Optical Emissions

A

THESIS

Presented to the Faculty

of the University of Alaska Fairbanks

in Partial Fulfillment of the Requirements

for the Degree of

DOCTOR OF PHILOSOPHY

By

Deli Shen, B.S., M.S.

Fairbanks, Alaska

September 1993

Proton Transport and Auroral Optical Emissions

by

Deli Shen

RECOMMENDED:

Prof. C.S. Deehr

Dr. D. Lummerzheim

Prof. R. Smith

Prof. K. Stamnes

Prof. H. Stenbaek-Nielsen

Prof. M.H. Rees, Chairman, Advisory Committee

Prof. John Morack, Head, Physics Department

APPROVED:

Dr. Paul Reichardt, Dean, College of Natural Sciences

E. Murphy, Chancellor's Faculty Assoc., Graduate Studies

23 August 1993

Date

Abstract

The hydrogen lines are the characteristic emissions of proton aurora and have been used to study the impact of protons upon the atmosphere. Observations of hydrogen emission on the long wavelength side of the unshifted lines were not explained by previous theories. To explain the observed optical emissions, a numerical code is developed to solve the one dimensional, steady state, linearly coupled transport equations of H^+/H in a dipole magnetic field. For the first time, the mirror force is included in the transport equations to produce backscattered particles which are responsible for emission at wavelengths longward of the unshifted lines. Both downward and upward particle intensities of H^+/H are calculated. The mirror reflectivities of energy and particles are defined, and their dependences on proton input spectra and pitch angle distributions are studied. The results show that the mirror reflectivity increases both with characteristic energy and with pitch angle of the input proton flux, but is more sensitive to angular distributions than to energy spectra. Energy deposition rate, ionization rate, H_α, H_β and Nitrogen First Negative bands emission rates and profiles are calculated.

Calculated fluxes of H^+/H and emission properties of Hydrogen Balmer lines are compared with a rocket measurement. The efficiency for production of the Balmer lines and the Nitrogen First Negative bands is obtained in terms of the energy input rate and the H^+ particle flux. A Doppler shift of about 3.0Å toward the blue for magnetic-zenith profiles of H_α is obtained, compared with observational results of 6.0 ± 2.0 Å. The calculated emissions on the red side of the unshifted hydrogen atomic emission lines when convolved with the instrumental function accounts for the observed emissions on the long wavelength side of the unshifted hydrogen Balmer lines.

Contents

List of Figures

List of Tables

Acknowledgements

This thesis has been completed under the steady, patient advice and encouragement of Professor M. H. Rees, my thesis advisor and the chairman of my graduate advisory committee. He has brought me into the fantastic auroral field, and given me as much freedom as I wished, yet guided me through a long period of hard work. He has provided financial and academic support and spent a great deal of time reviewing and correcting my thesis. His invaluable help is greatly appreciated.

I would like to thank the other committee members, Professors C.S. Deehr, R. Smith, K. Stamnes, H. Stenbaek-Nielsen, and Dr. D. Lummerzheim for their continuing help and valuable suggestions through out my thesis work. I would, especially, like to thank Dr. D. Lummerzheim for his help with computer programming and for carefully reviewing my thesis. Thanks also go to Professor Roger Smith for helping me analyze rocket data and for reviewing my thesis at short notice, and to Professor Dale Feist, the outside examiner.

I also would like to thank Dr. Øystein Lie-Svendsen for his help in computer programming and helpful discussions and Dr. Qilong Min for valuable discussions about numerical calculations. Their help was very important for the completion of my thesis. My gratitude also extends to many of my fellow graduate students in the Geophysical Institute and the Department of Physics who provided generous help and valuable discussions during the preparation of this thesis.

My work has been supported by National Aeronautics and Space Administration grant NAG-5-1097 and by National Science Foundation grant ATM9022197. The computation and printing were done on the UAF VAX computer and on a DEC work station. It is my pleasure to thank everyone in the UAF computing center for providing excellent service. I deeply appreciate Ms. Celia Rohwer at the Computer Service Center of the Geophysical Institute for her help in programming on the VAX. The thesis was typset using LaTeX.

Finally, I would like to thank my wife Lanying, my daughter Jing for their continuous support and encouragement, love and help in the thesis preparation.

Chapter 1

Introduction

Since the discovery of hydrogen lines in the auroral spectrum by Vegard (1939), the role of protons in auroral excitation has been a source of extensive study and speculation. The Doppler shifted hydrogen lines were, in fact, the only direct evidence for energetic particle excitation of the aurora before the era of rocket and satellite measurements. Systematic observations acquired by satellite-based energetic particle detectors have shown that, not infrequently, proton fluxes account for more than 90% of the auroral energy deposition rate over limited latitude segments of an orbit and that these fluxes are sufficiently large to produce intense auroras. But the development of a model for the behavior of proton excited aurora in magnetospheric substorm has been much slower than the development of electron auroral models. A detailed knowledge of the behavior of both electron and proton aurora and the possible interrelations between them is essential to the development of auroral theories.

A complete auroral theory should include two major processes: (1) how charged particles which are believed to originate from the solar wind penetrate the magnetosphere and are accelerated there; and (2) how these particles are transported into the ionosphere, deposit their energy and excite the observed optical emissions. This thesis focuses on the aspect of auroral theory concerned with particle transport. Specifically, the transport of protons and hydrogen atoms is investigated, and the optical emissions excited by the energetic protons and hydrogen atoms are computed.

1.1 Historical Review of Proton Aurora Theories

Studies of the aurora can be traced back to Aristotle's time. Since then, scientists have struggled to give a precise explanation of the aurora. Prior to Vegard's work, electrons were considered to be the principal auroral particles. After Vegard (1939) identified the Balmer lines in auroral spectra, Swings (1948) and Würm (1948) emphasized the role that heavy ions might play and theories that considered proton streams were developed by Störmer (1955), and by Bennett and Hulburt (1954a; 1954b). Current knowledge of the solar wind and the disturbed magnetosphere has shown that the early theories are no longer applicable.

Chamberlain (1961) studied ionization of the atmosphere due to proton impact and excitation of the optical emissions of hydrogen atoms. The first comprehensive study of the interaction of energetic protons with the atmosphere was carried out by Eather (1967b). Further work was done by Edgar et al. (1973, 1975) adopting a continuous slowing down approximation for the loss function and the analytical cross sections developed by Green and McNeal (1971). The latter did not fit the experimental cross sections in the low energy range. Using differential cross sections based on the binary encounter approximation (BEA) theory developed by Flannery (1971), Singh (1981) calculated the loss function and the secondary electron production from molecular nitrogen (N_2) by proton impact, and obtained a higher yield of low-energy secondary electrons than obtained by Edgar. However, Singh and Singhal's (1978) method still yields a lower secondary electron production rate at low energies compared with experimental results (Dose and Sele, 1975; Singh, 1981). In order to get better agreement with experimental results, Singh (1981) modified the elastic energy loss and calculated the loss function of molecular oxygen (O_2) and the secondary electron spectrum under proton impact. Agreement with experiments improved, but the calculation only applied to oxygen molecules, while in auroral excitation processes the most important neutral species is N_2 rather than O_2.

The next step in the analysis of proton aurora was taken by Rees (1982), who investigated the interaction of energetic protons with the atmosphere. He coupled the shape parameter of Rudd (1979) with the ionization rate to calculate production

rates of ejected electrons, and computed emission rates of hydrogen Balmer alpha and beta lines by considering the abundance of each constituent. After Rees' work, Van Zyl et al. (1984) calculated photon yields for proton aurora in a pure nitrogen atmosphere and discussed the effects of secondary electrons. It will be shown in section 4.4 that auroral characteristics in a nitrogen atmosphere differ from those derived in a real atmosphere, which better account for auroral observations.

Application of particle transport methods as developed by Jasperse and Basu (1982) provides the most realistic description of proton and hydrogen atom penetration of the upper atmosphere. Using linear transport theory, they developed coupled equations between proton and hydrogen atom streams. With some approximations to the coupling equations, they attempted to obtain an analytical solution. The solution is an infinite series which may or may not converge; the conditions under which the solution will converge were not provided. Several years later, Basu et al. (1987) showed that both the electron density profile and the peak altitude of the electron distribution computed by the linear transport theoretical approach to auroral proton precipitation compared reasonably well to that measured by the incoherent scatter radar, though some discrepancies exist. In 1990, Basu et al. (1990) solved the coupled transport equations using a numerical scheme. They compared the numerical results with the analytical solutions (Jasperse and Basu, 1982) and found large discrepancies in the particle fluxes computed by the two different schemes. The discrepancies in the energy deposition and ionization rates were small. The limitation in Basu's et al. (1990) numerical model is that the low energy cut-off is set at 1.0 keV, while the emission cross sections of hydrogen Balmer lines peak below 1.0 keV. The model can therefore not be applied to prediction of the optical emissions of hydrogen atoms. Extension of the energy range below 1.0 keV is difficult because of the evenly spaced energy grid in their model. For an evenly spaced energy distribution, the number of grid points would be over 2000 if the energy range 0.1 keV to 600.0 keV were to be covered with only three points falling below 1.0 keV.

1.2 Problems in Proton Aurora

The Doppler profile of hydrogen lines may be used as a tool for studying the distribution of protons in pitch angle and energy, but its implementation is hampered by lack of basic data. In the late sixties and early seventies, much effort was devoted to the study of the intensities and Doppler profiles of hydrogen lines in aurora. Apart from the very narrow hydrogen lines which have been recorded by Galperin (1963) and Johansen and Omholt (1963), few variations in the width of the lines have been observed, despite the fact that a great number of spectrograms with reasonable resolution have been obtained. Most observations show that the profiles do not vary appreciably from one aurora to another; the H_β line has about a 5Å displacement toward shorter wavelengths and the line width is about 16Å, regardless of the type of aurora. Magnetic-zenith hydrogen line profiles always show some emission on the long wavelength side of the unshifted line position. This red shifted emission extends to longer wavelengths than can be explained by the instrumental bandwidth alone. The observed emissions on the longward side of the unshifted line cannot be explained by collisional scattering of low energy protons either, as a simple wave-mechanical treatment of ion scattering (von Engel, 1965) shows that nearly all the collisional scattering of 1.0 keV protons by atmospheric constituents will deviate from forward scattering less than 0.2°. Multiple scattering of low energy protons could not explain the observed emissions on the long wavelength side of the unshifted emissions. The total number of collisions that H^+/H of energy about 10.0 keV could suffer on the way down is less than 10^4, and all these collisions occur near the bottom of the atmosphere. In a homogeneous atmosphere, the deflection caused by collisions should be in random directions, so the overall deflection of one particle is likely very small, not enough to deflect the particle back upward. Experimental results (Gao et al., 1990; Johnson et al., 1988, 1989) have also shown that protons or hydrogen atoms colliding with neutral species are scattered sharply in forward direction.

The red shift extends to a wavelength corresponding to protons travelling up the field lines with an energy component of 1-3 keV along the field lines. A likely explanation of the red shift is emission from particles that have been magnetically reflected and are returning back up the field lines. Bagariatskii (1958) suggested that

the red shifted emission may be due to protons being magnetically reflected, but was unable to reproduce the effect theoretically with the pitch angle distribution adopted by him. Eather (1966), taking into full account the convergence of the magnetic field, concludes that the mirroring indeed does provide the necessary effect, provided that the pitch angle distribution for the low energy protons is peaked around 70° — 90°, while recent rocket and satellite observations (Söraas et al., 1974; Miller and Whalen,1976; Urban, 1981) show the pitch angle distribution to be almost isotropic over the lower hemisphere.

One difficulty in dealing with proton transport is the beam spreading effect. Protons are confined along geomagnetic field lines by the Lorentz force, while hydrogen atoms produced through charge exchange processes of protons with the neutral atmosphere are free of this confinement. The hydrogen atoms will spread across field lines, and the spreading has been shown (Johnstone, 1972; Iglesias and Vondrak, 1974; Jasperse and Basu, 1982) to depend on the atmospheric structure, collision rate and primary particle energy and pitch angle, so it is not possible to develop an analytic expression for the beam spreading that can be included in the transport equations. Fortunately, as Iglesias and Vondrak (1974) showed, the spreading occurs mainly in the first few charge exchange processes, and can be ignored in the lower altitude region because of the small mean free path for the charge exchange collisions. The important processes of energy deposition, ionization, and optical emission, become dominant in the lower atmospheric region, so the main effect of spreading is to decrease the particle intensities in the center of the precipitating beam and to increase the beam width. In order to compare the model results with observations, these two effects can be taken into account by introducing a beam reduction factor in the one dimensional transport equations which will be given in section 2.2.

The purpose of this thesis is to develop a proton aurora model which can explain the observed optical emissions of hydrogen atoms. To explain the observed optical emissions of hydrogen atoms, the coupled transport equations for protons and hydrogen atoms have to be solved first. Based on the transport model of Jasperse and Basu (1982), a numerical model is developed to solve the one dimensional coupled transport equations that include a magnetic mirroring term to account for particles moving up magnetic field lines. The upward moving particles will excite emissions

on the long wavelength side of the unshifted hydrogen atom lines.

First, the particle intensities are calculated using an appropriate numerical scheme; then the energy deposition rates, ionization rates, and the optical emission rates of the hydrogen Balmer lines are calculated. The numerical scheme also gives the secondary electron production rate due to direct ionization processes. The line profiles of hydrogen atomic emissions due to proton precipitation are calculated and comparison is made between the calculated and observed line profiles. The numerical model will serve as a working model to explain the observed optical emissions of auroral hydrogen atomic lines.

Chapter 2

Transport Equations in a Magnetic Field

2.1 Main Collisional Processes

The behavior of protons penetrating the atmosphere differs fundamentally from that of electrons. Firstly, the probability of the deflection of protons in collisions with atmospheric particles is small enough to be neglected (Vallance Jones, 1974). Experiments have shown that for fast heavy particle projectiles, inelastic scattering cross sections are dominated by events in which the projectiles pass through the scattering region essentially undeflected (Rudd et al., 1985). Secondly, the probability of a fast proton capturing an electron to become a fast neutral atom introduces the need to consider the collisional interactions of such neutral particles. In the neutral state the particle is free from control by the magnetic field. Thus, in penetrating through the atmosphere, protons will alternate between spiral paths around the field lines and straight paths at an almost constant angle to the field direction. A schematic diagram of proton paths is shown in figure 2.1. Because of the smallness of collisional deflection the analysis of proton paths is simpler than for electrons, while the possibility of partial neutralization of the beam is a complication which must be taken into account.

Because the density of neutral species is much larger than that of the energetic protons and hydrogen atoms, only the interactions of protons and hydrogen atoms with neutral species are considered, and any interaction processes between

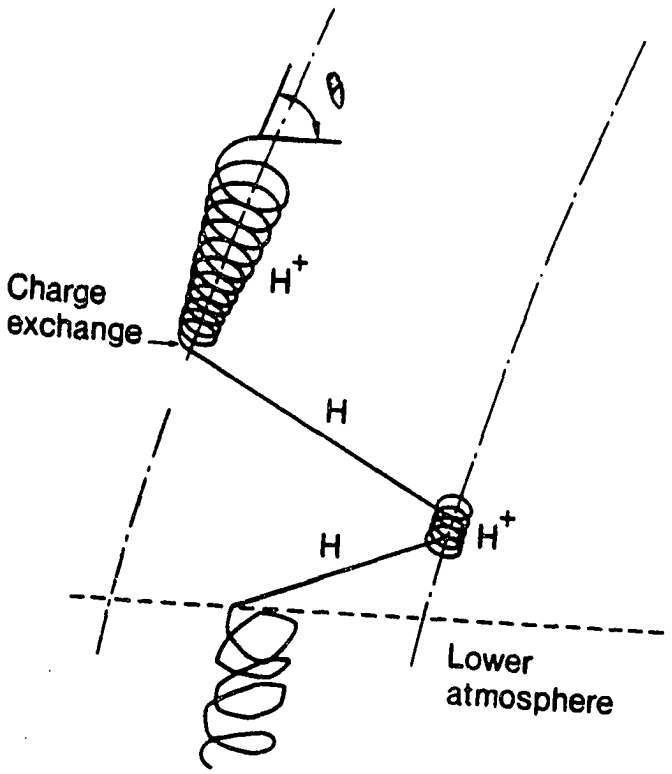

Figure 2.1: Path of incoming protons in the geomagnetic field. Protons spiral around the magnetic field lines with pitch angle θ, but once neutralized, the product hydrogen atom path remains undeflected.

protons and hydrogen atoms themselves, and interactions of H^+/H beam with ambient electrons and ions are neglected due to relative small densities of these particles compared with those of neutral species. The energy degradation of the H^+/H beam through various collisions with the neutral atmosphere is calculated. Due to the charge state conversion reactions, precipitating protons will become hydrogen atoms through charge capture processes, and hydrogen atoms then will convert to protons again through charge stripping processes, so, in fact, the proton transport problem is a two elements coupled transport problem, the coupling between protons and hydrogen atoms. The collisions of both H^+ and H with the atmospheric atoms and molecules have to be considered at the same time. The main collisional processes between proton and hydrogen and the neutral atmospheric species are the following.

(i) Charge exchange and stripping:

$$H^+ + M \longrightarrow H(nl) + M^+ \tag{2.1}$$

$$H + M \longrightarrow H^+ + M^{(*)} + e \tag{2.2}$$

(ii) Ionization :

$$H^+ + M \longrightarrow H^+ + M^{+n(*)} + ne \tag{2.3}$$

$$H + M \longrightarrow H(nl) + M^{+n(*)} + e \tag{2.4}$$

(iii)Excitation:

$$H^+ + M \longrightarrow H^+ + M^* \tag{2.5}$$

$$H + M \longrightarrow H(nl) + M^* \tag{2.6}$$

where M represents the major neutral species (N_2, O_2, and O), $M^{+n(*)}$ indicates that the neutral species may suffer multiple ionizations, but the probability of neutrals being multiply ionized is very small, so the measured ionization cross sections are considered to be from singly ionization process. Interactions between H^+ and H are not considered because their densities are much smaller than that of background species; $H(nl)$ indicates that the hydrogen atom may end up in excited states which are the source of the characteristic emissions in proton aurora; this will be dealt

with later in the optical emission chapter. In solving the transport equations, the only parameter that is needed is the intensity distribution of protons and hydrogen atoms, without worrying about the partition into individual states of the hydrogen atom.

2.2 Beam Spreading Effect

When auroral protons impact the atmosphere, charge exchange collisions with atmospheric particles result in energetic neutral hydrogen atoms. Protons can be confined along geomagnetic field lines by the Lorentz force, while the neutral hydrogen atoms produced through charge exchange are free of this confinement, and will spread across field lines as shown in figure 2.1. Such transverse spreading results in proton precipitation over a region wider than the original beam width above the atmosphere and consequently in a reduced proton intensity at the arc center. Transverse spreading of hydrogen atoms affects a one dimensional treatment of proton transport. Fortunately, the spreading occurs mainly at high altitude at the first few charge exchange processes, as has been shown by Iglesias and Vondrak (1974). Energy degradation at high altitude is a minor process. As protons penetrate further down to the altitude where energy degradation, ionization, and optical emission processes are important the beam spreading can be ignored because of the small mean free path for the charge exchange collisions. Therefore the only effect of spreading is to decrease the particle intensity in the center of the precipitating beam and to increase the beam width. Since it does not affect the transport, spreading can be taken into account by introducing a reduction factor in the one dimensional transport equations.

For narrow proton beam injected along a field line, transverse spreading has been calculated by a Monte-Carlo method (Davidson,1965) and by an approximate technique (Johnstone, 1972). For a proton arc of width 2W in the north-south direction, spreading has been derived by Iglesias and Vondrak (1974), and later modified by Jasperse and Basu (1982). A two-dimensional (Y-Z plane) sketch of a proton auroral arc of width $2W$ in the north-south direction (Y-axis) is illustrated in figure 2.2. The proton intensity distribution $f(\infty)$ is assumed to be homogeneous and isotropic over the arc of $2W$. Due to the spreading effect, the width of the

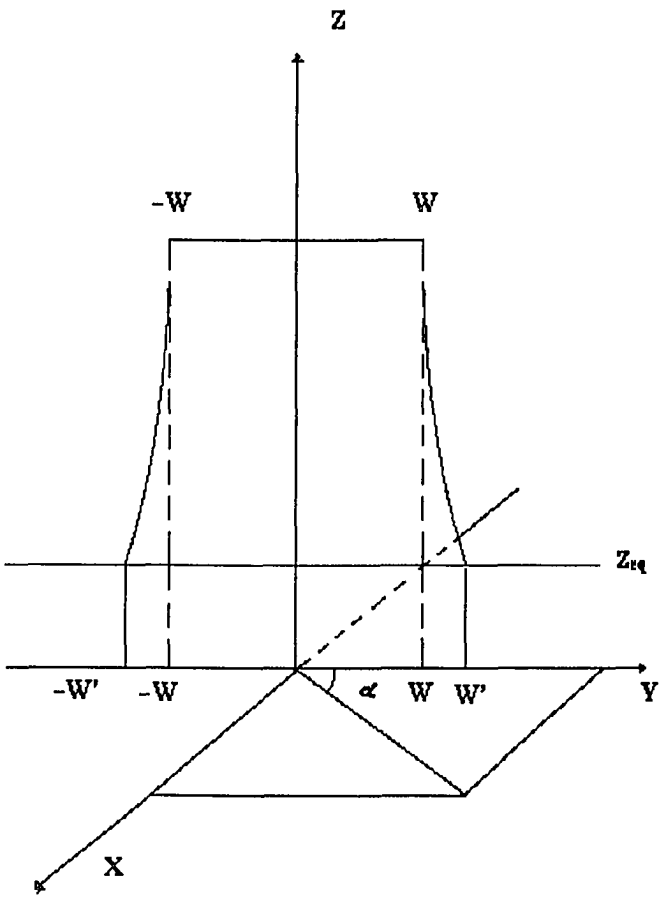

Figure 2.2: Spreading of a homogeneously distributed proton arc of width $2W$ in the north-south direction, with infinite extent in the east-west direction.

arc increases to $2W'$ by the time the precipitating particles reach the altitude Z_{eq}, defined as equilibrium altitude below which protons and hydrogen atoms are in equilibrium. No significant energy loss occurs above this altitude. At altitudes below Z_{eq}, the energy degradation processes are important while the spreading effect can be ignored due to the very small mean free path between collisions.

The particle distribution will no longer be homogeneous and isotropic over the whole precipitation region $2W'$. The inhomogeneous distribution at equilibrium altitude has been shown (Johnstone, 1972; Iglesias and Vondrak, 1974; Jasperse and Basu, 1982) to depend on the atmospheric structure, collision rate and primary particle energy and pitch angle. The change of the particle distribution at an

arbitrary point (X,Y) at equilibrium altitude Z_{eq} derived by Johnstone (1972) for the case of an isothermal atmosphere. Iglesias and Vondrak (1974) applied the formula to an auroral arc of width $2W$ in the north–south (Y–axis) direction and infinite in the east–west direction (figure 2.2) and obtained the particle intensity:

$$f(Z_{eq}, s, \theta) = \frac{f(\infty)}{2\pi H} \int_{Y-W}^{Y+W} dy \int_{-\infty}^{\infty} dx \frac{m \exp(s/H \tan\theta)}{m - 1 + \exp(s/H \tan\theta)} \qquad (2.7)$$

where W is the half-width of aurora arc, H is the scale height of the assumed isothermal atmosphere, $s = (x^2 + y^2)^{1/2}$ is the distance from point (x, y) to the center of the arc, θ is the pitch angle of energetic particles, $m = \sigma_{10}(E)/\sigma_{01}(E)$ is the ratio of the charge exchange cross section σ_{10} to charge stripping cross section σ_{01}, and is an energy dependent function. Substituting $x = y/\tan\alpha$, and integrating over y, the intensity becomes:

$$\begin{aligned} f(E_{eq}, Y, \theta) &= \frac{f(\infty)}{\pi} \int_0^{\pi/2} d\alpha \left\{ \left(1 - \frac{m}{m - 1 + \exp[(Y + W)/H \tan\theta \cos\alpha]} \right) \right. \\ &+ \left. \frac{W - Y}{|W - Y|} \times \left(1 - \frac{m}{m - 1 + \exp(|Y - W|/H \tan\theta \cos\alpha)} \right) \right\} \qquad (2.8) \end{aligned}$$

where Y is the distance from the center of the arc, α is the angle of the arbitrary point (X, Y) measured from the Y axis. In the current one dimensional transport model, only the intensity in the center of the arc ($Y = 0$) is needed, and the intensity reduction factor at the arc center, defined as the relative intensity distribution at the center of the arc is,

$$\frac{f(Z_{eq}, Y = 0, \theta)}{f(\infty)} = \frac{2}{\pi} \int_0^{\pi/2} d\alpha \left[1 - \frac{m}{m - 1 + \exp(W/H \tan\theta \cos\alpha)} \right] \qquad (2.9)$$

The dependence of the relative intensity reduction factor on arc width is shown in figure 2.3(a). The reduction factor is shown for various ratios of W to H and a fixed input energy $E_0 = 10.0$ keV. For an isotropic injection, the distribution becomes anisotropic at the center of the arc at altitude Z_{eq}. The flux at the center of the arc becomes increasingly isotropic and the reduction factor increases as the width of the arc increases. A scale height of 50 km is used for all subsequent calculations. Figure 2.3(b) gives the relative reduction of the particle distribution for various energies

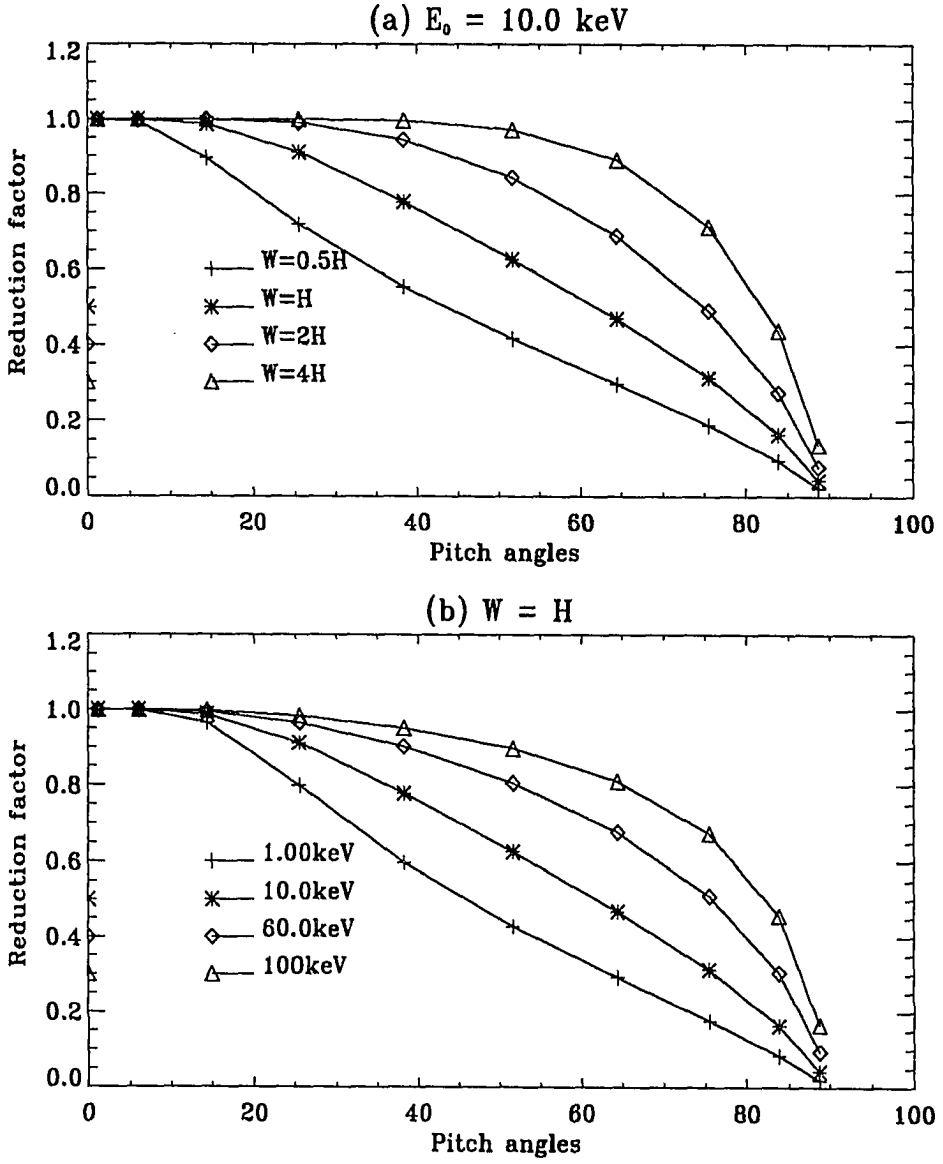

Figure 2.3: Angular redistribution of initially isotropic protons in an arc of width $2W$, (a) for various arc widths , (b) for various energies.

with a fixed arc width $W = H$. As the energy increases, the attenuation of the intensity at the arc center decreases and the distribution becomes more isotropic.

Integration of equation 2.9 over pitch angle gives the relative reduction of the flux under the center of the arc:

$$\frac{F(Z_{eq}, Y=0)}{F(\infty)} = 2\int_0^1 \mu\, d\mu \frac{f(Y=0, W, H, \mu)}{f(\infty)} \tag{2.10}$$

where $\mu = \cos\theta$ is the cosine of pitch angles. The total flux ratio for various arc widths and various energies is shown in figure 2.4 for an initially isotropic input flux. The reduction factor is more sensitive to the arc width than to energy. For an arc width ten times the scale height, the flux ratio approaches unity and is almost independent of the energy. For auroral arcs wider than about 1000 km, the spreading effect can be ignored, but for proton precipitation with peak energy around 10 keV, the flux ratio may change from about 0.5 to 0.9 when the arc width increases from 50 km to 500 km, so the transport code developed here is directly applicable to extended aurora. For narrow auroral arcs, a scaling factor depending on the width of auroral arc and the scale height of neutral atmosphere has to be included to account for the spreading effect caused by charge exchange processes when comparing the model with the observations.

2.3 Derivation of the General Transport Equations

As mentioned in the previous section, due to the repetitive conversions of H^+ into H in electron capture reactions, and of H into H^+ in ionization-stripping reactions, proton transport involves two coupled transport equations, one for protons and the other for hydrogen atoms. Collisions of both H^+ and H with the atmospheric atoms and molecules have to be considered simultaneously. Let $I_p(z, E, \mu)$ and $I_H(z, E, \mu)$ be the proton and hydrogen atom intensities in $z - E - \mu$ phase space. The Boltzmann equations for the respective intensities are

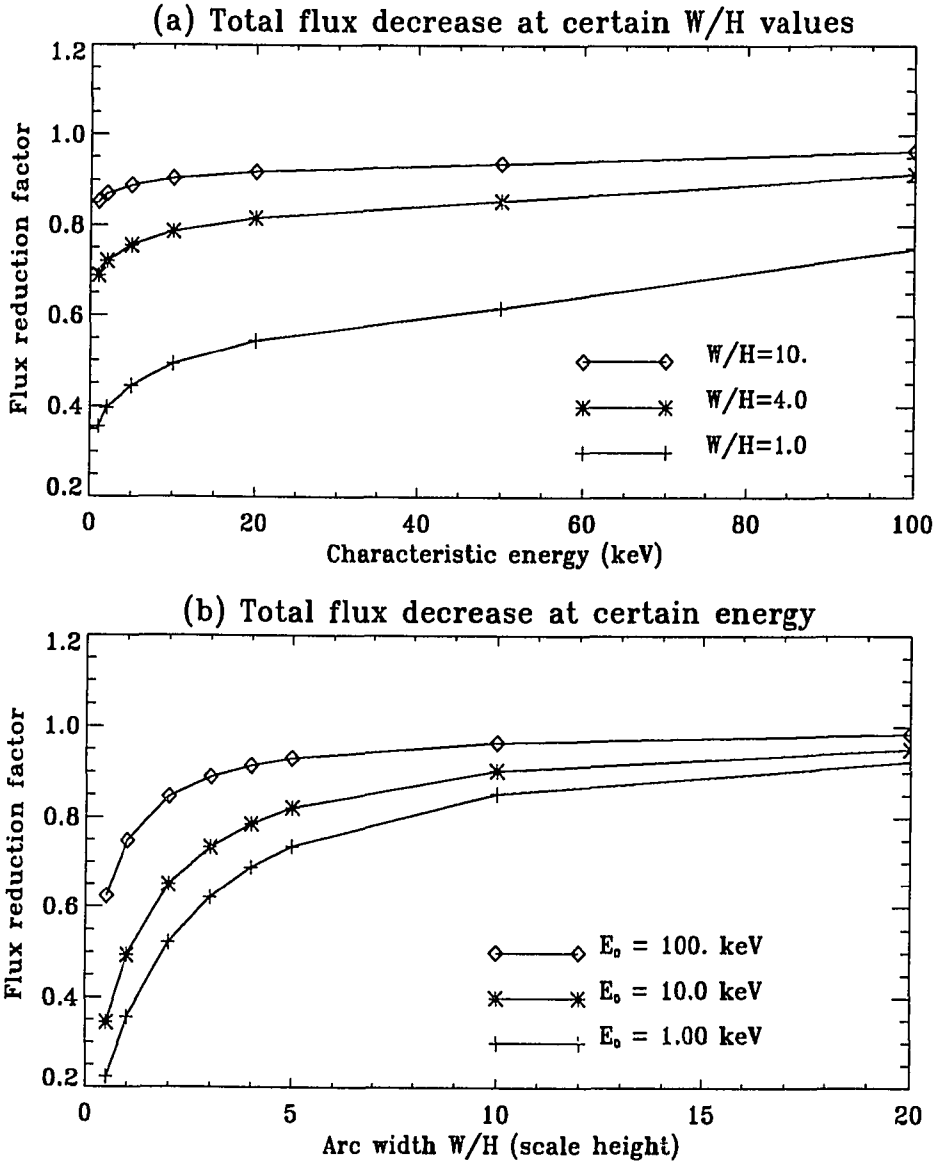

Figure 2.4: Fractional downward particle flux for various arc widths and energies, (a) energy dependence of flux reduction for various arc widths, (b) arc width dependence of fractional flux for different energies.

$$\frac{dI_p(z,E,\mu)}{dt} = \left(\frac{\delta I_p(z,E,\mu)}{\delta t}\right)_{coll} \tag{2.11}$$

$$\frac{dI_H(z,E,\mu)}{dt} = \left(\frac{\delta I_H(z,E,\mu)}{\delta t}\right)_{coll} \tag{2.12}$$

where z is the coordinate in the direction of the magnetic field as shown in figure 2.1, $dz/dt = \mu v$, with v the velocity of the projectile, and μ=cos θ is the cosine of the pitch angle θ. The intensities $I_p(z,E,\mu)$ and $I_H(z,E,\mu)$ are functions of altitude, energy, and pitch angle.

It takes a 10.0 keV proton about one second to travel from the top of the atmosphere to the end of its range. Most auroral observations (Söraas et al., 1974; Miller and Whalen,1976) show that proton precipitation is nearly invariant over time scales of the order of minutes. A steady state approximation is therefore adequate to study proton transport. In a steady state, the left hand side of equation 2.11 can be expanded into the partial form,

$$\frac{dI_p(z,E,\mu)}{dt} = \frac{\partial I_p(z,E,\mu)}{\partial z}\frac{dz}{dt} + \frac{\partial I_p(z,E,\mu)}{\partial \mu}\frac{d\mu}{dt} \tag{2.13}$$

In equation 2.13 the acceleration term has been omitted because it is assumed that the only force is the magnetic force which will only change the direction of the protons. The change of pitch angle with time can be calculated by assuming that the trajectory of the protons satisfies the first adiabatic invariant, that is:

$$E \sin^2\theta / B = \text{constant} \tag{2.14}$$

where E is the kinetic energy of the proton and θ the pitch angle, B is the magnitude of magnetic field. The conservation of the first adiabatic invariant is valid under the assumptions that there is no potential difference over distances of the order of the particle gyroradius and in a direction not parallel to the magnetic field, and that there are no oscillations in electric fields with frequencies greater than or of the order of the gyrofrequency. In the general case, the collisional processes will invalidate the conservation of the first adiabatic invariant, but in the forward scattering approximation, the conservation of the first adiabatic invariant can still be maintained. Neglecting any electric fields that may be present in the ionosphere, a proton penetrating into the atmosphere loses energy via collisional interactions

which are taken care of by the right hand sides of equations (2.11) and (2.12). The rate of change of the particle distribution functions due to collisional effects will be given later.

The magnetic field has no effect on the pitch angle of hydrogen atoms, so the left hand side of the transport equation for hydrogen atoms is:

$$\begin{aligned}\frac{dI_H(z,E,\mu)}{dt} &= \frac{\partial I_H(z,E,\mu)}{\partial z}\frac{dz}{dt} \\ &= \frac{\partial I_H(z,E,\mu)}{\partial z} v\mu \end{aligned} \tag{2.15}$$

The first term on the right hand side of equation (2.13) is simply $v\mu\frac{\partial I_p(z,E,\mu)}{\partial z}$, since $\mu = \cos\theta$, and $\frac{dz}{dt} = v\mu$. The conservation of the first adiabatic invariant, equation 2.14, gives:

$$E\sin^2\theta/B = E(1-\mu^2)/B = \text{constant}$$

or:

$$\frac{\partial\mu}{\partial z} = -\frac{(1-\mu^2)}{\mu}\frac{1}{2B}\frac{\partial B}{\partial z},$$

thus

$$\frac{d\mu}{dt} = \frac{\partial\mu}{\partial z}\frac{dz}{dt} = -v\mu\frac{(1-\mu^2)}{\mu}\frac{1}{2B}\frac{\partial B}{\partial z}$$

So the transport equations (2.11) and (2.12) become

$$\begin{aligned}\mu\frac{\partial I_p(z,E,\mu)}{\partial z} &= \frac{1}{v}\left(\frac{\delta I_p(z,E,\mu)}{\delta t}\right)_{coll} \\ &+ \frac{(1-\mu^2)}{2B}\frac{\partial B}{\partial z}\frac{\partial I_p(z,E,\mu)}{\partial\mu} \end{aligned} \tag{2.16}$$

$$\mu\frac{\partial I_H(z,E,\mu)}{\partial z} = \frac{1}{v}\left(\frac{\delta I_H(z,E,\mu)}{\delta t}\right)_{coll} \tag{2.17}$$

In general collision theory (McDaniel, 1989), the collision term $(\frac{\delta I_i}{\delta t})_{coll}$ is the sum of N integrals, where N is the number of different species present in the gas. Each of these integrals is designated by $B_i = (\frac{\delta I_i}{\delta t}) = \sum_j B_{i,j}$, where $B_{i,j}$ is the rate of change of the distribution function of species i caused by collisions with particles of species j as the trajectory of particles i is followed. The collision integral $B_{i,j}$ is obtained by calculating the difference between the rates of scattering of particles i into and

out of the volume element d^3v_i, due to collision with particles j. In the proton transport case, collisions of protons or hydrogen atoms with the background major neutral atmospheric species (N_2, O_2, O) are considered. Change of distribution functions of protons and hydrogen atoms due to collisions with the neutral species are calculated, while collisions between protons and hydrogen atoms themselves are neglected. The background neutral gas acts as a heat bath, and the change of its distribution function due to collisions is neglected. In z, E, μ phase space, the change in the distribution function at energy E, altitude z, and cosine pitch angle μ due to collisions with neutral species $n_s(z)$ can be written as (McDaniel, 1989):

$$\begin{aligned}\left(\frac{\delta I_p(z,E,\mu)}{\delta t}\right)_{coll} &= 2\pi v \sum_s n_s(z) \int dE' d\mu' \sum_j \sigma^j_{s,p}(E', \mu' \rightarrow E, \mu) I_p(z, E', \mu') \\ &+ 2\pi v \sum_s n_s(z) \int dE' d\mu' \sigma^{01}_s(E', \mu' \rightarrow E, \mu) I_H(z, E', \mu') \\ &- v \sum_s n_s(z) \sigma_{s,p}(E) I_p(z, E, \mu) \qquad (2.18)\end{aligned}$$

$$\begin{aligned}\left(\frac{\delta I_H(z,E,\mu)}{\delta t}\right)_{coll} &= 2\pi v \sum_s n_s(z) \int dE' d\mu' \sum_j \sigma^j_{s,H}(E', \mu' \rightarrow E, \mu) I_H(z, E', \mu') \\ &+ 2\pi v \sum_s n_s(z) \int dE' d\mu' \sigma^{10}_s(E', \mu' \rightarrow E, \mu) I_p(z, E', \mu') \\ &- v \sum_s n_s(z) \sigma_{s,H}(E) I_H(z, E, \mu) \qquad (2.19)\end{aligned}$$

where $\sigma_{s,p}(E)$, $\sigma_{s,H}(E)$ are total collision cross sections, including all elastic and inelastic cross sections, of proton and hydrogen atom with neutral species s, respectively; $n_s(z)$ is the number density of neutral species s at altitude z; $\sigma^j_{s,\beta}(E', \mu' \rightarrow E, \mu)$ is the double differential cross section for the j-type collision between species s and particle β (= H^+, H). The summation over j includes elastic, excitation and ionization collisions. μ is the cosine of the angle between particle velocity and the z axis, which is positive upward, and E is the particle energy. These total collision cross sections represent the rate at which H^+/H are scattered out of the current phase space volume . The second terms in equation (2.18) and (2.19) represent the rate of production due to the charge stripping and charge exchange processes, respectively. The first terms in equation (2.18) and (2.19) give the rate of change at which H^+/H are scattered into the current phase space volume. The transport equations then become

$$\mu\frac{\partial I_p(z,E,\mu)}{\partial z} = -\sum_s n_s(z)\sigma_{s,p}(E)I_p(z,E,\mu) + 2\pi\sum_s n_s(z)\int dE'd\mu'\sum_j \sigma^j_{s,p}(E',\mu'\rightarrow E,\mu)I_p(z,E',\mu') + 2\pi\sum_s n_s(z)\int dE'd\mu'\sigma^{01}_s(E',\mu'\rightarrow E,\mu)I_H(z,E',\mu') + \frac{(1-\mu^2)}{2B(z)}\frac{\partial B}{\partial z}\frac{\partial I_p(z,E,\mu)}{\partial \mu} \quad (2.20)$$

$$\mu\frac{\partial I_H(z,E,\mu)}{\partial z} = -\sum_s n_s(z)\sigma_{s,H}(E)I_H(z,E,\mu) + 2\pi\sum_s n_s(z)\int dE'd\mu'\sum_j \sigma^j_{s,H}(E',\mu'\rightarrow E,\mu)I_H(z,E',\mu') + 2\pi\sum_s n_s(z)\int dE'd\mu'\sigma^{10}_s(E',\mu'\rightarrow E,\mu)I_p(z,E',\mu') \quad (2.21)$$

The first term on the right hand side of equation (2.20) represents a sink of protons, the second term is the source from collisions of proton at higher energies with neutrals, and the third term is the source from collisions of hydrogen at higher energies with neutrals. The last term represents the mirror force derived earlier. The three terms on the right side in equation (2.21) represent quantities similar to the corresponding terms in equation (2.20).

Equations (2.20) and (2.21) are two coupled linear integro-differential equations that are not amenable to an analytical solution. The double differential cross sections $\sigma^j_{s,\beta}$(E',$\mu'\rightarrow$ E,μ) are not analytically integrable, and even for numerical solutions, some approximations are still needed. To solve the transport equations (2.20) and (2.21), the double differential cross sections have to be calculated first. In the electron transport problem, it is assumed (Lummerzheim, 1987) that the double differential cross sections can be represented by the product of a phase function and an energy differential cross section. The same approximation is adopted here, and it is assumed that the phase function of each collisional process is independent of the energy of the projectile particles. The integrations over angle and energy are then treated separately. The double differential cross section is written as:

$$\sigma^j_{s,\beta}(E',\mu'\rightarrow E,\mu) = \sigma^j_{s,\beta}(E'\rightarrow E)\Phi^j_{s,\beta}(\mu',\mu) \quad (2.22)$$

where $\sigma^j_{s,\beta}(E' \rightarrow E)$ is the energy differential cross section for type j collision of H^+/H with neutral species s, and $\Phi^j_{s,\beta}(\mu', \mu)$ is the scattering phase function.

2.4 Phase Function for H^+/H Elastic Scattering

Precipitating protons and hydrogen atoms deposit their energies into the neutral atmosphere through both elastic and inelastic collisions. For light projectile particles, such as electrons (Lummerzheim, 1987), phase functions for elastic scattering processes are very important. However, for protons, both theoretical (Nitz et al., 1987; Lorents and Aerth, 1965; Barat et al., 1973; and Marchi and Smith, 1965) and experimental work (Everhart, 1963; Baudon et al., 1968; and Nagy et al., 1971), has shown that the differential cross sections for elastic scattering collisions are sharply peaked in the forward direction, and that the cross sections drop sharply with increasing scattering angles. Gao et al. (1987, 1988) have measured differential cross sections for small angle elastic scattering in helium -rare gas collisions at keV energies, which showed that increasing the scattering angle from 0.05° to 0.5° decreases the cross section from $1.28\times\ 10^{-10}$ cm^2 to $5.15\times\ 10^{-13}$ cm^2 (Figure 2.5).

From figure (2.5), it can be seen that the elastic scattering angle is so small for rare gas collisions that approximating the phase function with a delta function is sufficient. Even though no experimental data have been found for H^+/H collisions with major atmospheric species, it is reasonable to infer from the rare gas data that the forward scattering approximation is very good for elastic scattering. Therefore, the phase function can be written as:

$$\Phi^{el}_{s,\beta}(\mu', \mu) = \delta(\mu' - \mu) \tag{2.23}$$

2.5 Phase Functions of H^+/H Inelastic Scattering

Angular differential scattering cross sections have been measured for inelastic interactions of H^+/H with the major species of the neutral atmosphere (Van Zyl et al., 1978; Fleischmann et al., 1974; Newman et al., 1986; Johnson et al., 1988; Gao

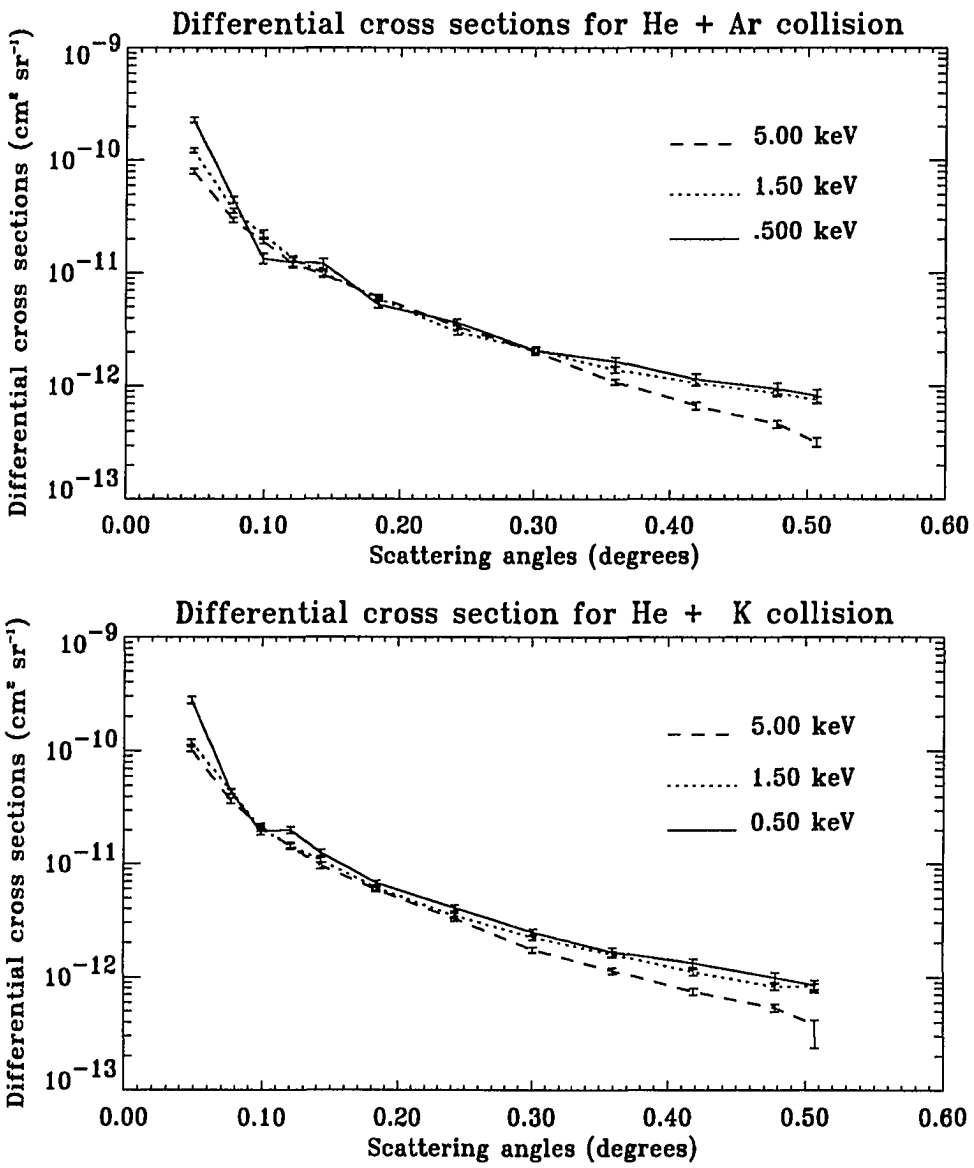

Figure 2.5: Experimental elastic scattering cross sections of rare gases by He impact (Gao, et al., 1987).

et al., 1990). The experimental results (figure 2.7 and 2.6) show that the cross sections are sharply peaked in the forward direction; thus, the phase functions for various inelastic scattering processes can also be approximated by delta functions. Equation (2.23) is , therefore, applied to both elastic and inelastic collisions.

2.6 Transport Equations Under Forward Scattering Approximation

It has been shown in the preceding sections that the phase functions for both elastic and inelastic scattering can be approximated by delta functions because the cross sections peak sharply in the forward direction. The double integrations in the transport equations reduce to single integrations with respect to the projectile energies which represents the energy degradation process. The singly differential cross section $\sigma_s(E' \rightarrow E)$ in the integration represents the probability of high energy (E') particles being scattered into the current energy bin (E), and if it can be represented by some analytical form, the integrations over energies in the transport equations would be able to be carried out either analytically or, at least, numerically. If the experimental data were available, the integrations could be implemented by some numerical scheme. For each reaction channel (excitation, ionization), the energy degradation cross section is different. However, experimental data for differential cross sections are not available for all discrete energy loss processes, and the singly differential cross sections are approximated by delta functions with an appropriate energy loss for each reaction channel. This reduces the transport equations to a numerically solvable problem. For continuous energy loss processes, such as ionization process, it will be shown later that the continuous losses can be approximated by using an average energy for secondary electrons.

For discrete excitation processes, excitation to each individual state will give a different energy loss, thus the singly differential cross section is just the sum of delta functions for all excited states. Due to the lack of experimental differential cross sections for each individual excited state, a two energy level model is used where the energy level difference is an average energy of some important states. The energy loss due to excitation is the energy level difference and the singly differential cross section become a delta function.

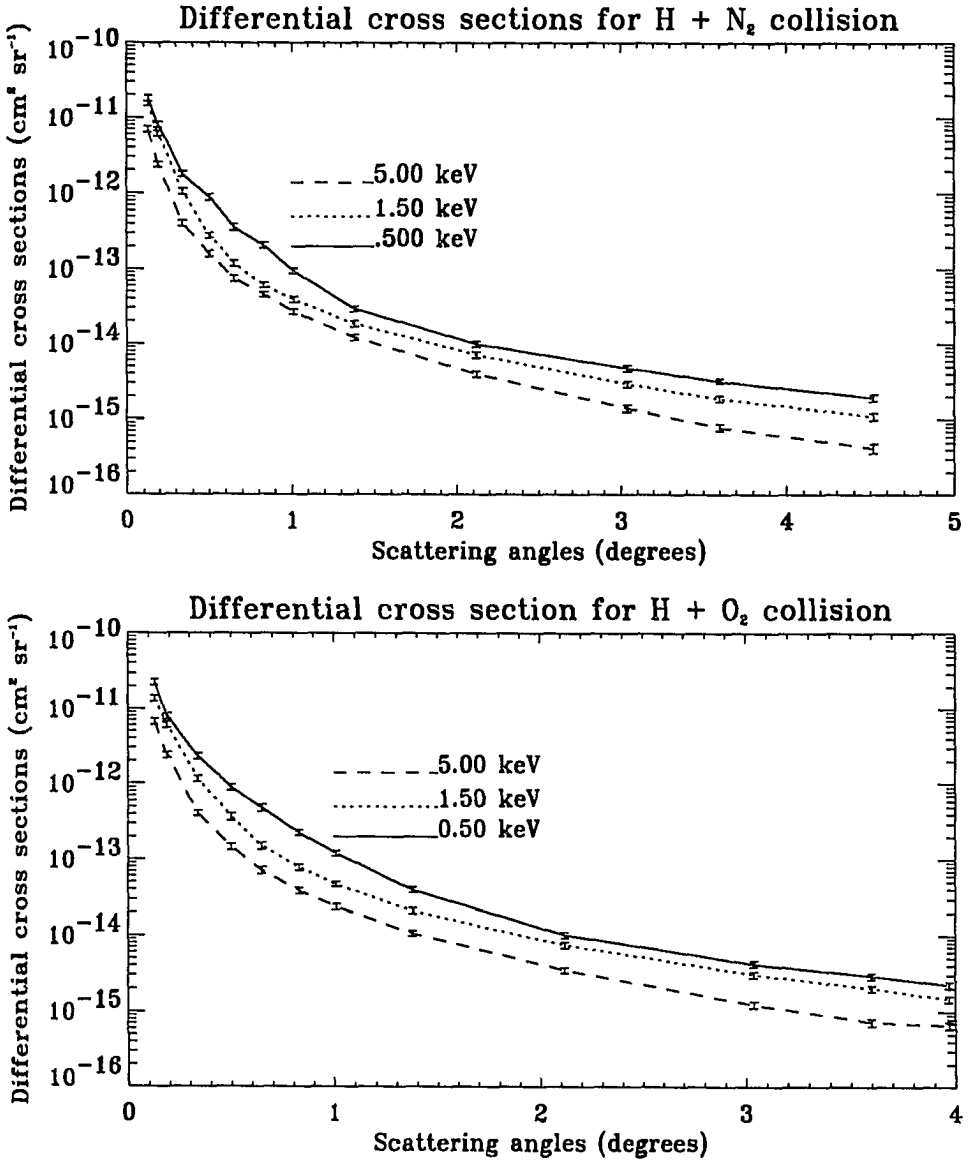

Figure 2.6: Angular differential cross sections for (a) H + N_2 (b) H + O_2, scattering at projectile energies 0.5, 1.5, and 5.0 keV (Johnson et al., 1988; and Newman et al., 1986).

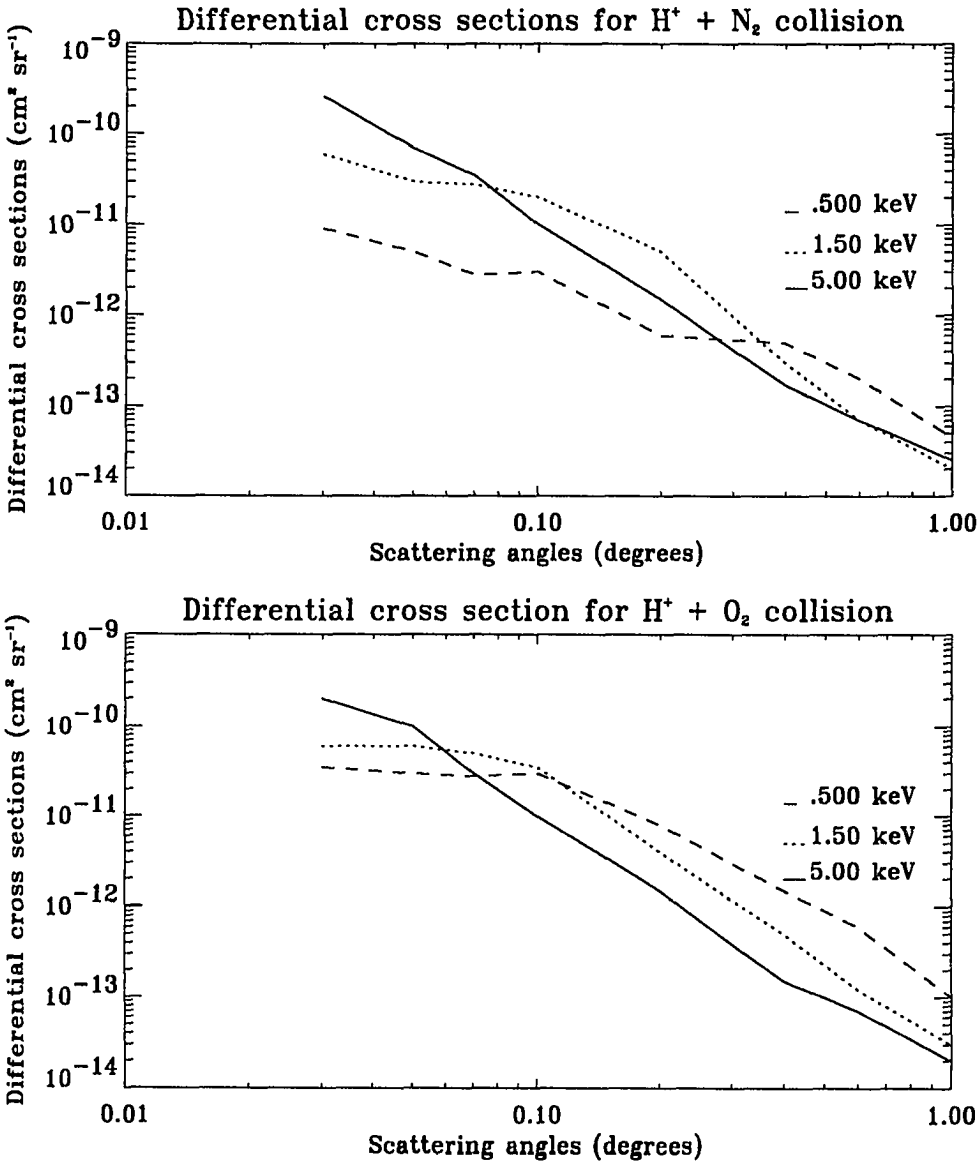

Figure 2.7: Angular differential cross sections for the charge-transfer collisions (a) $H^+ + N_2$, (b) $H^+ + O_2$ at 5.0, 1.5, and 0.5 keV projectile energies (Gao et al., 1990).

Table 2.1: Binding energy (in eV) and occupation number of N_2 and O_2 molecules

	N_2		O_2	
	I	N	I	N
$1\sigma_g$	409.9	2	543.5	2
$1\sigma_u$	409.9	2	543.5	2
$2\sigma_g$	37.3	2	40.3	2
$2\sigma_u$	18.78	2	25.69	2
$1\pi_u$	16.69	4	18.88	4
$3\sigma_g$	15.59	2	16.42	2
$1\pi_g$			12.07	2

For ionization processes, Rudd (1977, 1979) gives an empirical formula for the secondary electron production rate, which has the following exponential form:

$$\sigma(E_s, E_p) = 5\pi a_0^2 \alpha^3 \sum_i \frac{N_i I_H^2}{I_i^3} \frac{(T/I_i)^{\beta-1/2}}{4+(T/I_i)^{2\beta}} \exp\left(-\frac{\alpha E_s}{(I_i T)^{1/2}}\right) \qquad (2.24)$$

where E_s is the energy of secondary electrons, E_p is the energy of the incident energetic protons, $T = E_p/1836$, α and β are adjustable dimensionless parameters, N_i is the number of electrons in the target with binding energy I_i, I_H=13.6 eV, and a_0 is the radius of the first Bohr orbit. The binding energy I_i and the corresponding number of electrons in each subshell is shown in table 2.1 (Rudd et al., 1992) for nitrogen and oxygen molecules. Rudd (1979) tried to fit the experimental data with an empirical formula, and obtained the best fit by choosing $\alpha = 0.91$ and $\beta = 0.75$ for N_2 and O_2. The singly differential cross section calculated by equation 2.24 is shown in figure 2.8. From figure 2.8 it can be seen that the halfwidth of the differential cross section is on the order of 10.0 eV, much smaller than the energy grid size which will be given in the following chapter and that is used in solving the transport equations. It is therefore adequate to use delta functions to approximate the differential cross sections, and the energy loss corresponding to the average energy of the secondary electrons. The average energy of the secondary electron

can be calculated using:

$$\bar{E}_s(E_p) = \frac{\int_0^\infty E_s\, dE_s\, \sigma(E_s, E_p)}{\int_0^\infty dE_s\, \sigma(E_s, E_p)} \tag{2.25}$$

The integration of the numerator and denominator gives, respectively;

$$\int_0^\infty E_s\, dE_s\, \sigma(E_s, E_p) = 5\pi a_0^2 \alpha^3 \sum_i \frac{N_i I_H^2}{I_i^3} \frac{(T/I_i)^{\beta-1/2}}{4+(T/I_i)^{2\beta}} \times \frac{I_i T}{\alpha^2} \tag{2.26}$$

$$\int_0^\infty dE_s\, \sigma(E_s, E_p) = 5\pi a_0^2 \alpha^3 \sum_i \frac{N_i I_H^2}{I_i^3} \frac{(T/I_i)^{\beta-1/2}}{4+(T/I_i)^{2\beta}} \times \frac{(I_i T)^{1/2}}{\alpha} \tag{2.27}$$

Thus the average energy of secondary electrons due to proton impact on the neutral species is:

$$\bar{E}_s(E_p) = \frac{\sum_i \frac{N_i I_H^2}{I_i^3} \frac{(T/I_i)^{\beta-1/2}}{4+(T/I_i)^{2\beta}} \times I_i T}{\sum_i \frac{N_i I_H^2}{I_i^3} \frac{(T/I_i)^{\beta-1/2}}{4+(T/I_i)^{2\beta}} \times \alpha (I_i T)^{1/2}} \tag{2.28}$$

The sum in equation 2.28 is usually dominated by a single term (outer most subshell) as indicated by Rudd (1979), and the average energy becomes simply:

$$\bar{E}_s(E_p) = \frac{(IT)^{1/2}}{\alpha} = \frac{(I E_p \gamma)^{1/2}}{\alpha} \tag{2.29}$$

where γ is the electron to proton mass ratio, I is the ionization threshold of the dominant subshell, and all other parameters are the same as in equation 2.24.

For charge exchange processes, Taulbjerg (1990) used energy-gain spectroscopy to measure the singly differential cross sections as function of energy loss. He concluded that the differential cross section can be expressed as a delta function for electron capture reactions with very small laboratory scattering angles. With delta functions used to specify the energy differential cross sections, the double differential cross sections can be written as:

$$\sigma_s^j(E', \mu' \to E, \mu) = \frac{1}{2\pi} \sigma_s^j(E') \delta(E' - (E + W_s^j)) \delta(\mu' - \mu) \tag{2.30}$$

where $\sigma_s^j(E')$ is the total collision cross sections of H^+/H at energy E' for collision process j with neutral species s, W_s^j is the energy loss associated with the collision, and j represents elastic, excitation, ionization, charge stripping and electron capture

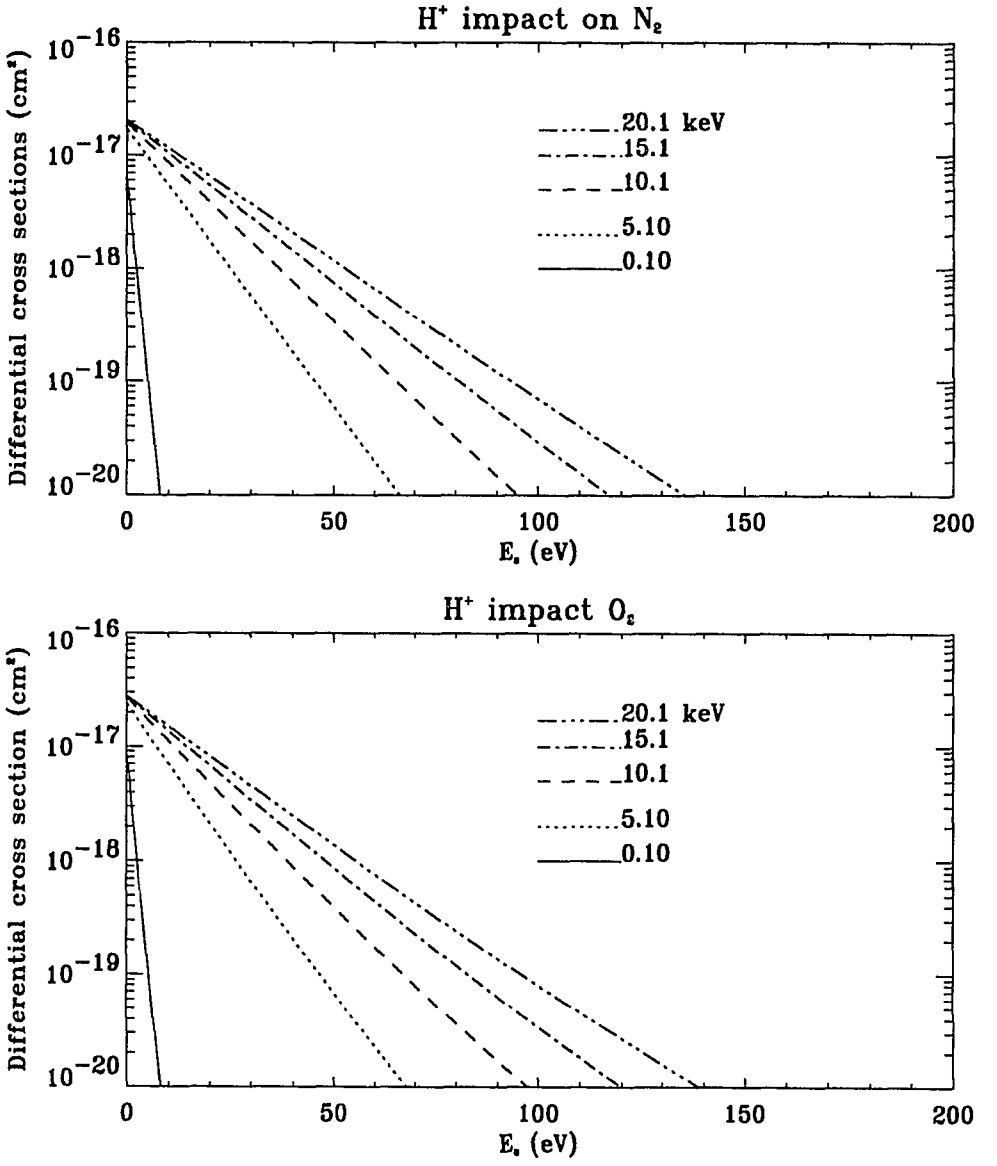

Figure 2.8: Cross sections for the production of secondary electrons by proton impact on (a) N_2, (b) O_2 at various energies.

processes. Values for W_s^k for each specific process will be given later in section 2.8. With the phase functions and singly differential cross sections being expressed by delta functions, the double integrations are carried out analytically, and the transport equations become:

$$\begin{aligned}
\mu\frac{\partial I_p(z,E,\mu)}{\partial z} &= -\sum_s n_s(z)\sigma_{s,p}(E)I_p(z,E,\mu) \\
&+ \sum_s n_s(z)\sum_j \sigma^j_{s,p}(E+W^j_{s,p}(E))I_p(z,E+W^j_{s,p}(E),\mu) \\
&+ \sum_s n_s(z)\sigma^{01}_s(E+W^{01}_s(E))I_H(z,E+W^{01}_s(E),\mu) \\
&+ \frac{(1-\mu^2)}{2B(z)}\frac{\partial B}{\partial z}\frac{\partial I_p(z,E,\mu)}{\partial \mu} \qquad (2.31) \\
\mu\frac{\partial I_H(z,E,\mu)}{\partial z} &= -\sum_s n_s(z)\sigma_{s,H}(E)I_H(z,E,\mu) \\
&+ \sum_s n_s(z)\sum_j \sigma^j_{s,H}(E+W^j_{s,H}(E))I_H(z,E+W^j_{s,H}(E),\mu) \\
&+ \sum_s n_s(z)\sigma^{10}_s(E+W^{10}_s(E))I_p(z,E+W^{10}_s(E),\mu) \qquad (2.32)
\end{aligned}$$

where the summation over j includes all elastic and inelastic collisional processes. Equations (2.31) and (2.32) are two coupled partial differential equations in altitude z and pitch angle μ. Numerical methods can be used to solve them if the cross section for each individual collisional process and energy loss associated with this collisional process are known. The cross sections and energy loss functions are discussed next.

2.7 Cross Sections

Collision cross sections of neutral species with H^+/H and energy losses associated with the collisions are crucial input parameters for H^+/H transport in the neutral atmosphere. In general, the double differential cross sections are needed to carry out the double integrations, but due to the characteristics of energetic H^+/H collision processes, the collisional phase functions can be approximated by delta functions. With these assumptions angular scattering is not important, and the important processes are the energy degradation and mirror reflection. The total collision cross

sections are then sufficient for solving the transport equations.

There have been many measurements of ionization cross sections of neutral species by H^+/H impact. Rudd et al. (1985) summarized the previous measurements and recommended values to be used for ionization cross sections of N_2 and O_2 by H^+ impact. McNeal and Birely (1973) measured ionization cross sections of N_2, O_2 and O by H impact, also ionization cross section of O by H^+ impact. All charge exchange (σ^{10}) and charge stripping (σ^{01}) cross sections are from the compilation of Van Zyl (1978). There are not many data available for the excitation cross sections of neutral species into individual states; most measurements of excitation cross section are deduced by measuring various optical emissions (Thomas, 1972). The excitation cross sections obtained in this way are used as the total excitation cross sections. The values adopted here are from compilations of Basu et al. (1987). The collected cross sections are shown graphically in figures 2.9 to 2.11, and the cross sections at several specific energies are shown in tables A.1 to A.3 in appendix A.

2.8 Energy Loss

Energy loss associated with each collisional process is important both for transport and for energy deposition rate, because it determines how deeply the particles can penetrate into the atmosphere. The energy loss is different for different processes. For elastic collisions, it can be calculated using classical energy and momentum conservation, while for inelastic processes, it is not easy to calculate, requiring some approximations that are in accord with the properties of the collisional processes. The energy loss for each process will be given in the following section.

2.8.1 Energy Loss in Elastic Scattering

Protons and hydrogen atoms deposit their energy in the atmosphere through both elastic and inelastic processes. In some previous calculations (Jasperse and Basu, 1982), the energy loss due to elastic scattering has been assumed to be zero. In electron transport, energy loss due to elastic scattering can be neglected because the electron mass is very small compared to the neutral gas mass, but protons and hydrogen atoms have masses comparable to the neutrals, so energy loss due to

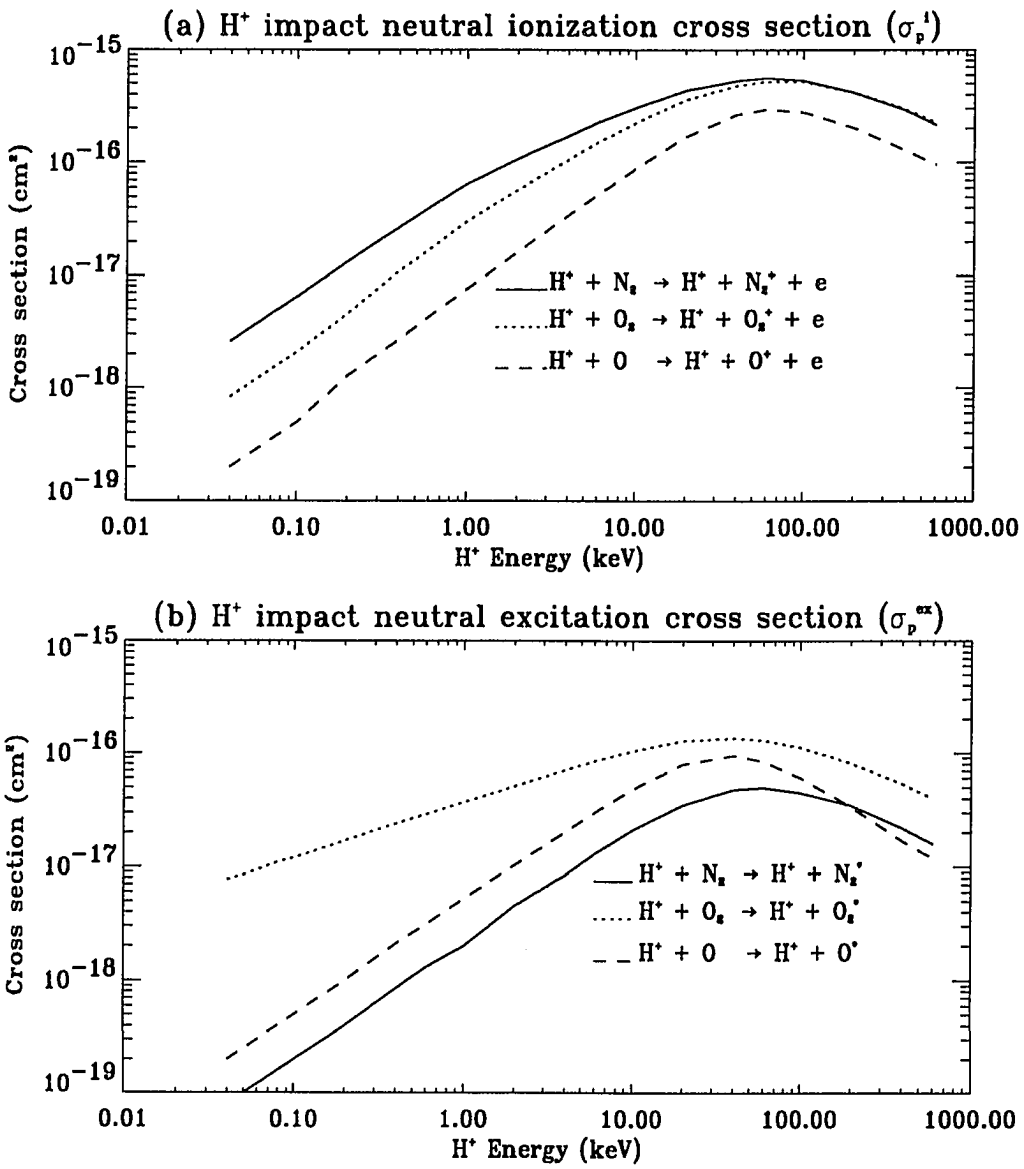

Figure 2.9: Ionization and excitation cross sections of N_2, O_2, and O by H^+ impact, (a) ionization cross sections, (b) excitation cross sections

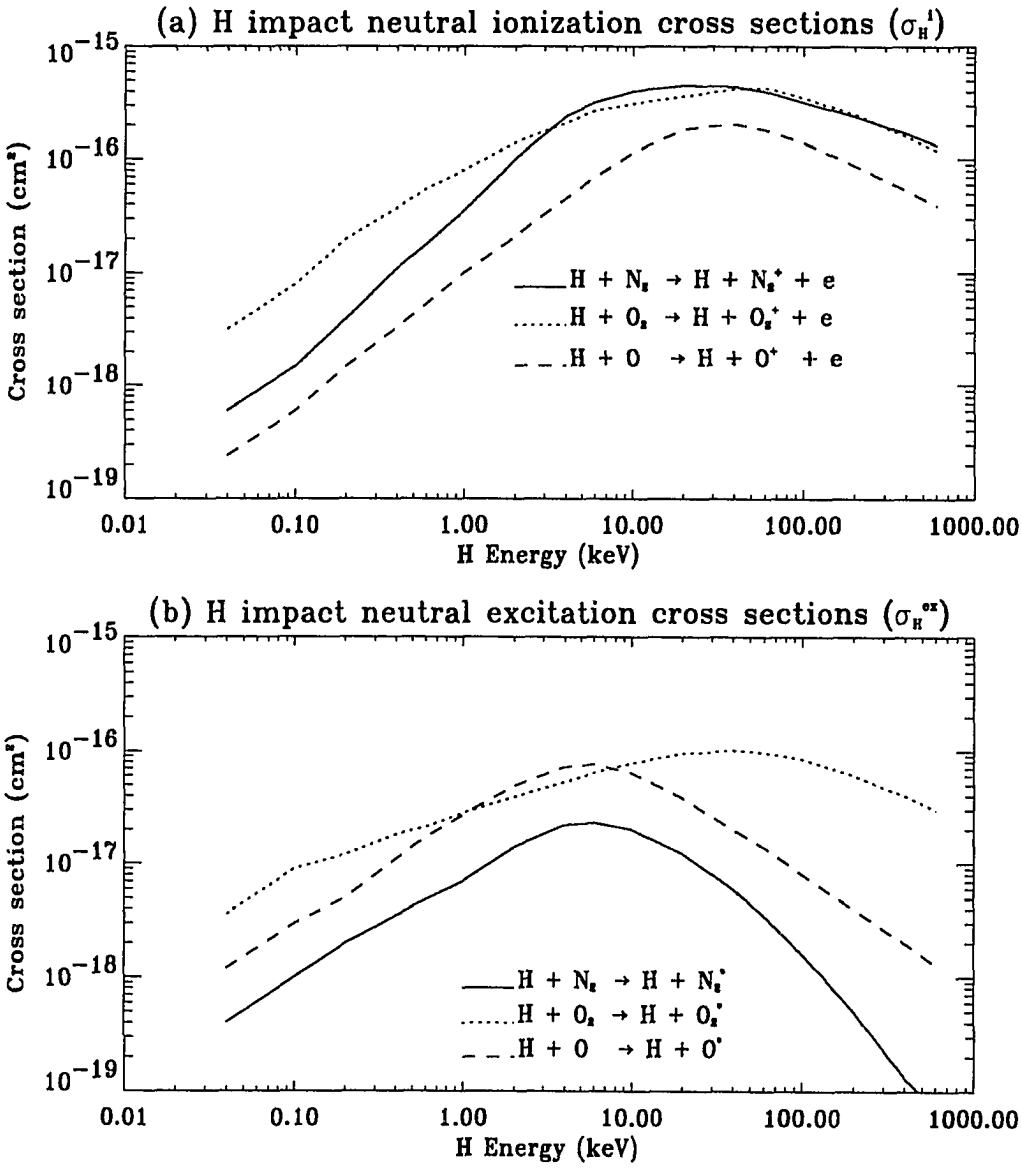

Figure 2.10: Ionization and excitation cross sections by H impact on N_2, O_2, and O (a)ionization cross sections, (b) excitation cross sections

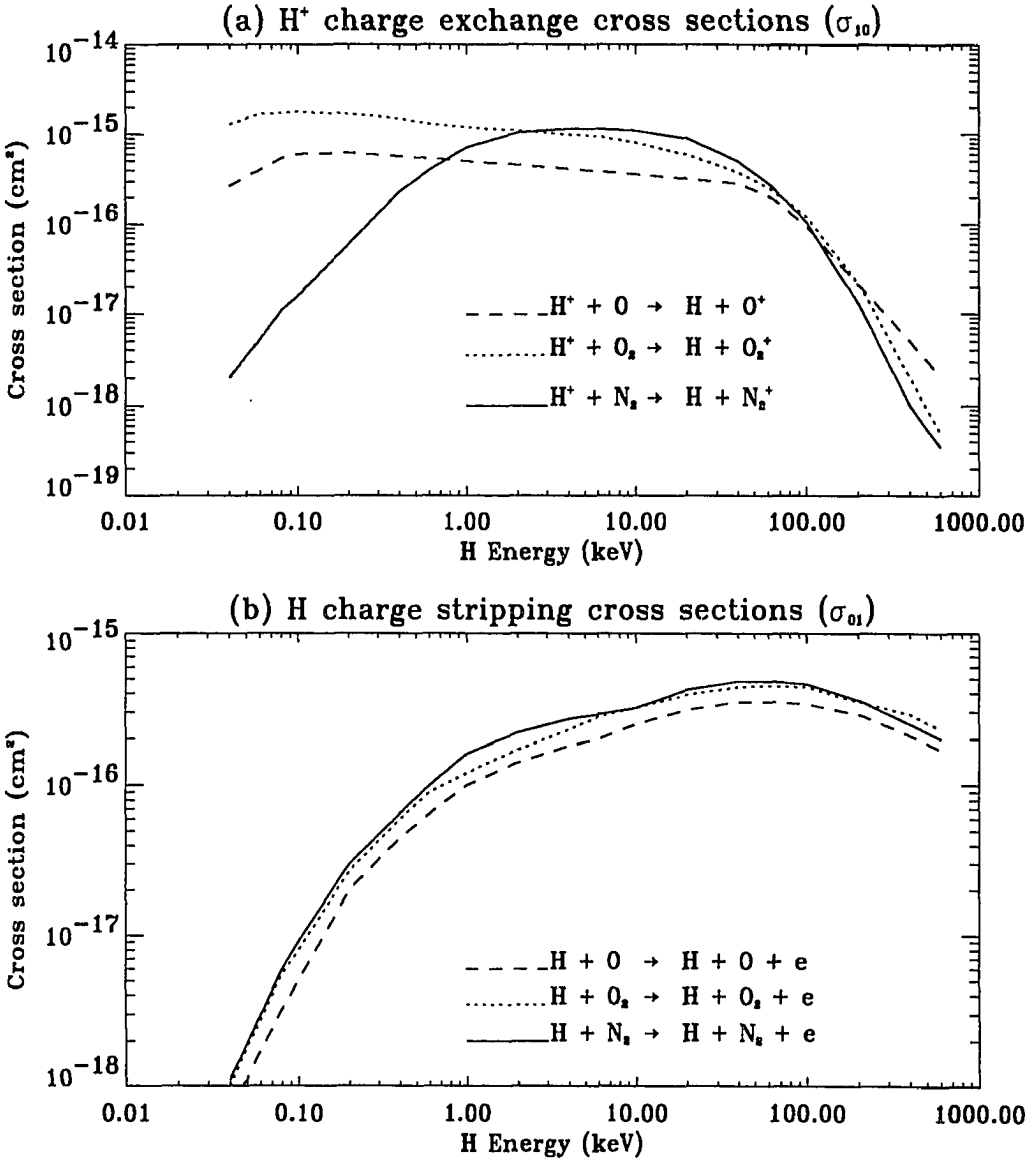

Figure 2.11: Charge exchange cross sections, (a) H^+ electron capture cross sections, (b)H charge stripping cross sections

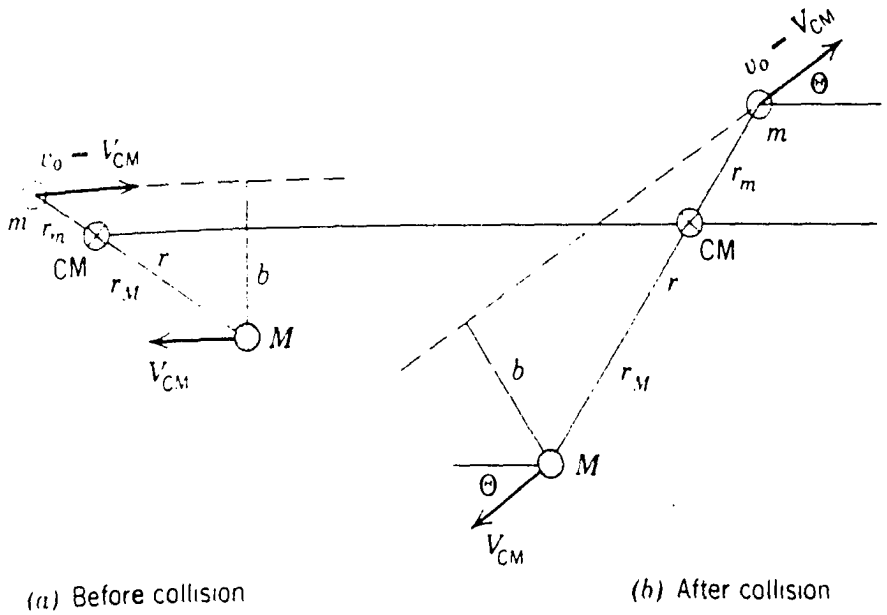

(a) Before collision (b) After collision

Figure 2.12: Elastic scattering in the laboratory frame. In each of the figures the distance between the particles r is much greater than the range of the interaction between the particles; m and M are at distance r_m and r_M respectively, from the center of mass.

elastic scattering in proton transport can not be neglected in the general case. It is shown below, however, that in forward scattering only, the energy loss is zero. Elastic processes can therefore be dropped from the transport equations.

Figure 2.12 illustrates an elastic collision process between an incident particle of mass m and a target particle of mass M. The target particle M is assumed at rest because the thermal velocity is much smaller than the speed of the incoming energetic particles. Before collision, the velocity of m is v_0, and M is at rest; after collision, m has velocity v and is deflected by θ relative to the original direction, the velocity of M is V at angle θ' as shown in the figure 2.12.

Energy and momentum conservation yields:

$$\frac{1}{2}mv_0^2 = \frac{1}{2}mv^2 + \frac{1}{2}MV^2 \quad (2.33)$$

$$mv_0 = mv\cos\theta + MV\cos\theta' \quad (2.34)$$

$$0 = mv\sin\theta - MV\sin\theta' \quad (2.35)$$

These equations are valid regardless of the form of the interaction between the particles provided the collision is elastic. Eliminating V and θ' yields:

$$(\frac{v}{v_0})^2 - \frac{2m}{M+m}\cos\theta(\frac{v}{v_0}) - \frac{M-m}{M+m} = 0 \quad (2.36)$$

From 2.36, v as a function v_0, m, M and scattering angle θ is obtained:

$$v = v_0\frac{m}{M+m}\left(\cos\theta + \sqrt{\frac{M^2}{m^2} - \sin^2\theta}\right) \quad (2.37)$$

The energy loss is:

$$\begin{aligned}\Delta E &= \frac{1}{2}m(v_0^2 - v^2) \\ &= \frac{1}{2}mv_0^2\left[1 - \left(\frac{m}{M+m}\right)^2\left(\cos\theta + \sqrt{\frac{M^2}{m^2} - \sin^2\theta}\right)^2\right]\end{aligned} \quad (2.38)$$

The relative energy loss is:

$$\begin{aligned}\Delta E_r &= \frac{\Delta E}{E_0} = 1 - f(\theta) \\ &= 1 - \left(\frac{m}{M+m}\right)^2\left(cos\theta + \sqrt{\frac{M^2}{m^2} - \sin^2\theta}\right)^2\end{aligned} \quad (2.39)$$

The relative energy loss fraction as function of scattering angle θ is shown in figure 2.13 for collisions of protons or hydrogen atoms with major neutral species N_2, O_2, and O.

The energy loss expression 2.39 is exact regardless of the interaction potential form between collision partners and is valid for any scattering angle, and it is easy to see that $\Delta E(\theta = 0) = 0$. Bray et al. (1977) measured the energy loss in elastic collisions at small scattering angles experimentally, and confirmed that 2.39

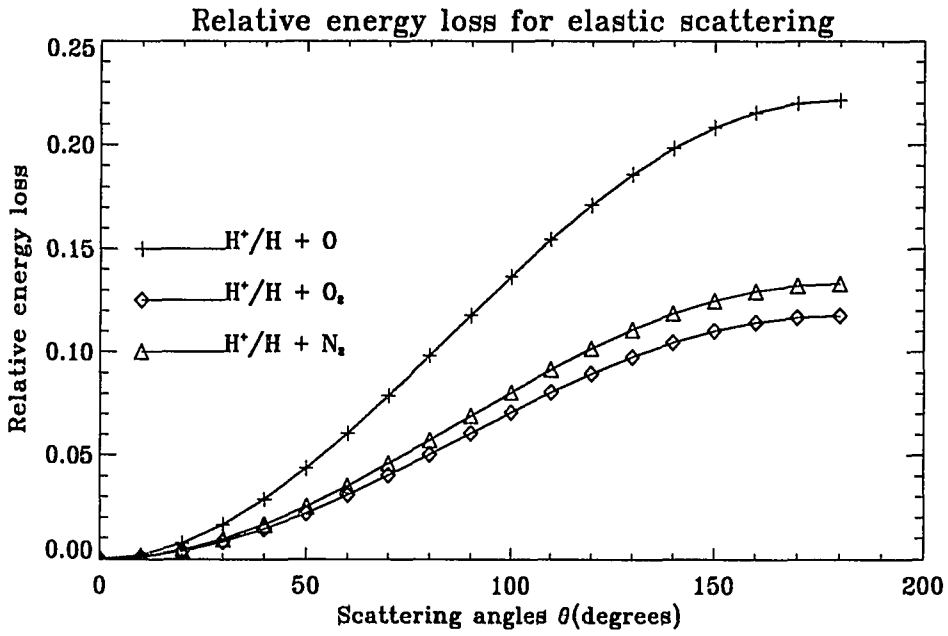

Figure 2.13: The relative energy loss of protons or hydrogen atoms as a function of scattering angle θ, $+$ — is for collision with oxygen atom O; Δ — for collision with nitrogen molecules; and $\diamond$ — is for collision with oxygen molecules.

is correct. This justifies adopting zero energy loss for elastic collisions in the forward scattering approximation.

2.8.2 Energy Loss due to Inelastic Scattering Processes

The projectile particles H^+/H will lose kinetic energy to internal energy of the neutral species through inelastic collisions. The energy loss of H^+ is assumed to be the same as that of H, for simplicity. The energy loss depends on the individual states of the target gas being excited or ionized, while the cross sections given in section 2.7 are the total cross sections. Little information is available about which state of the target gas is excited or ionized, so it is difficult to determine exactly how much energy has been transferred into internal energy of the target gas. It is only possible to estimate the energy loss of projectiles in each individual collision.

For discrete excitation processes, excitation to individual states is not considered,

and the energy loss of the projectile H^+/H equals the energy level difference in a two energy level system. This is true only for light projectiles, such as electrons and photons, because the mass ratio of electron to neutral is so large that the target neutral, at rest before being impacted on by electrons, can be considered to remain at rest. For heavy particles such as H^+/H, the momentum conservation has to be taken into account because the mass of the proton and hydrogen atom is comparable to that of neutral species. In order to excite the target into the excited state, the energy of the proton and hydrogen atom has to be greater than the threshold of the target gas because of the momentum conservation requirement. In some previous calculations (Basu et al., 1990), no attention has been paid to the momentum conservation. For example, the excitation threshold of N_2 ($a^1\Pi$) by electron impact was measured to be 9.11 eV by Tanaka (1955). In order for the collision of H^+/H with N_2 to have 9.11 eV transferable kinetic energy, the H^+/H projectile energy would have to be at least 9.44 eV to satisfy both energy and momentum conservations. Schowengerdt and Park (1970) measured the energy loss of H^+ through collision with N_2 and found it to be 9.5 eV which is in agreement with the calculated energy loss of 9.44 eV. The experimental measured energy loss of 9.5 eV is actually used in the numerical calculations and is listed in Table 2.2 as the energy loss of H^+/H through excitation collisions with nitrogen molecules N_2. No experimental data are available for the energy loss of H^+/H through excitational collisions with molecular and atomic oxygen, the energy losses are estimated through energy level diagrams of O_2 and O in analogy to that of N_2.

For ionization processes, the energy loss is given by $I_s + \bar{E}_s(E_p)$ where I_s is the ionization threshold of the neutral particle s, and $\bar{E}_s$ is the average energy of the secondary electron which can be calculated using equation 2.29. The threshold I_s of neutral species under the impact of H^+/H can be calculated from the corresponding photoionization threshold which can be found in Rees (1989) and by considering both momentum conservation and energy conservation similarly to the excitation threshold determination. The ionization threshold I_s for N_2, O_2, and O due to proton and hydrogen atom impact are calculated to be 16.14, 12.46 and 14.46 eV, respectively, from corresponding photoionization thresholds. The values of the energy losses which are the same for both protons and H atoms are denoted by W^i in table 2.2 for some specific projectile energies.

For the charge stripping process, the energy loss W^{01} is given by $E_\beta + E_s$, where $E_\beta = 13.6eV$ is the ionization threshold of hydrogen atoms. The average energy $E_s(E)$ of the ejected electron has been calculated empirically by Van Zyl et al. (1984). All species share the same ionization threshold energy of the hydrogen atom and the energy of the secondary electron, E^s, thus the energy loss W^{01} is independent of the neutral species and is put into the last column of table 2.2

For the charge exchange process, the energy loss is given by $I_s + E\gamma$, where γ is the electron to proton mass ratio, and I_s is the ionization threshold of neutral species s. The reason that the energy loss for charge exchange is estimated in this way is based on the argument given by Basu et al. (1987) that the charge exchange process is viewed as one in which an electron is ejected from the neutral atom and then captured by the incident proton. It is argued that the capture probability is maximum when the ejected electron is moving with the same speed as that of the proton, i.e., when the energy of the ejected electron is close to the value $E\gamma$. The energy loss in a charge exchange process is denoted by W_s^{10} in table 2.2.

In energy loss calculations, the common assumption is that the kinetic energy transferred to the target gas from the projectile is the minimum in order to satisfy both energy and momentum conservation, and no internal energy is transferred into the excited state of the hydrogen atom. This assumption simplifies the problem, but underestimates the energy loss of the projectiles; the actual energy loss will be larger than what is used in solving the transport equations. This will cause an apparent deeper particle penetration. The effects of this underestimate of the energy loss will be discussed in chapter 4 when the model is compared with experimental data.

Table 2.2: Inelastic energy loss in neutral species

energy	N_2			O_2			O			
E_p	W^i	W^{ex}	W^{10}	W^i	W^{ex}	W^{10}	W^i	W^{ex}	W^{10}	W^{01}
(keV)	(eV)	(eV)	(eV)	(eV)	(eV)	(eV)	(eV)	(eV)	(eV)	(eV)
1.0e–1	17.17	9.5	16.2	13.41	5.2	12.6	15.48	11.0	14.6	14.0
2.0e–1	17.60	9.5	16.2	13.79	5.2	12.6	15.88	11.0	14.7	14.1
4.0e–1	18.20	9.5	16.3	14.32	5.2	12.7	16.45	11.0	14.7	14.4
6.0e–1	18.66	9.5	16.4	14.73	5.2	12.8	16.89	11.0	14.8	14.6
1.0e+0	19.40	9.5	16.6	15.38	5.2	13.0	17.59	11.0	15.0	14.9
2.0e+0	20.75	9.5	17.2	16.57	5.2	13.6	18.87	11.0	15.6	15.6
4.0e+0	22.66	9.5	18.3	18.26	5.2	14.7	20.68	11.0	16.7	16.8
6.0e+0	24.12	9.5	19.4	19.55	5.2	15.8	22.07	11.0	17.8	18.0
1.0e+1	26.44	9.5	21.5	21.61	5.2	17.9	24.27	11.0	19.9	20.1
2.0e+1	30.71	9.5	27.4	25.38	5.2	23.4	28.32	11.0	28.9	26.0
4.0e+1	36.75	9.5	37.9	30.71	5.2	34.3	34.04	11.0	36.3	36.6
6.0e+1	41.38	9.5	48.9	34.81	5.2	45.2	38.44	11.0	47.2	47.6
1.0e+2	48.72	9.5	70.6	41.30	5.2	67.0	45.40	11.0	69.0	66.0
2.0e+2	62.22	9.5	125.0	53.23	5.2	121.4	58.20	11.0	123.4	125.6
4.0e+2	81.30	9.5	234.0	70.10	5.2	230.4	76.30	11.0	232.4	233.6
6.0e+2	95.94	9.5	342.9	83.05	5.2	339.3	90.19	11.0	341.3	343.6

Chapter 3

Solution of the Transport Equations

3.1 Magnetic Mirror Reflection

In the forward scattering approximation the only force that can change the pitch angle of the precipitating protons is due to the convergent magnetic field. This mirror force is responsible for coupling between the forward and backward streaming particles. Only the downward moving particles are subject to magnetic reflection, while the upward moving particles can not turn back to the downward direction. The transport equation is therefore separated into a downward and an upward component. There is no coupling btween the downward and upward moving particles, so the two components can be solved separately.

Protons with a specified energy and pitch angle distribution at the top of the atmosphere penetrate along magnetic field lines. Due to the converging magnetic field, the downward moving particles will change pitch angle. When the pitch angle of protons at the top of a slab is larger than a critical angle θ_c, the pitch angle will reach 90° at the bottom of the slab. The protons will then be reflected back at the bottom of the slab as shown in figure 3.1. The reflected particles will not be able to come down again because the pitch angle always decreases on the way up. They become the internal source for the upward transport equations and a loss term for the downward transport equations. The upward transport equations yield the particle distributions in the upward direction. The upward moving H atoms may

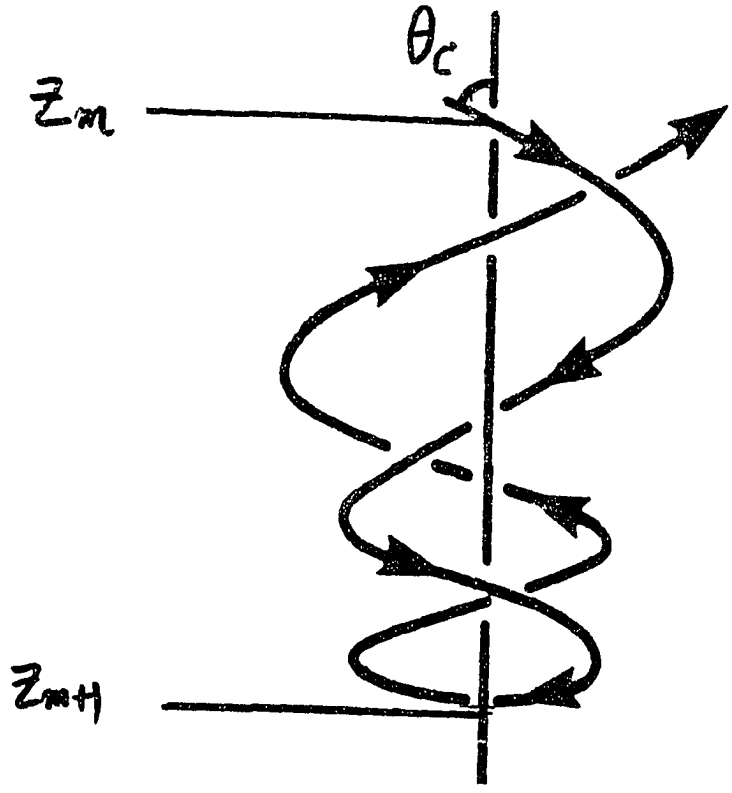

Figure 3.1: Critical angle θ_c for mirror reflection. Particles with pitch angles greater than the critical angle θ_c on the top of a slab will be reflected back upwards from the bottom of the slab.

be in an excited state which on radiative decay produces the red shifted portion of the emission relative to observers looking up along a magnetic field line.

3.2 Solution of the Coupled Equations

It has been shown in section 2.8.1 that the energy loss for elastic collisions is zero in the forward scattering approximation, resulting in a mutual cancellation of the source and the loss terms for elastic scattering in the transport equations. The transport equations in the forward scattering approximation are:

$$\begin{aligned}
\mu\frac{\partial I_p(z,E,\mu)}{\partial z} &= -\sum_s n_s(z)\sigma_{s,p}(E)I_p(z,E,\mu) \\
&+ \sum_s n_s(z)\sum_k \sigma^k_{s,p}(E+W^k_{s,p}(E))I_p(z,E+W^k_{s,p}(E),\mu) \\
&+ \sum_s n_s(z)\sigma^{01}_s(E+W^{01}_s(E))I_H(z,E+W^{01}_s(E),\mu) \\
&+ \frac{(1-\mu^2)}{2B(z)}\frac{\partial B}{\partial z}\frac{\partial I_p(z,E,\mu)}{\partial \mu} \qquad (3.1) \\
\mu\frac{\partial I_H(z,E,\mu)}{\partial z} &= -\sum_s n_s(z)\sigma_{s,H}(E)I_H(z,E,\mu) \\
&+ \sum_s n_s(z)\sum_k \sigma^k_{s,H}[E+W^k_{s,h}(E)]I_H(z,E+W^k_{s,H}(E),\mu) \\
&+ \sum_s n_s(z)\sigma^{10}_s(E+W^{10}_s(E))I_p(z,E+W^{10}_s(E),\mu) \qquad (3.2)
\end{aligned}$$

The summation over k differs from the previous summation over j, in that k no longer includes elastic scattering. (3.1) and (3.2) are a system of two coupled partial differential equations. To solve these equations numerically, a finite two dimensional grid of unevenly spaced energy points from E_{min} to E_{max} and unevenly spaced altitude points from z_{min} to z_0 is chosen for each value of μ. Interpolation is used to map intensities onto grid points. With some algebraic manipulations (see appendix B), the transport equations can be written in the following form:

$$\begin{aligned}
\mu\frac{\partial I_p(z,E_n,\mu)}{\partial z} &= -A_pI_p(z,E_n,\mu) + B_pI_p(z,E_{n+1},\mu) \\
&+ A_HI_H(z,E_n,\mu) + B_HI_H(z,E_{n+1},\mu) \\
&+ \frac{(1-\mu^2)}{2B(z)}\frac{\partial B}{\partial z}\frac{\partial I_p(z,E_n,\mu)}{\partial \mu} \qquad (3.3) \\
\mu\frac{\partial I_H(z,E_n,\mu)}{\partial z} &= -C_HI_H(z,E_n,\mu) + D_HI_H(z,E_{n+1},\mu) \\
&+ C_pI_p(z,E_n,\mu) + D_pI_p(z,E_{n+1},\mu) \qquad (3.4)
\end{aligned}$$

where A_p, B_p, C_p, D_p, A_H, B_H, C_H, and D_H are defined in appendix B.

Equations (3.3) and (3.4) are two coupled partial differential equations in altitude z and and pitch angle μ, and difference equations in energy E and there is no upward scattering in energy. The transport equations are now solved for a single energy, E_{max}, as function of altitude and pitch angle. Since the projectile particles

degrade in energy along the way down into the atmosphere through collisions with neutral atmospheric species, and no particles gain energy, there is no source term for particles with energy E_{max}. The transport equations at the maximum energy are

$$\mu\frac{\partial I_p(z,E,\mu)}{\partial z} = -\sum_s n_s(z)\sigma_{s,p}(E)I_p(z,E,\mu) + \frac{(1-\mu^2)}{2B(z)}\frac{\partial B}{\partial z}\frac{\partial I_p(z,E,\mu)}{\partial \mu} \quad (3.5)$$

$$\mu\frac{\partial I_H(z,E,\mu)}{\partial z} = -\sum_s n_s(z)\sigma_{s,H}(E)I_H(z,E,\mu) \quad (3.6)$$

with $E = E_{max}$ in equations (3.5) and (3.6). There is no coupling between protons and hydrogen atoms at the maximum point, E_{max}; thus the transport equations (3.5) and (3.6) can be solved separately as ordinary partial differential equations. It is assumed that there is no downward energetic hydrogen atom flux at the top of atmosphere. $I_H(z,E,\mu) = 0$ at $E = E_{max}$. Equation (3.5) yields the particle intensities of protons at E_{max} as functions of altitude and pitch angles. The particle intensities at the maximum energy become auxiliary boundary conditions which together with the input spectrum boundary condition at the top give the two boundary conditions necessary to solve for the particle intensities at any energy, altitude and pitch angle. The cross sections given in chapter 2 and the neutral densities derived from the MSIS90 model are adopted in the calculations.

A second order implicit integration scheme, given in appendix B, is adopted with appropriate boundary conditions in cosine of pitch angle μ requiring minimal attention to the stability of the solution. Starting from the top layer, with a given particle intensity as a function of energy and pitch angle, the derivative with respect to pitch angle is calculated. For the next layer down, the transport equations are first solved for the particle distribution at the maximum energy, E_{max}, and for each pitch angle μ. Then, with the altitude in a do-loop, the particle distribution at each energy grid point is calculated by energy degradation with the maximum energy as boundary condition at each pitch angle. By this scheme, particle intensities as a function of altitude, energy and pitch angle can be calculated layer by layer.

Since transport and energy degradation occur simultaneously, there are restrictions on the choice of grid distribution in both altitude and energy. Particles with

pitch angle μ and energy E will have N_c=$\sigma(E) \times n(z) \times dz/\mu$ collisions after passing through distance dz/μ, and at the same time will lose energy $\Delta = N_c \times W(E)$, assuming that the energy loss is $W(E)$ for one specific collision. In order to use interpolation and avoid extrapolation, the energy grid has to satisfy the following conditions for the same specific collision:

$$dE = \Delta E_i \geq \Delta(E_i, z_j, \mu_k) = W(E_i) \times \sigma(E_i) \times n(z_j) \times dz_j/\mu_k \qquad (3.7)$$

where ΔE_i is the energy grid size at point E_i, dz_j is the altitude grid size at point z_j, and μ_k is the cosine of the pitch angle of stream k, $\sigma(E_i)$ is the cross section for the specific collision and $n(z_j)$ is the neutral density at point z_j. The energy loss $\Delta(E_i, z_j, \mu_k)$ is a function of energy, altitude and pitch angle for each specific energy degradation process. With six different energy degradation processes identified by these variables, it is difficult to choose energy and altitude grids to satisfy equation (3.7). The grids for pitch angle, altitude and energy are chosen as follows in my calculation.

First, the pitch angle grid is set up using a Gaussian quadrature method. The number of the pitch angle grid points is given by number of streams.

Then, for the altitude grid points, the following equations are used to determine the altitude grid distribution:

$$z_m = \frac{1}{B} \ln\left(\frac{A}{m}\right) \qquad (3.8)$$

where m is an integer representing the do-loop number. m varies from 1 to M, the total number of grid points, corresponding to an altitude change from top to bottom. A and B are two constants which are determined from the upper and lower boundary altitudes and the total number of altitude points. For example, if the altitude is chosen to range from 80 km to 800 km, with a total of 70 grid points, then

$$z_1 = 800 = \frac{1}{B} \ln(A) \qquad (3.9)$$

$$z_{70} = 80 = \frac{1}{B} \ln\left(\frac{A}{70}\right) \qquad (3.10)$$

A and B are determined to be 112.23 and 0.0059 by equations (3.9) and (3.10).

Finally, after the altitude and pitch grid points are determined, the energy grid point distribution is given by:

$$\Delta E_i = \Delta E_{i-1} + \Delta \tag{3.11}$$

where Δ is a small constant. The energy grid size ΔE_i increases through the entire range. The small constant Δ is chosen such that equation (3.7) can be satisfied for most of the energy grid points. The transport code is run for various combinations of $E \times z \times \mu$ grid points. Energy and particle conservation are checked for each case and the energy grid is modified until conservation criteria are satisfied. A satisfactory combination was found to be 70 points for z(80 km$\leq z \leq$ 800 km), 150 points for E(0.1 keV $\leq E \leq$600 keV), and 12 points for μ(-1$\leq \mu \leq$ 1).

3.3 Numerical Results

Three neutral constituents (N_2, O_2, and O) are used in the calculations and their densities are given by the MSIS-90 model. The collisional cross sections used have been given in section 2.4. Most rocket measurements (Söraas et al., 1974; Miller and Whalen, 1976; Whalen and McDiarmid, 1972) have revealed that the angular distribution of proton precipitation in most proton auroras is almost isotropic over the upper hemisphere (downward precipitation) at all energies. All the calculations are done with isotropic pitch angle distributions except for the reflectivity calculations which are done for several different angular inputs to show the dependence of magnetic mirror reflection on pitch angle. The code can calculate the particle intensities of proton and hydrogen atoms for any type of input distribution, and both Maxwellian and monoenergetic energy distributions are used with the isotropic pitch angle assumption.

3.3.1 Hemispherically Averaged Intensities

The hemispherically averaged particle intensities are obtained by integrating the specific intensities obtained from solving the transport equations over pitch angle.

$$\begin{aligned} \bar{I}_\beta(z,E) &= 2\pi \int d\mu I_\beta(z,E,\mu) \\ &= 2\pi \sum_i w_i I_\beta(z,E,\mu_i) \end{aligned} \tag{3.12}$$

The summation is carried out over a hemisphere to obtain the upward or downward hemispheric intensity, w_i is the weight which is given by the Gaussian integration once the number of pitch angles is specified, a total of twelve in these calculations, $\beta = p, H$ for protons and hydrogen atoms, respectively. Figure 3.2 shows intensities of protons and hydrogen atoms as functions of energy at some given altitudes in the downward and upward directions with a Maxwellian input differential energy spectrum at the top of the atmosphere. Figure 3.3 shows similar results for a different characteristic energy E_0.

The effects of energy degradation processes and particle conversion processes between protons and hydrogen atoms as particles penetrate into the atmosphere are evident in figures 3.2 and 3.3. Energy degradation moves particles from high energy to low energy bins, building up the population of low energy particles. Charge exchange reactions convert protons into hydrogen atoms and, because the charge exchange cross section is much larger than the charge stripping cross section at low energy, hydrogen atoms become more abundant than protons at low energy, as shown in figures 3.2 and 3.3. The same situation holds for particles reflected upward, with hydrogen atoms more abundant than protons at low energy.

With the mirror force included in the transport equation, it is of interest to compute the flux of reflected particles. The reflectivity is defined as the ratio of the upward directed flux to the downward input flux at the top of the atmosphere:

$$R_p = \frac{2\pi \int_0^1 \mu d\mu \int_{E_{min}}^{E_{max}} dE\, I_t(z_0,E,\mu)}{2\pi \int_{-1}^0 \mu d\mu \int_{E_{min}}^{E_{max}} dE\, I_t(z_0,E,\mu)} \tag{3.13}$$

$I_t(z_0,E,\mu)$ is the sum of proton and hydrogen atom intensities at the top of the atmosphere z_0. The particle reflectivity, R_p , for a Maxwellian input spectrum is shown in figure 3.4(a) as a function of characteristic energy. The energy reflectivity

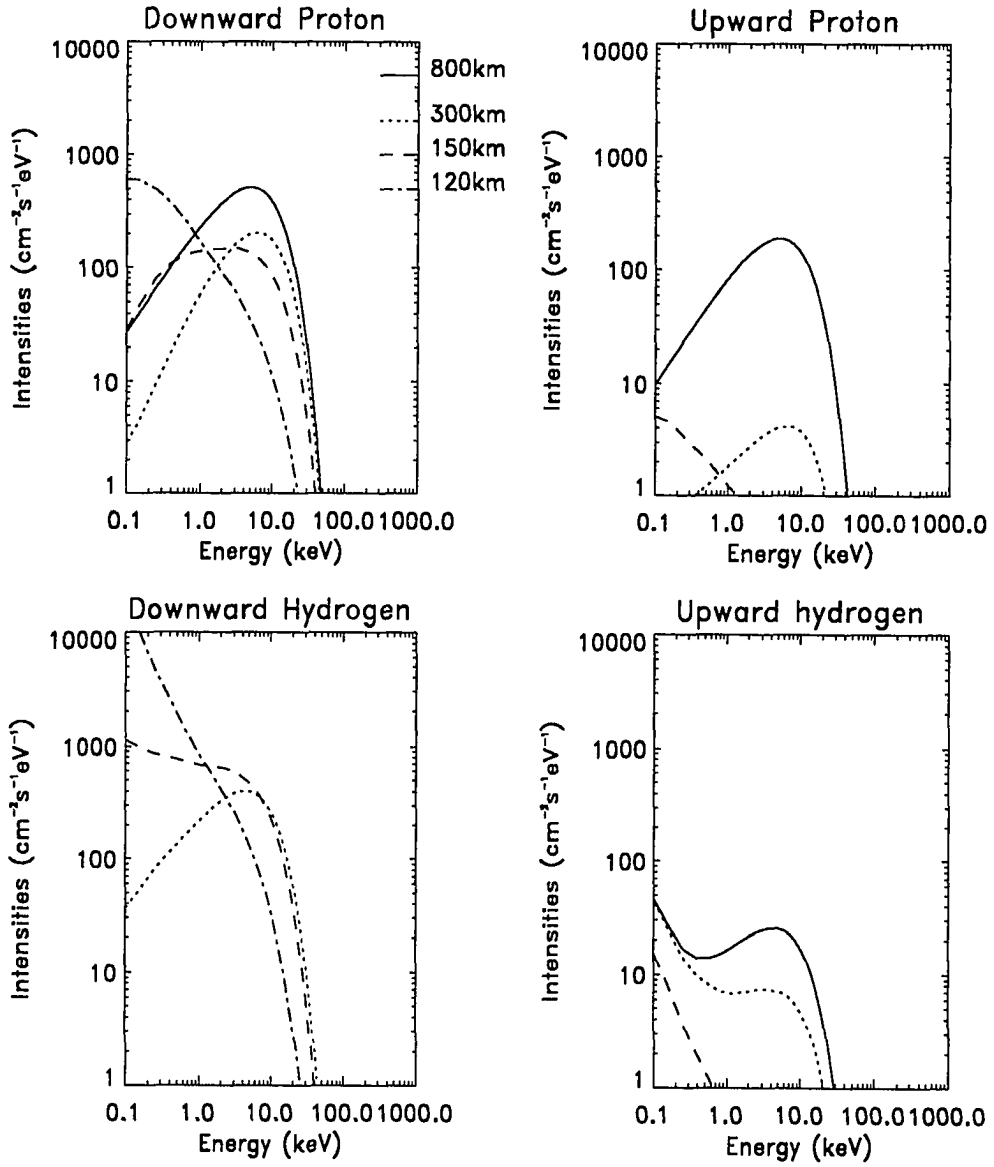

Figure 3.2: Hemispherically averaged particle intensities of H^+/H as functions of energy at some given altitudes z for a Maxwellian input energy spectrum with characteristic energy E_0=5.0 keV, and a total energy flux of 0.5 erg $cm^{-2}s^{-1}$.

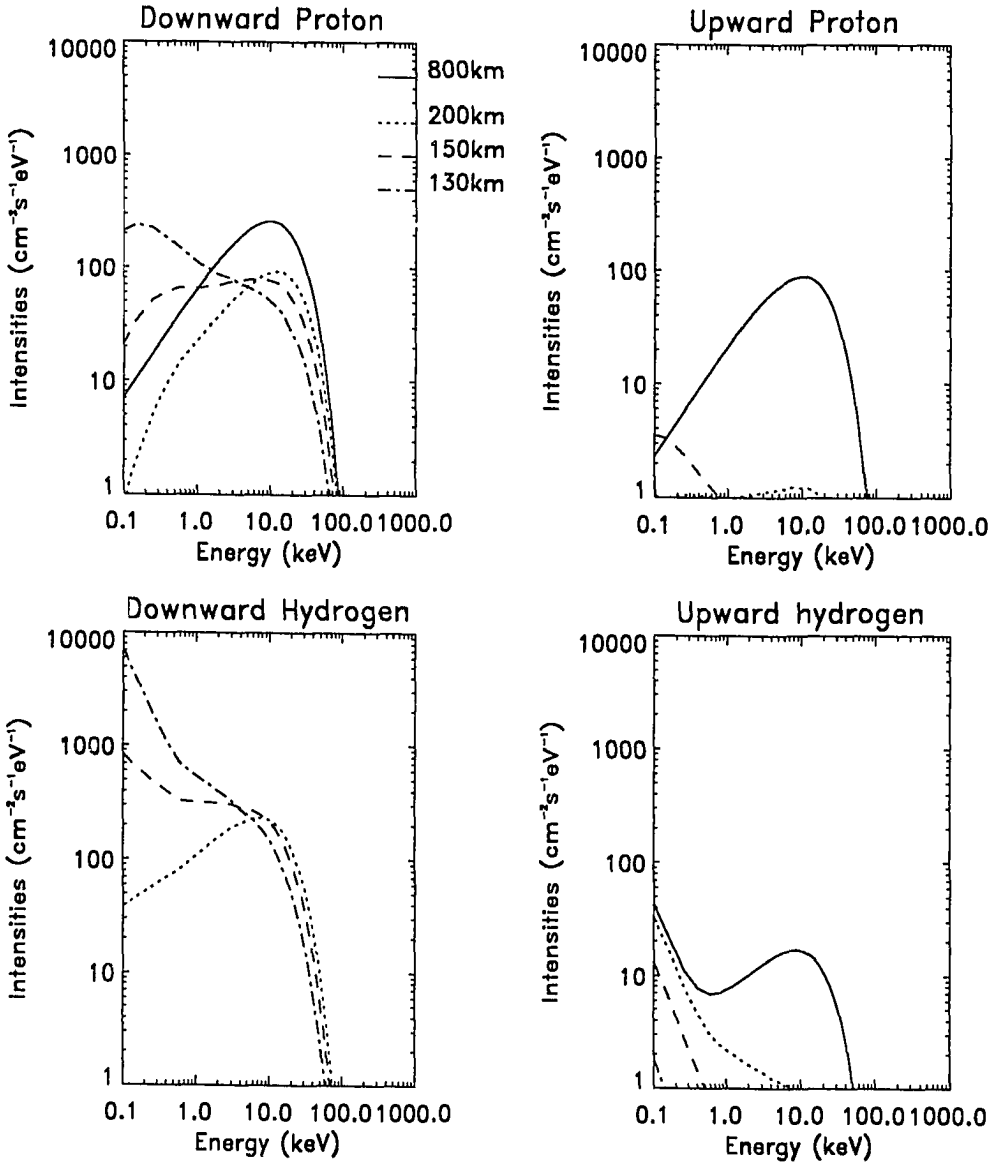

Figure 3.3: Hemispherically averaged particle intensities of H^+/H as functions of energy at some chosen altitudes. The input differential energy flux is Maxwellian, with characteristic energy E_0=10.0 keV, and the total input energy flux is 0.5 erg cm^{-2} s^{-1}.

is defined similarly by:

$$R_e = \frac{2\pi \int_0^1 \mu d\mu \int_{E_{min}}^{E_{max}} E\, dE\, I_t(z_0, E, \mu)}{2\pi \int_{-1}^0 \mu d\mu \int_{E_{min}}^{E_{max}} E\, dE\, I_t(z_0, E, \mu)} \tag{3.14}$$

where all the symbols are the same as those in equation 3.13. The energy reflectivity as function of characteristic energy is shown in figure 3.4 (b) for a Maxwellian proton energy distribution. The calculation is done for a total energy input rate of 0.5 erg/cm^2/s. Figure 3.4(a) and (b) show that the mirror reflectivity in both energy and particles increases very slightly with characteristic energy E_0, but is almost independent of the energy distribution of the input spectrum. The mirror force depends only on the pitch angle, not on the energy of the projectile particles. The slight increase in reflectivity with energy is due to the larger fraction of protons at high energy compared to hydrogen atoms which are free of magnetic field confinement. Only protons are subject to mirror reflection.

To show the dependence of the reflectivity on the pitch angle distribution, three types of angular distributions, pancake, isotropic and very forward peaked, are used in the calculations. The reflectivities are shown in figure 3.4(a) and (b). For a pancake angular distribution ($1-cos^2\theta$), the reflectivity in both particles and energy can reach as high as about 30%. For very forward peaked angular distributions($cos^2\theta$), the reflectivity is about 4%.

3.3.2 Composition in H^+/H streams

The fraction of protons and hydrogen atoms in an H^+/H stream can be calculated as function of energy and altitude by the following formulae:

$$F_1(z, E) = \frac{\bar{I}_p^t(z, E)}{\bar{I}_p^t(z, E) + \bar{I}_H^t(z, E)} \tag{3.15}$$

$$F_0(z, E) = \frac{\bar{I}_H^t(z, E)}{\bar{I}_p^t(z, E) + \bar{I}_H^t(z, E)} = 1 - F_1(z, E) \tag{3.16}$$

where $\bar{I}_p^t(z, E)$ and $\bar{I}_H^t(z, E)$ are the total averaged intensities (upward plus downward) of protons and hydrogen atoms, respectively. The fraction of proton and H atoms in the mixture depends on both altitude and energy; the calculated proton fraction, F_1, as a function of energy for various altitudes is shown in figure 3.5(a).

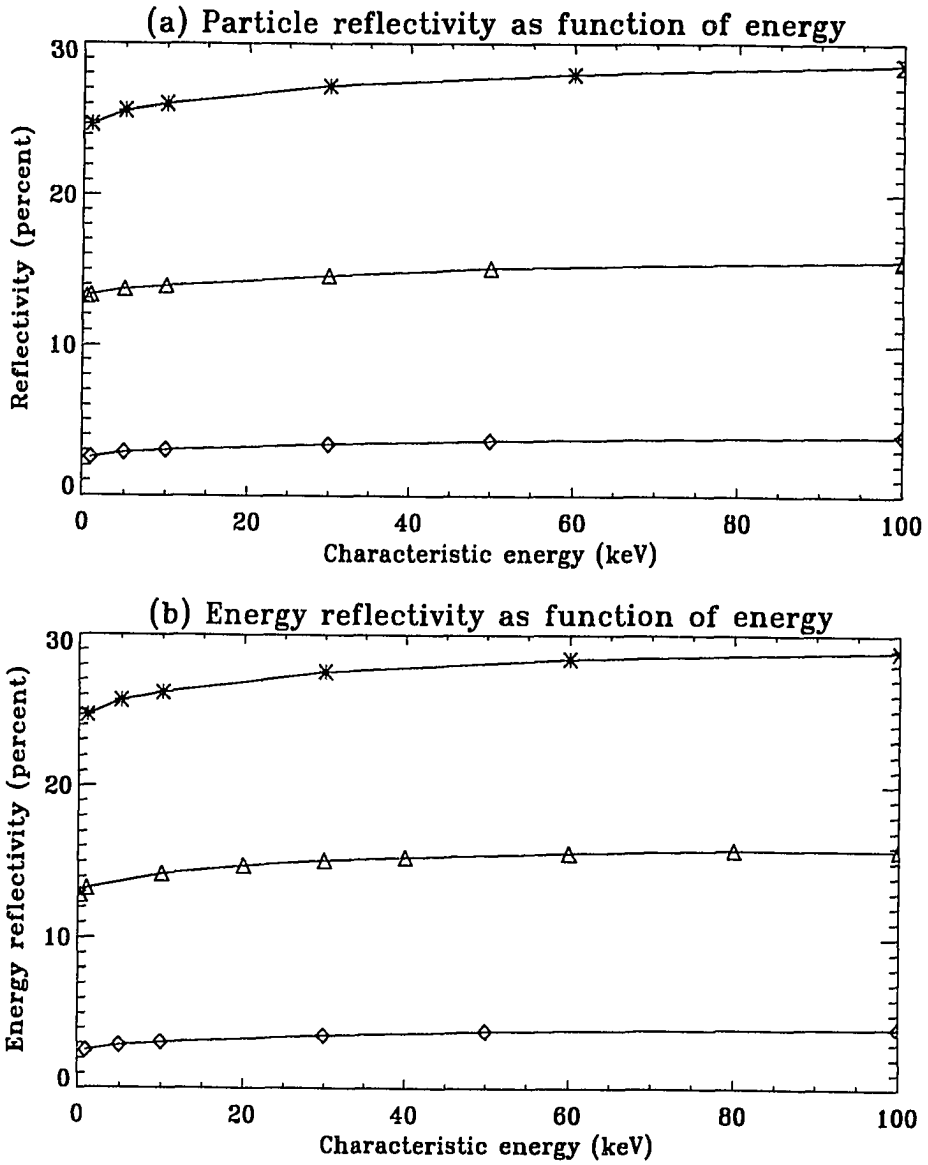

Figure 3.4: Particle and energy reflectivity as a function of characteristic energy E_0 for a Maxwellian energy distribution and different angular distributions; $*$ — pancake, $\triangle$ — isotropic, $\diamond$ — forward peaked distributions, (a) particle reflectivity, (b) energy reflectivity. The angular distributions are defined in the text.

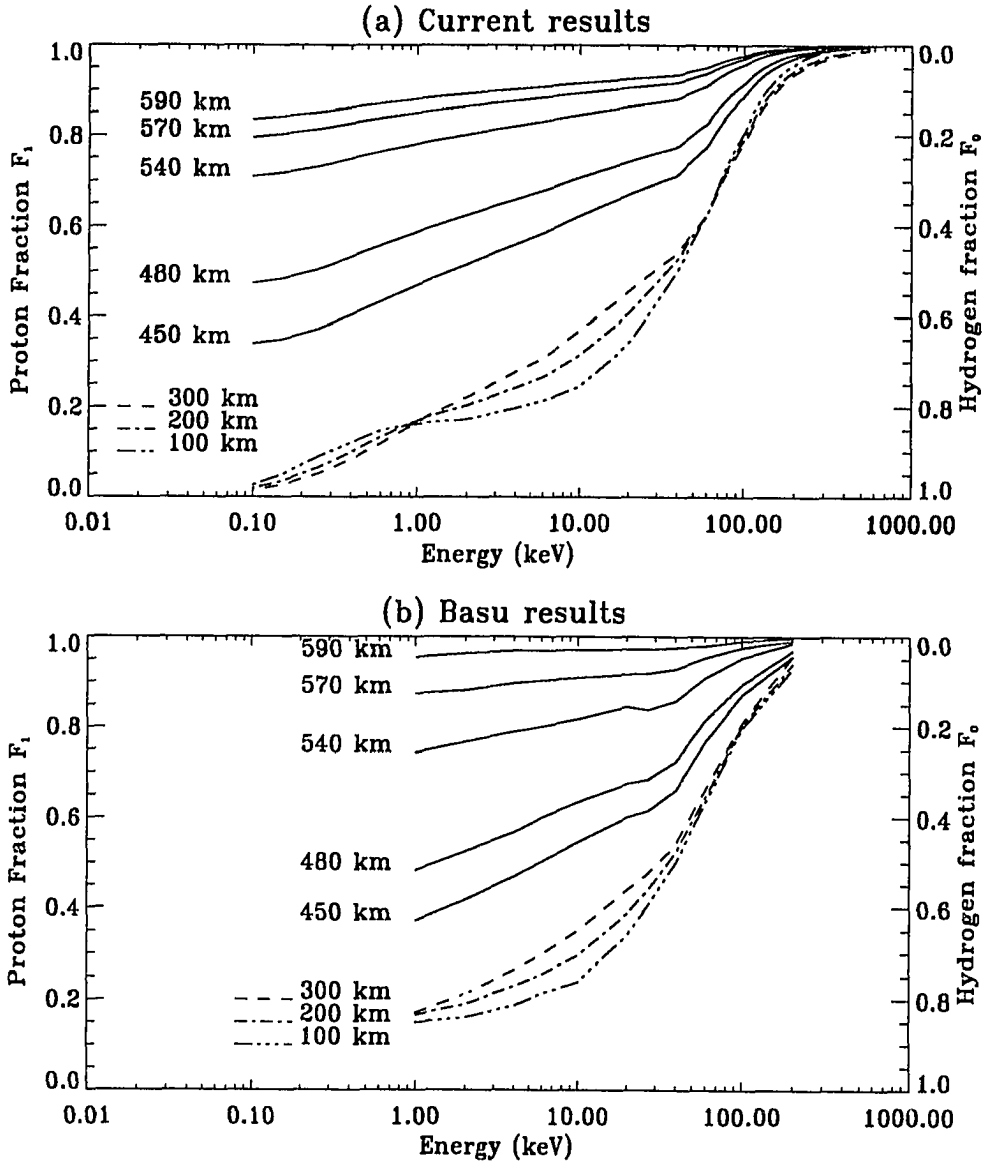

Figure 3.5: (a) Fraction of protons F_1, and hydrogen atoms, F_0, as a function of energy at several altitudes, for an input Maxwellian system with characteristic energy $E_0 = 10$ keV, and a total energy flux of 0.5 erg cm^{-2} s^{-1}, (b)Proton and H atom fractions calculated by Basu et al. (1990)

Figure 3.5(a) illustrates the conversion from protons to hydrogen atoms as the protons penetrate into the atmosphere. The fraction of protons in the mixture decreases with altitude and energy, the high energy protons being converted into low energy hydrogen atoms through charge exchange and energy degradation. Below the equilibrium altitude, the fraction of protons and hydrogen atoms in the mixture remains almost unchanged. Hydrogen atoms dominate the mixture for energies below about 40 keV. Almost all the protons are converted to hydrogen atoms at 0.1 keV because charge exchange cross sections are much larger than charge stripping cross sections at this energy. The two cross sections are approximately equal at about 40 keV, and above 40 keV, the fraction of protons is larger than that of hydrogen atoms at all altitudes because charge stripping cross sections are larger than charge exchange cross sections at energies above 40 keV.

The results of the present model are compared with those of Basu et al. (1990) in figure 3.5(b). The comparison can only be qualitative, because Basu et al. (1990) did not specify the parameters which determine the neutral atmospheric model. The neutral composition is a major factor that will affect the charge exchange rate, energy deposition and ionization rate. Different atmospheric models will give different results. In addition, Basu et al. (1990) did not include in the transport equations the mirror reflection term which will affect the relative fraction of protons and hydrogen atoms at high altitudes because protons reflected back up at high altitudes will most probably remain in the charged state due to the low density of neutral atmospheric species, and charge exchange processes are not important at high altitudes. Even so, figure 3.5 shows that in the energy range 1.0 keV to 600 keV, the two results are similar. Basu et al.'s (1990) calculations do not extend below 1.0 keV. Present calculations show a high fraction of hydrogen atoms at energies below 1.0 keV. The high hydrogen atom fraction in the energy range between 0.1 and 1.0 keV is important for the optical emissions of hydrogen atoms and will be discussed in chapter 4.

Basu et al. (1990) also argued that above the equilibrium altitude, energy degradation is not important as the neutral densities are low, thus, energy and particle loss can be neglected. If the energy losses are assumed to be zero in the transport equations, it is easy to show that the total particles are constant, all particles will just convert alternatively between charged and neutral states. By the time the equi-

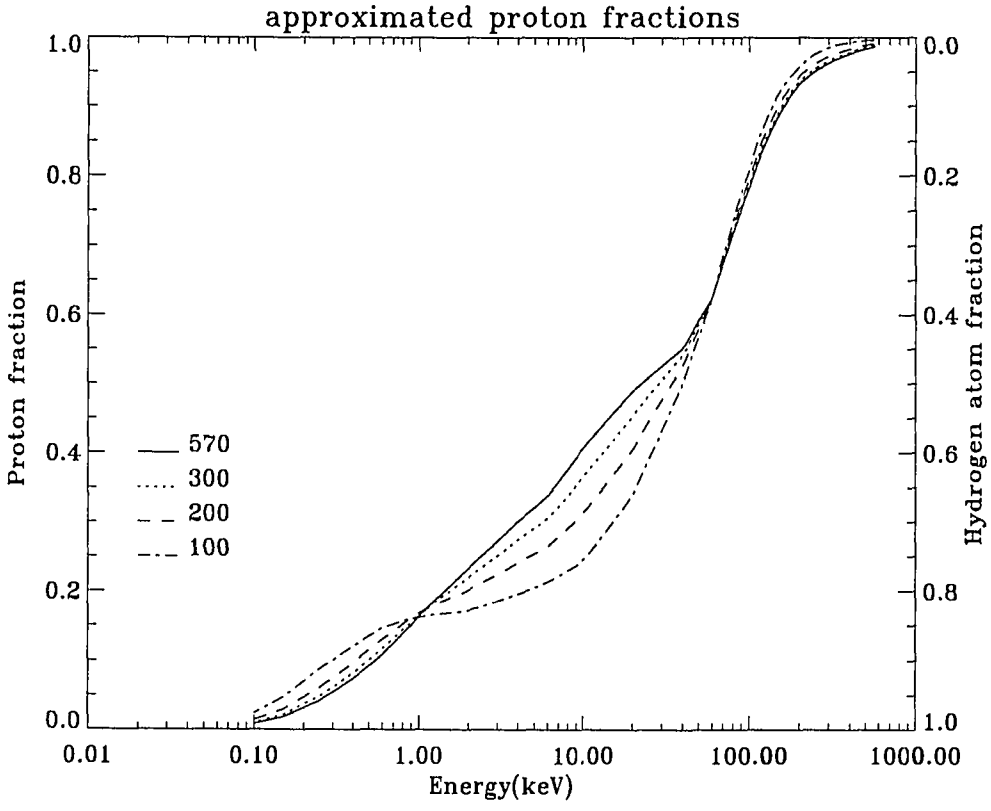

Figure 3.6: Proton and hydrogen atom fractions computed from equations 3.17 and 3.18.

librium state is reached, the equilibrated proton and hydrogen atom fractions can be approximated by the following forms:

$$F_1'(z,E) = \frac{\sum_s n_s(z)\sigma_s^{01}(E)}{\sum_s n(z)[\sigma_s^{01}(E)+\sigma_s^{10}(E)]} \quad (3.17)$$

$$F_0'(z,E) = 1 - F_1'(z,E) \quad (3.18)$$

where σ_s^{01} and σ_s^{10} are charge exchange and charge stripping cross section, respectively; n_s is the neutral density. The proton and hydrogen atom fractions as functions of energy at several altitudes are shown in figure 3.6. Comparing figure 3.6 with figure 3.5(a) shows that below the equilibrium altitude, which is about 300 km, the proton and hydrogen fractions calculated by equations 3.17 and 3.18 are

almost the same as those calculated from the transport equations, which shows that the approximate equations 3.17 and 3.18 can be used in calculating the equilibrated proton and hydrogen atom fractions if only the relative equilibrium fractions of protons and hydrogen atoms are desired. But at high altitudes, where equilibrium between protons and hydrogen atoms has not been reached, the transport equations have to be solved in order to calculate the relative fractions of proton and hydrogen atoms.

The hemispherically averaged particle intensities as a function of altitude at a given energy can also be calculated from the transport model. Figure 3.7 shows the hemispherically averaged particle intensities for a Maxwellian input spectrum of characteristic energy of 10.0 keV. The solid lines are proton intensities and the dotted lines are hydrogen atom intensities. The vertical solid lines are the input proton intensities. The graphs show that at low energies, hydrogen atoms dominate at low altitude, but at high energies, protons remain the dominant fraction.

3.3.3 Energy Deposition Rate

Energetic particles lose energy to the atmosphere through collisions with the background neutral species. At each collision a particle loses a certain amount of energy in the layer where the collision occurs. Summing over all collisional processes and integrating over all energies gives the total energy loss within that layer. However, the energy degradation calculation in proton transport is cut off at 0.1 keV, well above the thermal energy. Particles that accumulate at the lowest energy grid point still carry some kinetic energy that needs to be taken into account. The kinetic energy carried by particles at the lowest energy can be accounted for by using the total energy flux change method. Since at the lowest energy grid point, no further transport will be considered, the energy lost in each slab is equal to the net energy flux change in that slab. The energy deposition rate is thus calculated by the following formula:

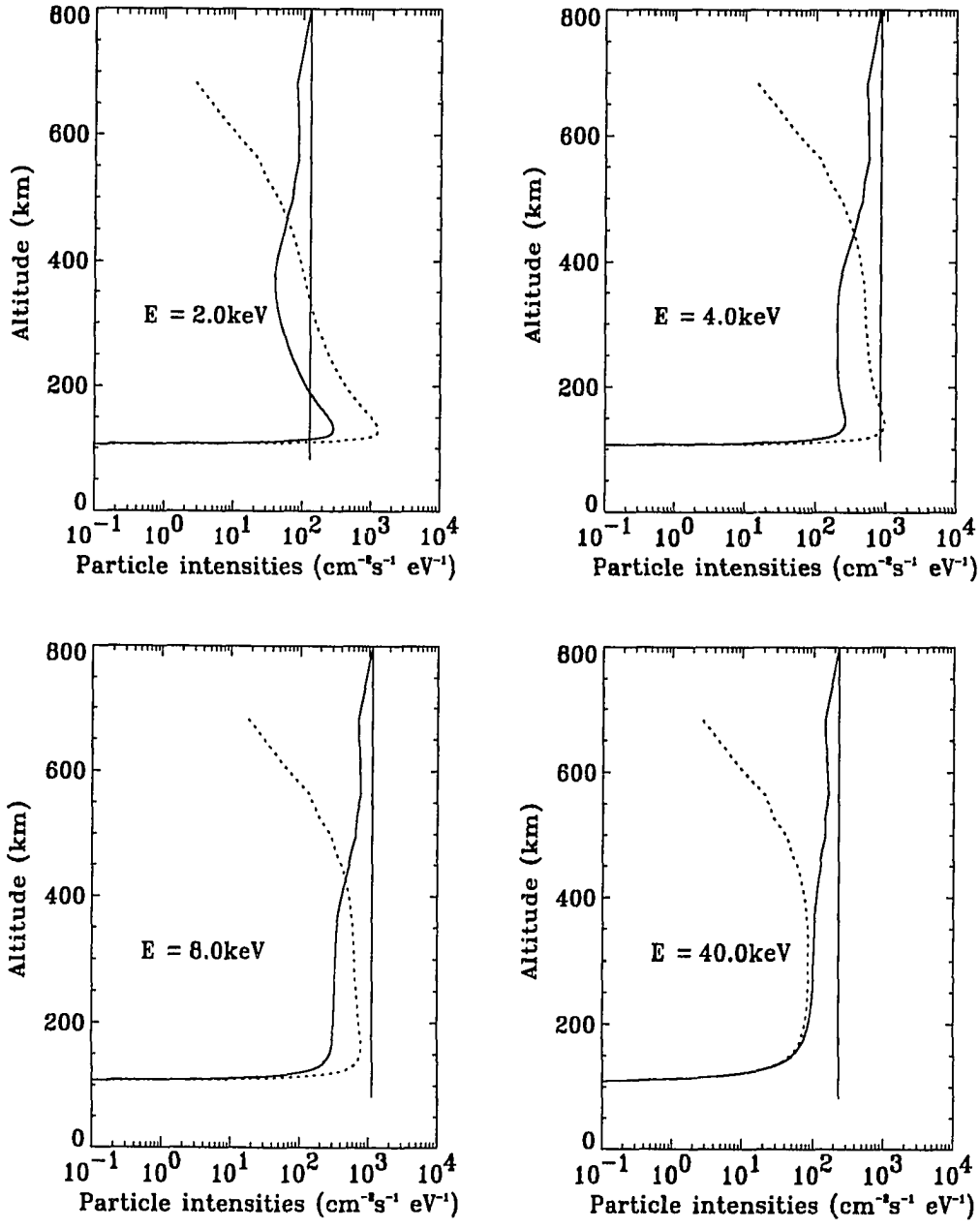

Figure 3.7: Hemispherically averaged proton and hydrogen atom intensities versus altitude for downward moving particles at some specific energy. Incident proton distribution is a Maxwellian with $E_0 = 10.0$ keV, total input energy flux is 0.5 erg cm^{-2} s^{-1}.

$$\eta'_E(z) = 2\pi \sum_s n_s(z) \Bigg\{ \int_{E_{min}}^{E_{max}} dE \sum_k \sigma^k_{s,p}(E) W^k_{s,p}(E) \int_{-1}^{1} d\mu \, I_p(z,E,\mu) + \int_{E_{min}}^{E_{max}} dE \sum_k \sigma^k_{s,H}(E) W^k_{s,H}(E) \int_{-1}^{1} d\mu \, I_H(z,E,\mu) \Bigg\} + \frac{\partial F(z,E_{min})}{\partial z} \quad (3.19)$$

where $F(z,E_{min})$ is the total energy flux at altitude z and energy E_{min}. The energy deposition rates calculated by summing over all energy loss processes as a function of altitude for Maxwellian input energy spectra with different characteristic energies are shown in figure 3.8. Figure 3.8 shows that the H^+/H stream deposits most of its energy at low altitudes, and the penetration depth depends on the characteristic energy of precipitating protons; the harder the spectrum, the deeper the protons can penetrate. Figure 3.9 presents the energy deposition rates calculated by Basu et al. (1990). The present model predicts penetration depths that are somewhat smaller than those obtained by Basu et al. (1990), while the peak values of energy deposition rate are larger than theirs because the present calculations do not include the spreading effect. Basu et al. (1990) used a reducing factor of 0.75 to account for the spreading effect. It was pointed out in section 2.2 that the spreading effect depends on the proton spectrum and on the ratio of arc width of precipitating proton streams to the scale height of the neutral atmosphere. These parameters need to be included in evaluating the spreading effect in transport calculations. Comparison between the present calculations with Basu et al.'s (1990) can only be qualitative since the neutral atmospheric parameters that affect the energy deposition rate are not the same.

3.3.4 Ionization Rate

Energetic protons and hydrogen atoms can ionize the atmospheric gases. In addition to the direct ionization reactions given by equations 2.3 and 2.4, the charge stripping process defined by equations 2.2 also produces electron-ion pairs, and is therefore, treated as an ionization process. The total ionization rate includes all processes that produce free electron-ion pairs. However, some previous calculations omitted the ionization produced by charge stripping. In their calculation of the ionization

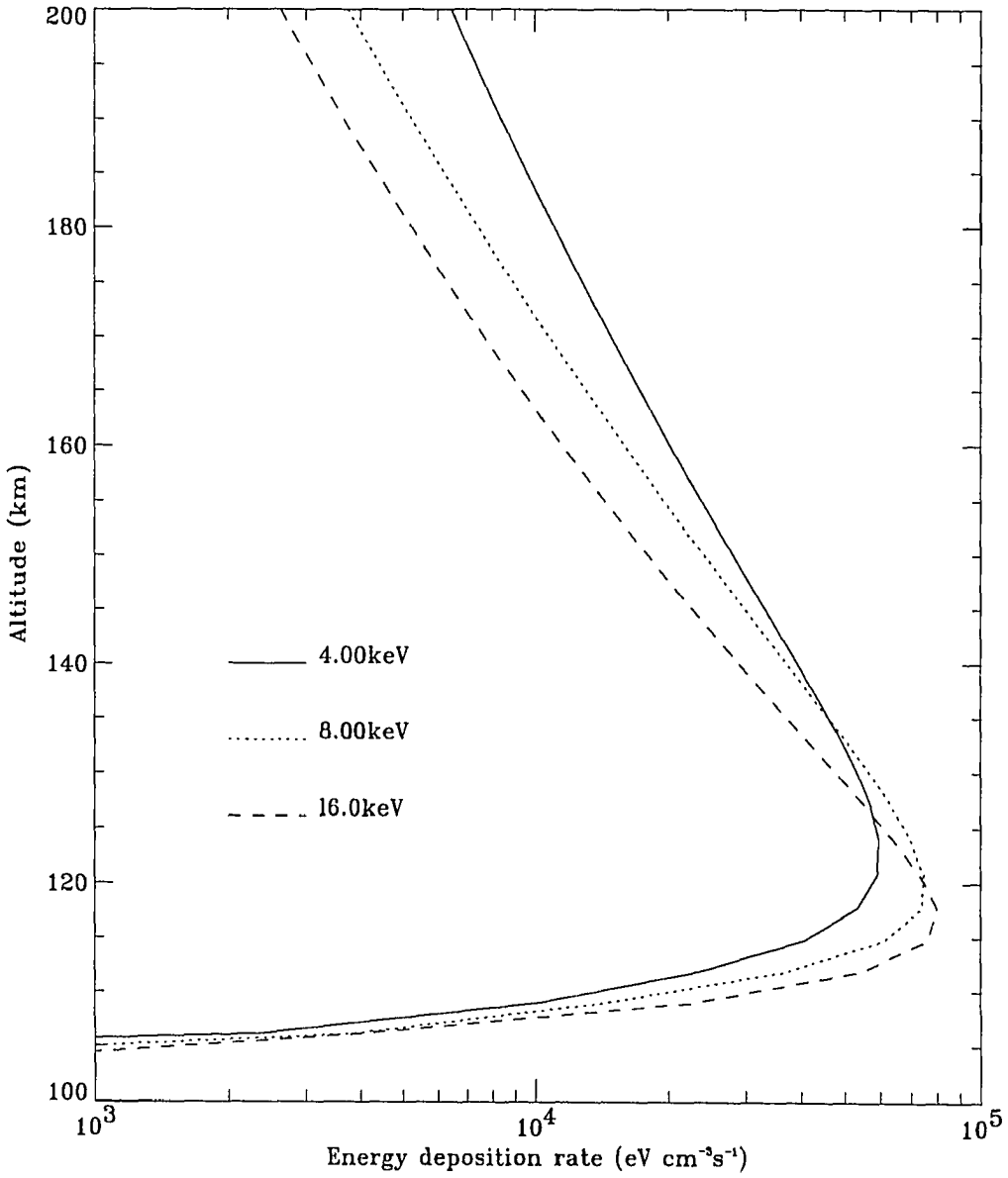

Figure 3.8: Altitude profiles of the energy deposition rate for a Maxwellian proton energy distribution with different characteristic energies E_0. The input energy flux is 0.5 erg cm^{-2}s^{-1}, and the pitch angle distribution is isotropic.

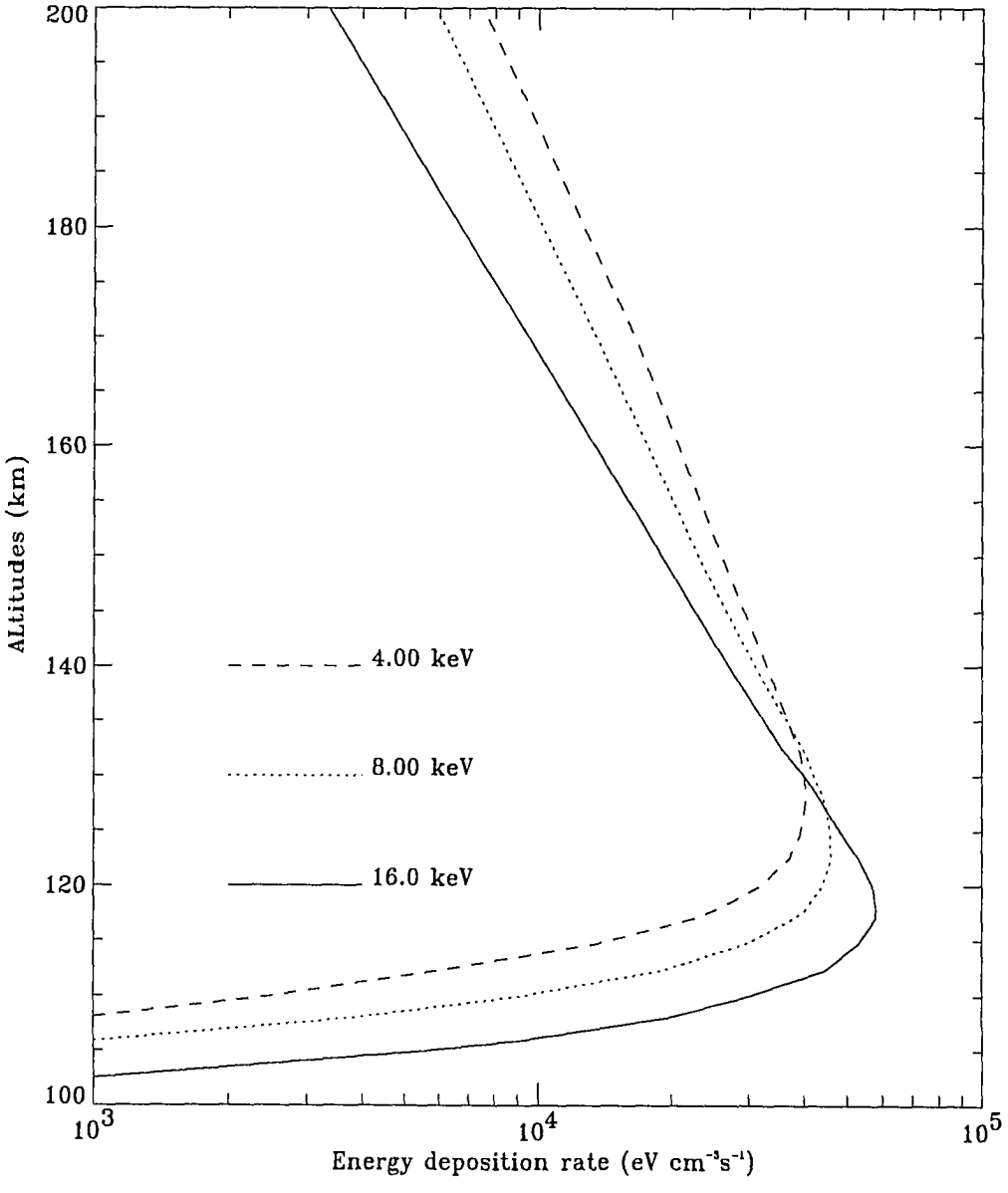

Figure 3.9: Energy deposition rate versus altitude obtained from Basu et al. (1990). The input energy flux is 0.5 erg cm^{-2}s^{-1} and the pitch angle distribution is also isotropic. A factor of 0.75 has been applied to account for the spreading effect discussed in section 2.2.

rate, Basu et al. (1990) included the charge exchange process which, however, does not produce a free electron-ion pair.

With the calculated particle fluxes and the measured ionization cross sections of neutrals due to proton and hydrogen atom impact, the ionization rate is calculated as a function of altitude by the following formula:

$$\eta_I(z) = 2\pi \sum_s \int_{E_{min}}^{E_{max}} dE \int_{-1}^{1} d\mu \left\{ \sigma^i_{s,P}(E) I_p(z,E,\mu) + \left[\sigma^i_{s,H}(E) + \sigma^{01}_s(E)\right] I_H(z,E,\mu) \right\} \quad (3.20)$$

where the superscript i denotes ionization, and $\sigma^{01}_s(E)$ is the charge stripping cross section.

The ionization rates for Maxwellian input spectra with different characteristic energies, E_0, are shown in figure 3.10(a). The altitude of peak ionization is a function of characteristic energy E_0, the larger E_0, the deeper the H^+/H beam penetrates. For comparison, figure 3.10(b) presents the ionization rate excluding the contribution by charge stripping collisional processes. It it is evident that charge stripping contributes a significant fraction of the total ionization, with the amount dependent on the characteristic energy, E_0.

3.3.5 Energy Conservation Test

A numerical scheme is usually evaluated by its accuracy, stability, and efficiency. The current model is very efficient, it can be run in several minutes, and its stability is almost automatically maintained by the second order implicit method (Potter, 1972). The accuracy of the model can be tested by comparing the calculations with the experimental data in chapter 4. The calculations also must conserve energy.

The energy deposition rate is used to check energy conservation. Integrating the energy deposition rate over altitude gives the total energy absorbed. Energy conservation requires that the energy deposited in the atmosphere should equal the energy input at the top of the atmosphere minus the energy reflected back out at the top of the atmosphere. The total energy deposited in the atmosphere Q_d is obtained by integrating the energy deposition rate over altitude.

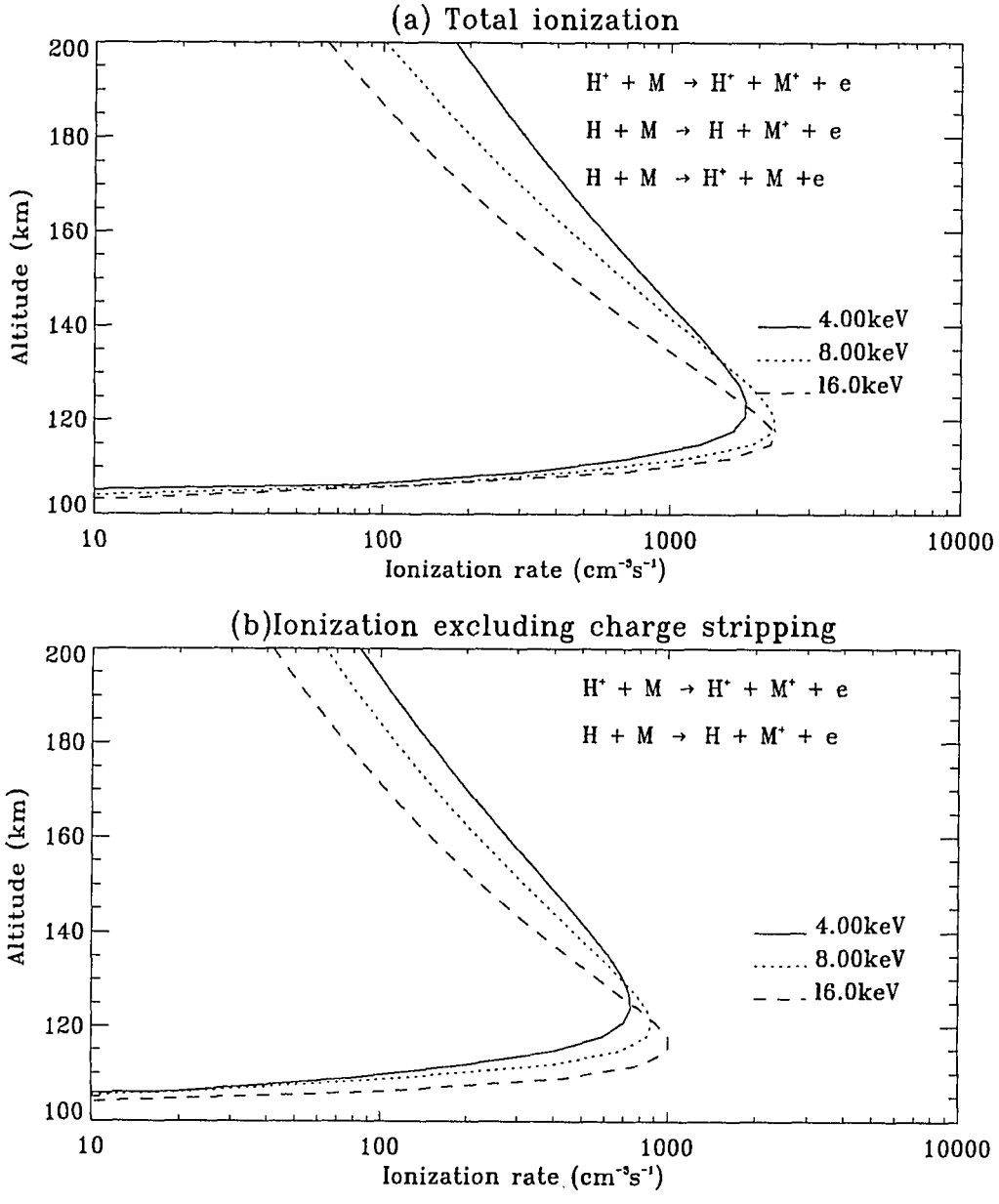

Figure 3.10: Ionization rates due to proton precipitation. The input energy distribution is Maxwellian and the pitch angle distribution is isotropic. The input energy flux is 0.5 erg $cm^{-2}s^{-1}$. (a) total ionization rate, (b)ionization rate excluding the charge stripping contribution.

Table 3.1: Energy Conservation for Maxwellian distributions

input energy(Q_0) ($eVcm^{-2}s^{-1}$)	deposited(Q_d) ($eVcm^{-2}s^{-1}$)	reflected(Q_r) ($eVcm^{-2}s^{-1}$)	energy E_0 (keV)	(B_q)
3.125e+11	2.679e+11	0.422e+11	4.00	0.8%
3.125e+11	2.644e+11	0.433e+11	8.00	1.5%
3.125e+11	2.607e+11	0.447e+11	16.0	2.3%
3.125e+11	2.557e+11	0.468e+11	32.0	3.2%

$$Q_d = \int \eta'_E(z)\, dz \tag{3.21}$$

where $\eta'_E(z)$ is energy deposition rate given by equation 3.19 The energy Q_r reflected back out of the top of the atmosphere can be calculated by the upward particle intensities,

$$Q_r = 2\pi \int_{E_{min}}^{E_{max}} E\, dE \int_0^1 \mu\, d\mu \{I_p(z_0, E, \mu) + I_H(z_0, E, \mu)\} \tag{3.22}$$

$$\tag{3.23}$$

Labeling the input energy flux by Q_0, an energy conservation parameter B_q is defined by

$$B_q = \frac{Q_0 - Q_r - Q_d}{Q_0} * 100\% \tag{3.24}$$

Table 3.1 shows the energy conservation parameter for Maxwellian spectra of different characteristic energies. The pitch angle distribution of the input protons is isotropic, and the total input energy flux is maintained constant. Energy conservation achieved by the present transport model is better than 5.0 percent.

The beam spreading effect discussed in section 2.2 does not affect energy and particle conservation because the atmosphere is represented by a semi-infinite plane. The particles are either deposited in the atmosphere or reflected back out of the atmosphere. The spreading effect may affect the fraction that is reflected and deposited but not the total particle and energy fluxes.

Chapter 4

Optical Emissions by Hydrogen Atoms

4.1 Introduction

The hydrogen Balmer lines in auroral spectra were first detected at Oslo by Vegard (1939); he identified the H_α and H_β lines, and on one occasion he found a diffuse line that peaked 5Å to the short wavelength side of the normal H_β wavelength (4861Å). Much later, this observation was interpreted by Vegard (1948) as due to the Doppler displacement of the emission by hydrogen atoms. Approaching the earth with considerable velocity, protons are neutralized and excited through encounters with background atmospheric atoms and molecules. Since then, many observations as well as laboratory investigations and theoretical studies have been made to use the hydrogen emission as a tool to study the impact of protons upon the atmosphere during aurora. In fact, the optical emissions of hydrogen atoms were the only direct evidence of the type of particle entering the earth's atmosphere during aurora before the discovery of X-ray radiation in and near the auroral zones (Meredith et al., 1955) and the establishment of a direct association between aurora and X-rays. Many workers believed that the particles were accelerated into the earth's atmosphere and were therefore probably of only one sign. Thus, it was considered that some auroral arcs could be entirely due to protons (Chamberlain, 1954a, b), and much work went into the study of hydrogen emissions from aurora. However, experimental difficulties in the measurement of weak emissions frequently

lead to observations that were difficult to analyze quantitatively.

Today, satellites and rockets can measure the auroral particles directly, and optical emission cross sections of hydrogen atoms due to various collisional processes of H^+/H with the background atmospheric species are available. It is possible, therefore, to model the transport of auroral protons, and to study the mechanism of the auroral emissions by hydrogen atoms. The satellite or rocket measured proton fluxes can be used to calculate the hydrogen emissions excited by these energetic auroral protons passing through the atmosphere, using the transport model developed in preceding chapters, and compare the calculated emission rates with either ground-based observations or satellites and rockets measurements.

4.2 Excitation Processes and Emission Cross Sections of Hydrogen Atoms

4.2.1 Excitation Processes

When protons enter the atmosphere their energy is degraded through inelastic collisions, ionizing and exciting the atmospheric molecules and atoms. In a process called charge exchange, or electron capture, the product hydrogen atom may be in an excited state which is written in the following form:

$$H^+ + M \rightarrow H(nl) + M^{+(*)} \tag{4.1}$$

Here n is the main quantum number and l the orbital quantum number of the hydrogen atom. The processes have different cross-sections $\sigma_{10}(nl)$ for electron capture into different levels nl. Another excitation process is direct collision between the hydrogen atoms in the ground state and atmospheric atoms and molecules (M), described by:

$$\begin{aligned} H + M &\rightarrow H(nl) + M \\ &\quad or \quad H(nl) + M^+ + e \end{aligned} \tag{4.2}$$

with $\sigma_{00}(nl)$ denoting the excitation cross sections to different states nl. The excited hydrogen atoms H(nl) produced in the different types of collisions will emit

Lyman and Balmer series radiations in transitions down to the ground state and first excited state, respectively. This thesis considers only the Balmer lines because line profiles have only been measured for H_α and H_β. The emissions of the Lyman series are stronger than those of Balmer series, but these can not be measured from the ground due to strong atmospheric absorption. All other series of hydrogen atomic lines are too weak to study. Due to the low density of hydrogen in the atmosphere, the contribution of energetic electron impact on H to line emissions is negligibly small, so only contributions from H^+/H impact on neutral species are considered.

The proton and hydrogen atom intensity distributions result from the transport calculations. Once the excitation cross sections $\sigma_{10}(nl)$ and $\sigma_{00}(nl)$ are known, the production rates of hydrogen atoms in different states nl can be calculated. Laboratory measurements yield optical emission cross sections for various lines and in the following calculations, only optical emission rates of Balmer lines are given.

4.2.2 Emission Cross Sections of H_α and H_β

The H_α and H_β emission cross sections for collisions of H and H^+ projectiles with neutral species N_2, O_2 have been measured by several investigators, but no measurements have as yet been reported of the emission cross sections for collisions of H^+/H projectiles with oxygen atoms. Fortunately, the hydrogen emissions originate in the lower part of the atmosphere where the densities of N_2 and O_2 are larger than that of O. A rough estimate of the cross sections for collisions with O would not cause an appreciable error. The emission cross sections adopted in this thesis have been measured by Van Zyl and Neumann (1980) for energies between 0.1 keV and 3.0 keV, while for energies above 3.0 keV, the data are from Yousif et al. (1986). The H_α emission cross sections are shown in figure 4.1, and listed in table 4.1. The H_β emission cross sections are shown in figure 4.2, and the experimental data points are collected in table 4.2; the data points are by courtesy of Sigernes (1992) who obtained them from Van Zyl through a private communication.

4.3 Excitation of N_2

Molecular band emissions belonging to the first-negative (1N) system of N_2^+ (the $B^2\Sigma_u^+ \rightarrow X^2\Sigma_g^+$ electronic transition) and the second positive (2P) system of N_2 (the

Table 4.1: H_α emission cross sections for collisions of H^+/H with neutral species

Energy	H impact on			H^+ impact on		
	N_2	O_2	O	N_2	O_2	O
(keV)	(cm^2)	(cm^2)	(cm^2)	(cm^2)	(cm^2)	(cm^2)
4.0e-2	4.45e-18	1.13e-18	5.65e-19	2.20e-21	1.06e-19	5.30e-20
5.0e-2	7.24e-18	2.81e-18	1.41e-18	4.40e-21	2.49e-19	1.25e-19
6.3e-2	9.37e-18	4.69e-18	2.35e-18	8.80e-21	5.02e-19	2.51e-19
8.0e-2	1.03e-17	5.88e-18	2.94e-18	1.79e-20	9.55e-19	4.78e-19
1.0e-1	1.13e-17	6.91e-18	3.45e-18	3.39e-20	1.62e-18	8.10e-19
2.0e-1	2.10e-17	1.38e-17	6.90e-18	2.02e-19	3.19e-18	1.59e-18
4.0e-1	3.88e-17	2.37e-17	1.18e-17	1.04e-18	6.63e-18	3.32e-18
6.3e-1	4.60e-17	2.65e-17	1.33e-17	2.21e-18	7.61e-18	3.81e-18
1.0e+0	4.32e-17	2.62e-17	1.31e-17	4.10e-18	8.75e-18	4.37e-18
2.0e+0	3.25e-17	2.32e-17	1.16e-17	8.09e-18	1.11e-17	5.55e-18
3.2e+0	2.63e-17	2.05e-17	1.02e-17	1.08e-17	1.17e-17	5.85e-18
4.0e+0	2.43e-17	1.90e-17	.950e-17	1.17e-17	1.18e-17	5.90e-18
5.0e+0	2.25e-17	1.78e-17	8.90e-18	1.25e-17	1.19e-17	5.95e-18
6.3e+0	2.11e-17	1.63e-17	8.06e-18	1.32e-17	1.21e-17	6.05e-18
1.0e+1	1.90e-17	1.46e-17	7.30e-18	1.40e-17	1.30e-17	6.50e-18
2.0e+1	1.62e-17	1.21e-17	6.11e-18	1.63e-17	1.33e-17	6.55e-18
3.2e+1	1.38e-17	1.05e-17	5.25e-18	1.54e-17	1.18e-17	5.90e-18
4.0e+1	1.26e-17	9.61e-18	4.81e-18	1.30e-17	1.01e-17	5.01e-18
6.3e+1	1.04e-17	7.98e-18	3.99e-18	7.68e-18	6.14e-18	3.07e-18
1.0e+2	8.38e-18	6.42e-18	3.21e-18	3.55e-18	2.84e-18	1.42e-18
2.0e+2	5.59e-18	4.28e-18	2.14e-18	.575e-18	.460e-18	.230e-18
4.0e+2	3.26e-18	2.50e-18	1.25e-18	.501e-19	.401e-19	.200e-19
6.3e+2	2.20e-18	1.69e-18	.845e-18	1.02e-20	.820e-20	.410e-20
1.0e+3	1.45e-18	1.11e-18	.555e-18	.200e-20	.160e-20	.800e-21

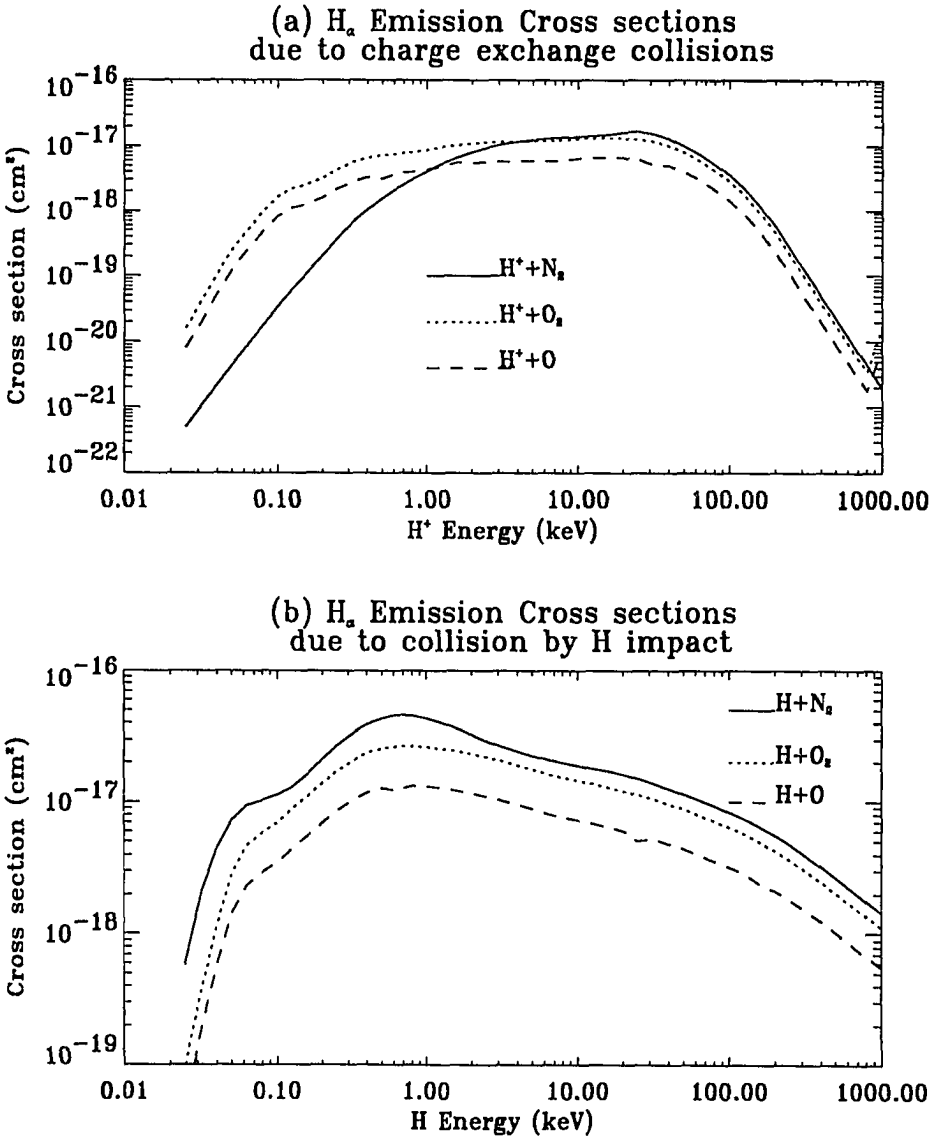

Figure 4.1: H_α Emission cross sections of neutral species, (a) charge exchange processes, (b) impact excitations.

Table 4.2: H_β emission cross sections for collisions of H^+/H with neutral species

Energy	H impact on			H^+ impact on		
	N_2	O_2	O	N_2	O_2	O
(keV)	(cm^2)	(cm^2)	(cm^2)	(cm^2)	(cm^2)	(cm^2)
4.0e-2	.432e-18	.090e-18	.045e-19	.200e-21	.900e-20	.450e-20
5.0e-2	.833e-18	.257e-18	.128e-18	.400e-21	.212e-19	.106e-19
6.3e-2	1.34e-18	.513e-18	.256e-18	.900e-21	.427e-19	.213e-19
8.0e-2	1.81e-18	.776e-18	.388e-18	.180e-20	.812e-19	.406e-19
1.0e-1	2.18e-18	1.04e-18	.520e-18	.340e-20	.138e-18	.690e-19
2.0e-1	3.98e-18	2.19e-17	1.09e-18	.202e-19	.271e-18	.135e-18
4.0e-1	7.10e-18	4.03e-17	2.02e-17	.104e-18	.564e-18	.282e-18
6.3e-1	8.79e-18	4.89e-17	2.45e-17	.221e-18	.647e-18	.323e-18
1.0e+0	8.89e-18	5.31e-17	2.65e-17	.410e-18	.744e-18	.372e-18
2.0e+0	7.74e-18	5.54e-17	2.77e-17	.848e-18	1.01e-17	.505e-18
3.2e+0	6.86e-18	5.35e-17	2.68e-17	1.22e-18	1.18e-17	.590e-18
4.0e+0	6.61e-18	5.17e-17	2.58e-17	1.41e-17	1.30e-17	.650e-18
5.0e+0	6.30e-18	4.98e-17	2.49e-18	1.63e-17	1.44e-17	.720e-18
6.3e+0	6.08e-18	4.70e-18	2.35e-18	1.88e-17	1.62e-17	.810e-18
1.0e+1	5.64e-18	4.33e-18	2.16e-18	2.42e-17	2.15e-17	1.08e-18
2.0e+1	4.83e-18	3.61e-18	1.80e-18	3.55e-17	2.86e-17	1.43e-18
3.2e+1	4.04e-18	3.07e-18	1.58e-18	3.67e-17	2.81e-17	1.40e-18
4.0e+1	3.68e-18	2.81e-18	1.40e-18	3.16e-17	2.45e-17	1.23e-18
6.3e+1	3.03e-18	2.32e-18	1.16e-18	1.89e-18	1.51e-18	.755e-18
1.0e+2	2.45e-18	1.88e-18	.940e-18	.873e-18	.699e-18	.350e-18
2.0e+2	1.67e-18	1.28e-18	.640e-18	.141e-18	.113e-18	.565e-19
4.0e+2	1.02e-18	.782e-18	.391e-18	.123e-19	.099e-19	.050e-19
6.3e+2	.697e-18	.535e-18	.268e-18	.250e-20	.020e-19	.010e-19
1.0e+3	.464e-18	.355e-18	.178e-18	.500e-21	.400e-21	.200e-21

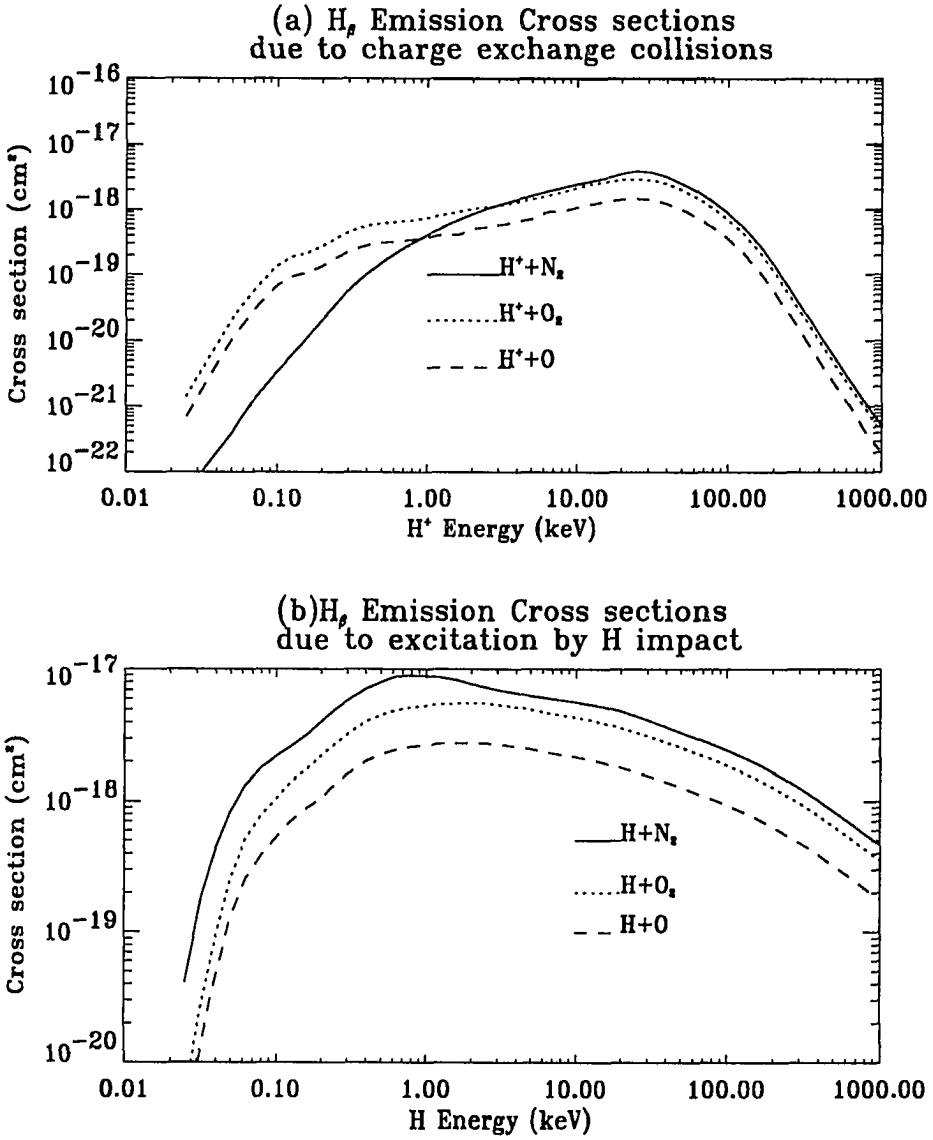

Figure 4.2: Emission cross section of H_β due to (a)charge exchange collisions, (b) impact excitation collisions.

$C^3\Pi_u \rightarrow B^3\Pi_g$ electronic transition) are among the most intense and easily observed atmospheric emissions in proton aurora (Omholt, 1971; Vallance Jones, 1974). The reactions are as follows:

$$\begin{aligned} H^+/H + N_2 &\rightarrow N_2^+(B^2\Sigma_u^+) + H^+/H + e \\ &\quad | \\ &\rightarrow N_2^+(X^2\Sigma_g^+) + h\nu(3914\text{Å}) \qquad (4.3) \\ H + N_2 &\rightarrow N_2(C^3\Pi_u) + H \\ &\quad | \\ &\rightarrow N_2(B^3\Pi_g) + h\nu(3371\text{Å}) \qquad (4.4) \end{aligned}$$

Excitation of the $C^3\Pi_u$ state from the singlet ground state by H^+ impact has been neglected in equation (4.4) because the transition is formally forbidden according to the Wigner spin conservation rule (Thomas, 1972), and the cross sections for the process will be very small. Dahlberg et al. (1967) and Thomas et al. (1968) have measured the cross section for the emission of 3371Å from the transition $C^3\Pi_u \rightarrow B^3\Pi_g$ of N_2 due to proton impact. The results show that the emission cross section of the second positive system is indeed very small. Dahlberg et al. (1967) also measured the 3371Å emission cross section of the second positive system of N_2 molecules due to hydrogen impact, and found the cross sections to be much smaller than the cross sections of 3914Å emission of first negative band of N_2^+. In this work I will not discuss the second positive emission processes.

The cross sections for emission of the first negative bands by H^+ and H collisions with N_2 have been measured by Van Zyl et al. (1983) over the range of H^+/H energies of interest for proton auroral analysis. Figures 4.3 (a) and (b) give the emission cross sections of the $N_2^+1N(0,0)$ band due to H^+ and H impact on N_2, respectively. The curves are composites of several sources: (a) $H^+ + N_2$ collision data are from Van Zyl et al. (1983) for projectile energies below 2.0 keV, and from Carleton and Lawrence (1958) for energies above 2.0 keV and below 4.0 keV, from Philpot and Hughes (1964) for energies between 10.0 and 100.0 keV, and from Sheridan el at. (1971) for energies between 4.0 and 20.0 keV, and above 100.0 keV. (b) For $H + N_2$ collisions, the measurements are from Van Zyl et al. (1983) for energies below 2.0 keV; from Birely (1974) for energies between 1.0 keV and about

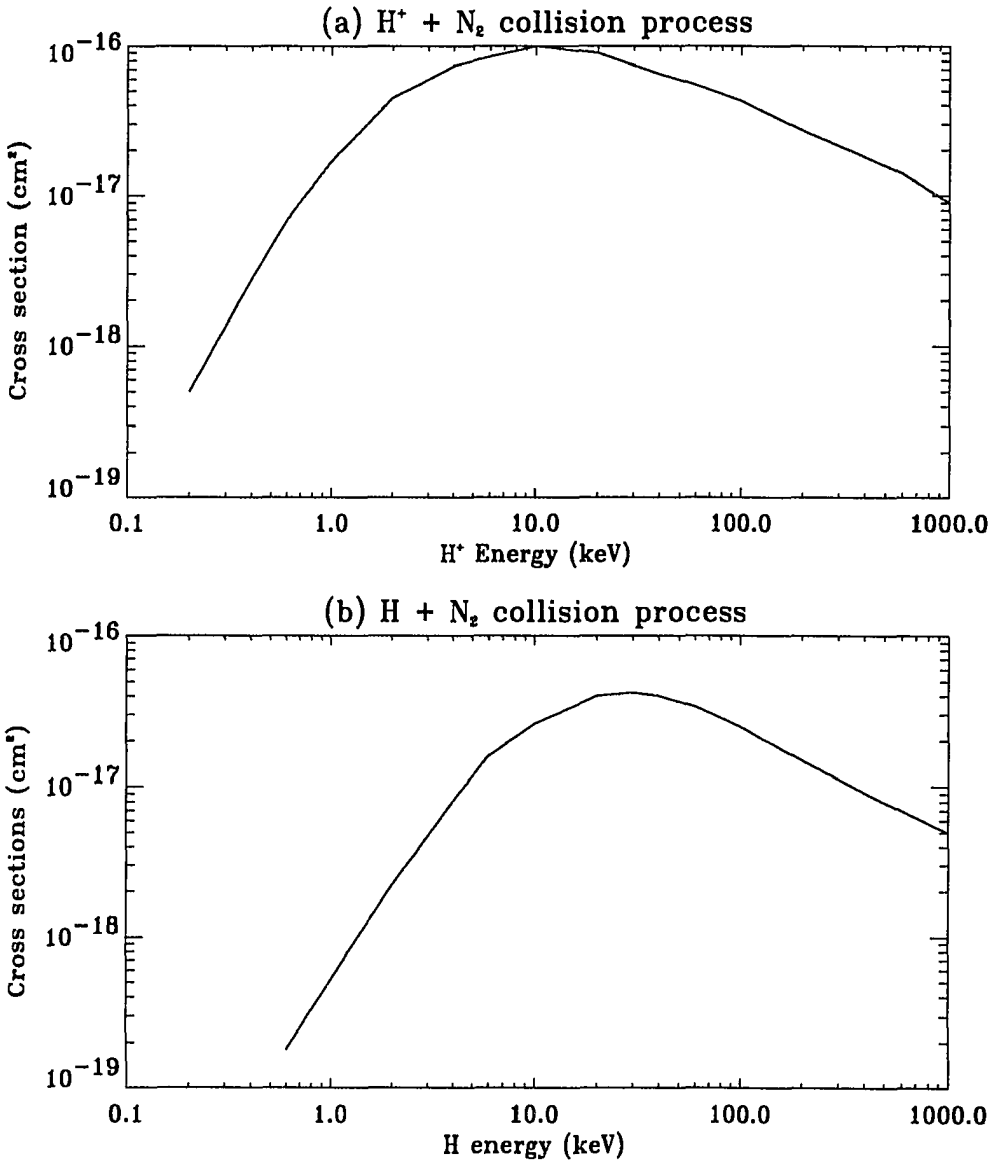

Figure 4.3: Cross sections for N_2^+ 1N(0,0) band emission for (a) $H^+ + N_2$ collisions, (b) $H + N_2$ collisions.

10.0 keV; from McNeal and Clark (1969) and Dahlberg et al. (1967) for energies above 10.0 keV to about 100.0 keV; the curves are extrapolated above 100.0 keV.

4.4 Volume Emission Rate of H_α,H_β and N_2^+

With the above emission cross sections and the H^+/H intensities calculated from the transport equations, the volume emission rate of the hydrogen lines can be calculated by:

$$R^k(z) = 2\pi \sum_s n_s(z) \int_{E_{min}}^{E_{max}} dE \int_{-1}^{1} d\mu \left[\sigma^k_{s,p}(E) I_p(z,E,\mu) + \sigma^k_{s,H}(E) I_H(z,E,\mu)\right] \tag{4.5}$$

where $\sigma^k_{s,p}$, and $\sigma^k_{s,H}$ are emission cross sections due to charge exchange and impact excitation, respectively, and k represents different hydrogen emission lines. The densities of the major constituents, denoted by subscripts s, at altitude z are $n_s(z)$. The integration over pitch angle μ runs from -1 to 1 because both downward and upward moving particles will contribute to the observed emissions. Figures 4.4 and 4.5, respectively, show volume emission rates of H_α and H_β lines for input Maxwellian differential energy spectra with different characteristic energies E_0. These two figures show that the hydrogen emissions peak at different altitudes for different proton input spectra; the harder the proton spectra, the deeper the emissions peak in the atmosphere.

Integration of equation 4.5 over altitude gives the column emission rate observed along the magnetic field line. It is this integrated intensity that is measured by satellites and rockets viewing along a magnetic field line above altitude, z. The emission rate of H_α and H_β as function of characteristic energy E_0 is shown in table 4.3 for three different pitch angle distributions. Table 4.3 shows that for the same energy spectrum, the total emission also depends on the pitch angle distributions. Forward peaked protons will penetrate deeper than those at large pitch angles, thus contribute more optical emissions.

For N_2^+ first negative band emission, the volume emission rate formula is:

$$R_{vv'}(z) = 2\pi n(z) \int_{E_{min}}^{E_{min}} dE \int_{-1}^{1} d\mu \left[\sigma_p^{vv'}(E) I_p(z,E,\mu) + \sigma_H^{vv'}(E) I_H(z,E,\mu)\right] \tag{4.6}$$

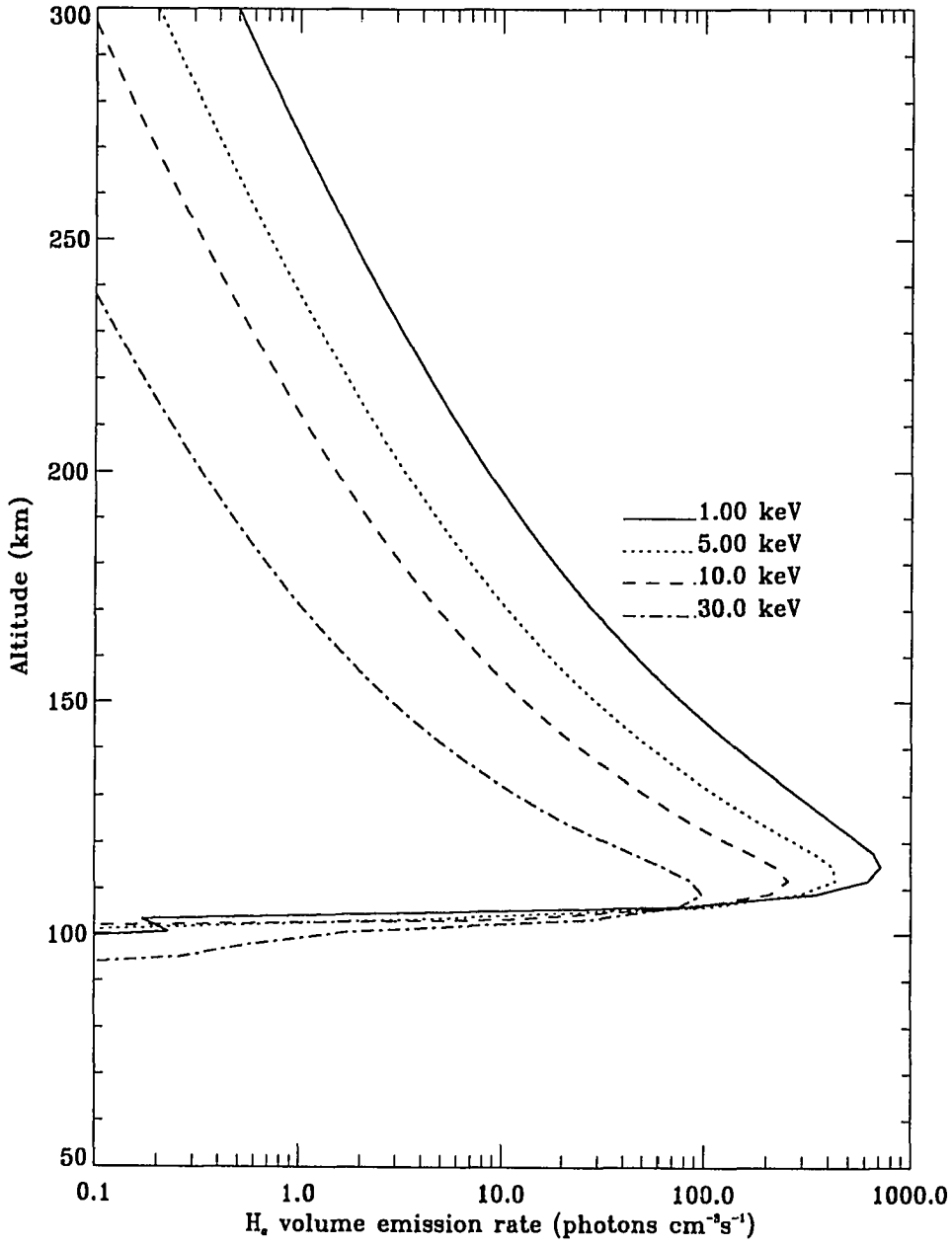

Figure 4.4: Volume emission rate of the H_α line for input Maxwellian differential energy spectra with various characteristic energies E_0. The total input energy flux is 0.5 erg cm^{-2} s^{-1}, the angular distribution is isotropic.

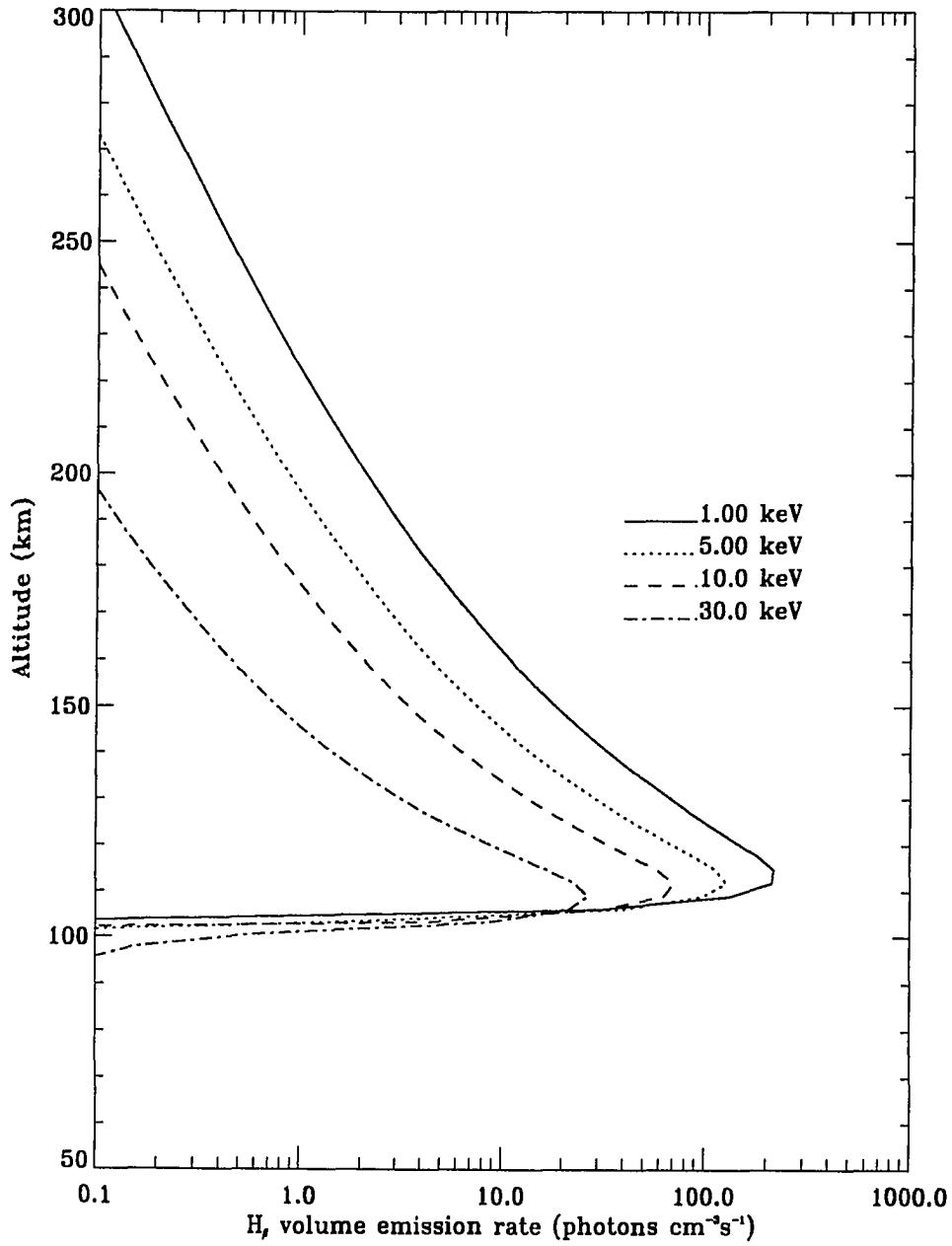

Figure 4.5: Volume emission rate of the H_β lines for input Maxwellian differential energy spectra with various characteristic energies E_0. The total input energy flux is 0.5 erg cm^{-2} s^{-1}, the angular distribution is isotropic.

Table 4.3: The column emission rates of H_α and H_β as function of characteristic energy. The total input energy flux is 0.5 ergs/cm^2/s.

E_0	Forward peak		Isotropic		Pancake	
keV	H_α(R)	H_β(R)	H_α(R)	H_β(R)	H_α(R)	H_β(R)
1.00	3715.8	1051.8	3659.3	1035.1	3598.0	1017.1
3.00	1450.6	399.0	1422.2	390.89	1392.0	382.26
5.00	903.13	247.22	882.90	241.49	861.64	235.47
10.0	467.23	127.59	454.45	124.01	441.19	120.30
20.0	240.04	65.32	231.64	63.00	223.01	60.61
30.0	161.83	43.91	155.15	42.08	148.33	40.22
50.0	97.04	26.23	92.15	24.90	87.19	23.56

where $\sigma_p^{vv'}$, $\sigma_H^{vv'}$ are emission cross sections of the $N_2^+1N(v,v')$ band for proton and hydrogen atom impact on N_2, respectively, $n(z)$ is the density of N_2, $I_p(z,E,\mu)$ and $I_H(z,E,\mu)$ are the proton and hydrogen atom intensities calculated in the transport equations. The calculated volume emission rate for the $N_2^+1N(0,0)$ band is shown in figure 4.6.

The column emission rates of H_α, H_β and $N_2^+1N(0,0)$ band are shown in figure 4.7 as function of the average energy of Maxwellian input spectra with an isotropic pitch angle distribution. Figure 4.7(a) gives the emission rate per unit energy flux, while figure 4.7(b) shows the emission rate per unit proton particle flux. The average energy is twice the characteristic energy E_0 for a Maxwellian spectrum. A comparison between the present results and those of Van Zyl et al. (1984) is shown in table 4.4. For hard spectra (large E_0), the current results are close to Van Zyl's et al. (1984), but for softer spectra (small E_0), the photons/proton values are larger than Van Zyl's et al. (1984). A possible explanation is that a mixed atmosphere (N_2, O_2, and O) is used here, while Van Zyl et al. just used N_2. The two atmospheres yield different H^+/H equilibrium values because the charge exchange and charge stripping cross sections of O_2 and O have different shapes from that of N_2.

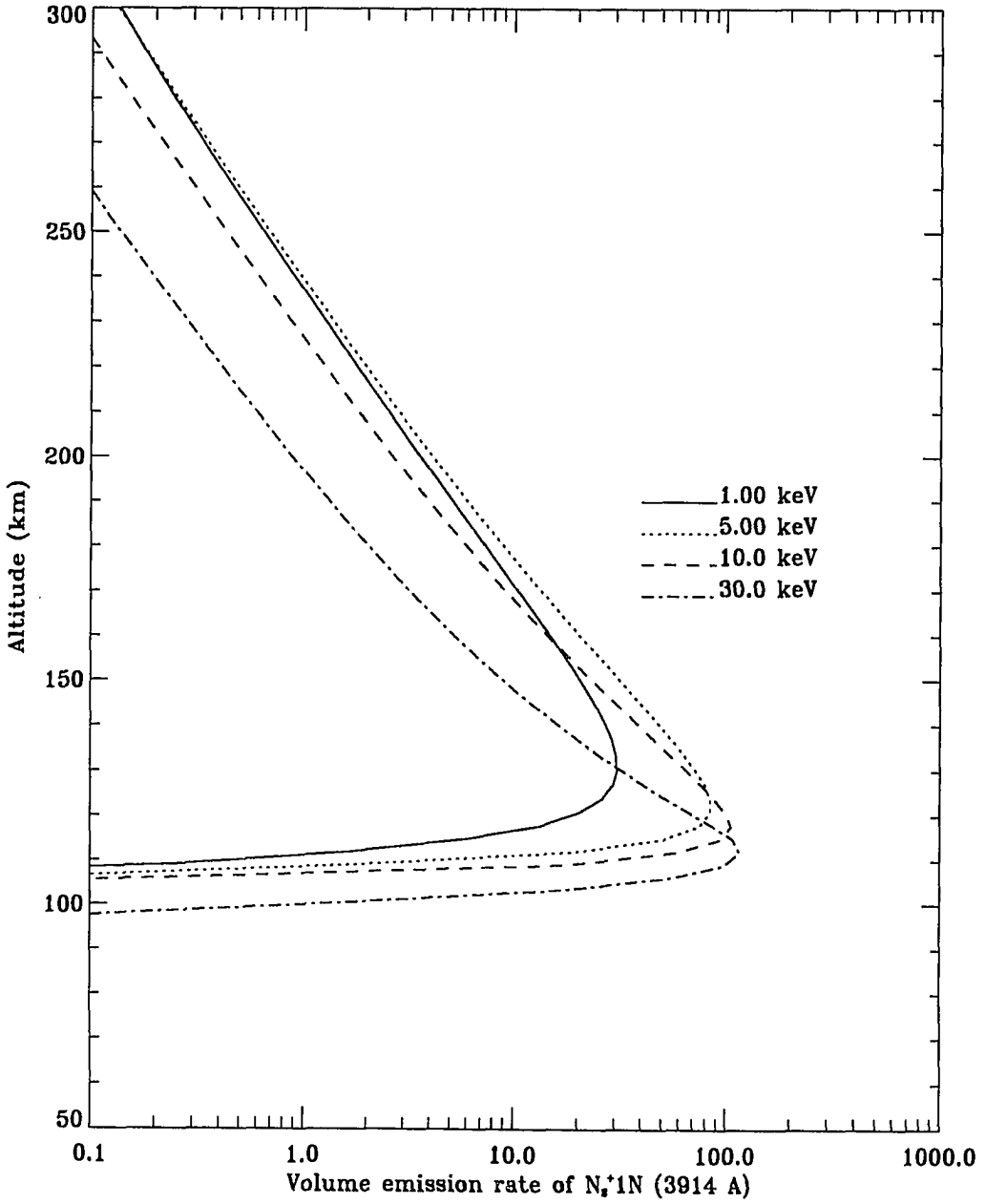

Figure 4.6: Volume emission of the N_2^+1N (0,0) by H^+/H impact excitation. An input Maxwellian energy distribution with energy flux 0.5 erg cm^{-2} s^{-1} was adopted in the model calculations. The pitch angle distribution of input protons is isotropic.

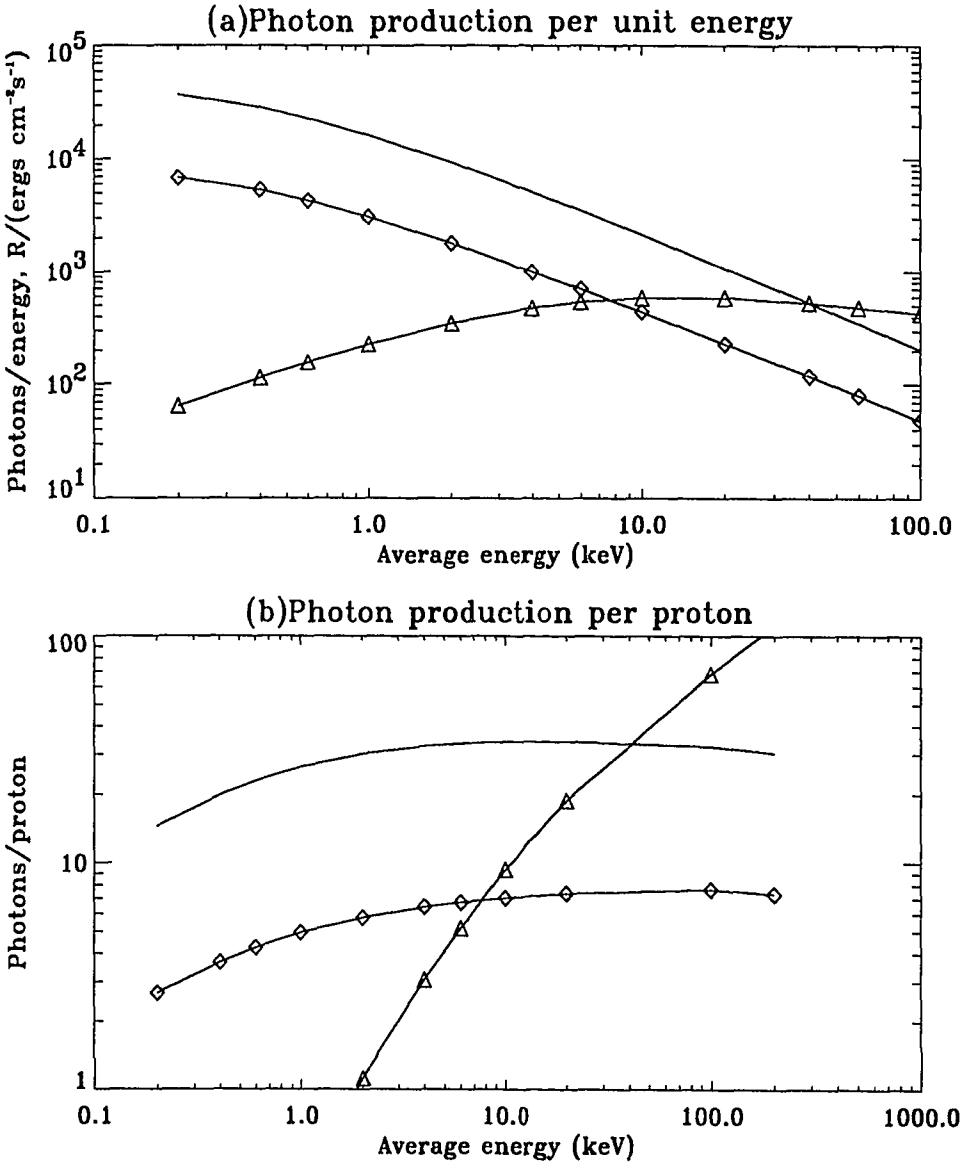

Figure 4.7: Column emission rate of H_α, H_β and $N_2^+1N(0,0)$ band, (a) emission per unit energy flux, (b) emission per proton particle flux as function of average energy. Solid line —- H_α, ◇ —- H_β; △—- $N_2^+1N(0,0)$ band.

Table 4.4: Production of H_α and H_β photons per primary H^+ incident on the neutral atmosphere during a simulated proton auroral shower as function of E_0, the characteristic energy of a Maxwellian distribution. The pitch angle distribution of energetic H^+ is isotropic.

E_0	Total H_α		Total H_β	
keV	Present	Van Zyl	Present	Van Zyl
0.10	14.483	0.944	2.665	0.162
0.20	19.78	2.05	3.65	0.36
0.30	22.90	3.02	4.24	0.54
0.50	26.42	4.71	4.94	0.86
1.00	30.20	7.43	5.76	1.36
2.00	32.74	10.8	6.42	2.03
3.00	33.63	12.8	6.73	2.49
5.00	34.14	15.7	7.03	3.20
10.0	34.23	20.8	7.35	4.41
20.0	33.90	26.7	7.61	6.11
30.0	33.52	30.9	7.70	7.23
50.0	32.63	36.6	7.67	8.71
100.	30.50	43.9	7.32	10.8

For a single species N_2 atmosphere, the percentage of H is about 80% in the low energy range, while in a mixed atmosphere, the percentage of H can reach 100% for energies below 1.0 keV. The emission cross sections of H_α and H_β peak at about 1.0 keV, and it is the hydrogen atoms that produce most of the optical emissions due to the large excitation cross sections. With a larger fraction of hydrogen atoms in a mixed neutral atmosphere, the total optical emission will be much larger than that in a pure N_2 atmosphere even though N_2 makes up about 70% of the total atmosphere. Another difference between the present results and Van Zyl's et al. is that the efficiency of hydrogen emission (photons per input proton or per input energy)

in the present calculation has a peak as a function of the characteristic energy of the input proton flux, while Van Zyl's et al. efficiencies increase monotonically.

The ratios H_α/H_β, $H_\beta/N_2^+1N(0,0)$ as function of characteristic energy E_0 are also calculated and shown in figure 4.8. From figure 4.8(a), it can be seen that the ratio of H_α to H_β changes very little with different average energies, because the emission cross sections of H_α and H_β have almost the same shape. Because most emission occurs below the equilibrium altitude, the ratios can also be estimated from the equilibrium H^+/H distribution. Using the equilibrium H^+/H distribution given by equation 3.17 and 3.18, and combining the emission cross sections with the density of neutral species, the intensity ratios of H_α/H_β, and $H_\beta/N_2^+1N(0,0)$ can be estimated as in figure 4.8(b). The estimated results for $H_\beta/N_2^+1N(0,0)$ are similar to those calculated with the transport code over part of the projectile energy range, which lends confidence to the numerical calculations of the optical emissions.

4.5 Effects of Secondary Electrons

Secondary electrons produced by H^+/H ionizations of atmospheric molecules and atoms may also ionize N_2 molecules, and excite the $N_2^+1N(0,0)$ bands. The secondary electron distribution can be calculated by using equation (2.24), but this formula is derived for ionization by H^+ impact. No corresponding data are available for $H + N_2$ collisions. Since the hydrogen atom flux fraction F_0 is larger than proton flux fraction F_1 in typical proton aurora (see Figure 3.5), ignoring secondary e^- production by hydrogen atom impact would be unrealistic. Using the results of Rudd et al. (1980), Van Zyl et al. (1984) treated ionization by fast H as the sum of two separate processes: ionization by the H^+ nucleus , and ionization by the atom's orbital electron, which is assigned an effective kinetic energy $m_e v_h^2/2$, where m_e is the electron mass and v_h is the H atom velocity. In the present calculations, the electron production rate due to hydrogen impact on neutrals is assumed to be the same as that due to H^+ impact collisions. The production spectrum for a Maxwellian input spectrum of protons is shown in figure 4.9 as function of secondary electron energy at different altitudes. Figure 4.10 shows the production rate spectrum of secondary electrons as a function of proton characteristic energy E_0 at an altitude of 120 km.

The above calculated electron production rates can be used as an embedded

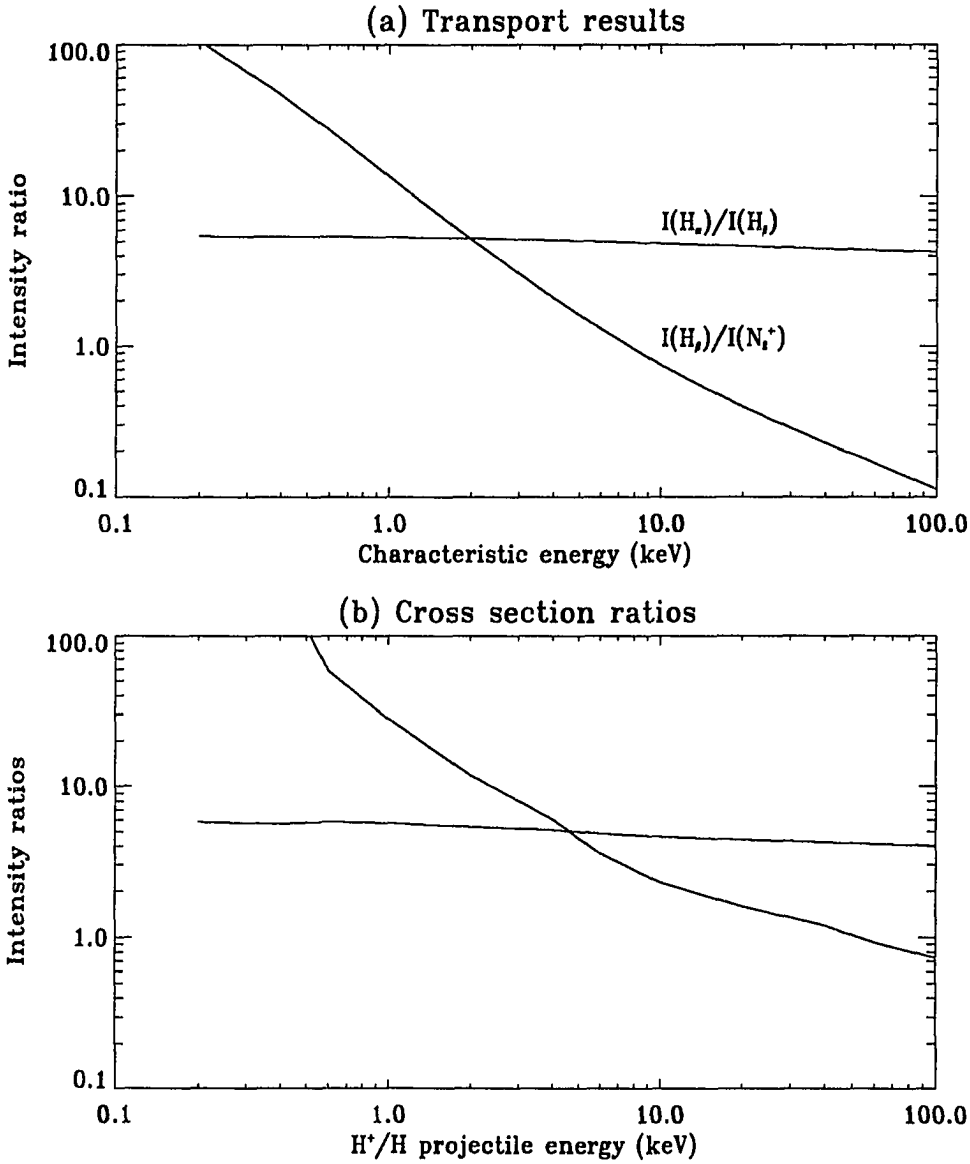

Figure 4.8: Auroral intensity ratios for H_α, H_β and $N_2^+1N(0,0)$ band emissions as functions of characteristic energy for proton precipitation with a Maxwellian energy spectrum, (a) transport equation results, (b) values estimated from cross sections.

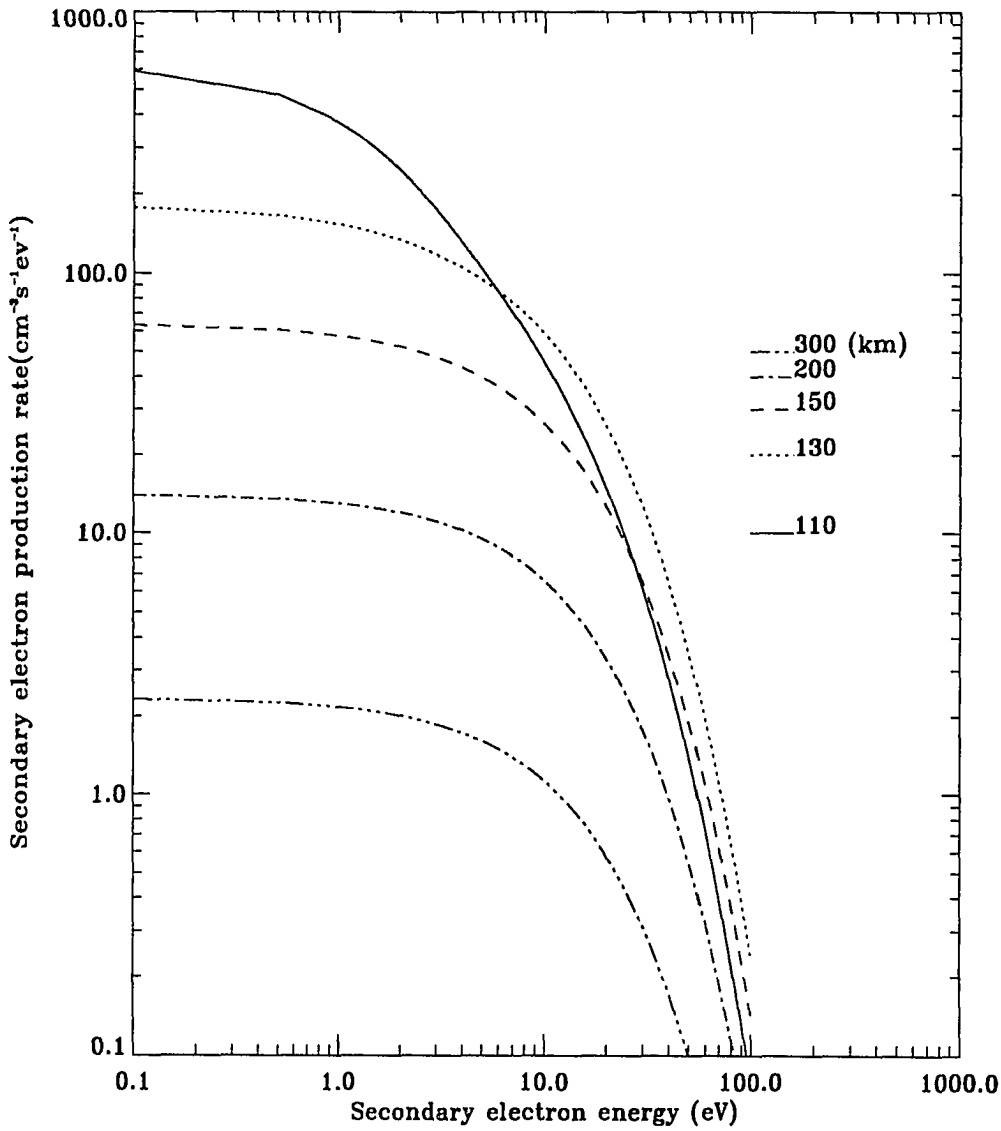

Figure 4.9: Secondary electron production rate as a function of electron energy at different altitudes. A Maxwellian energy spectrum with the characteristic energy 10 keV and an input flux 0.5 erg cm^{-2} s^{-1} is adopted for the proton precipitation.

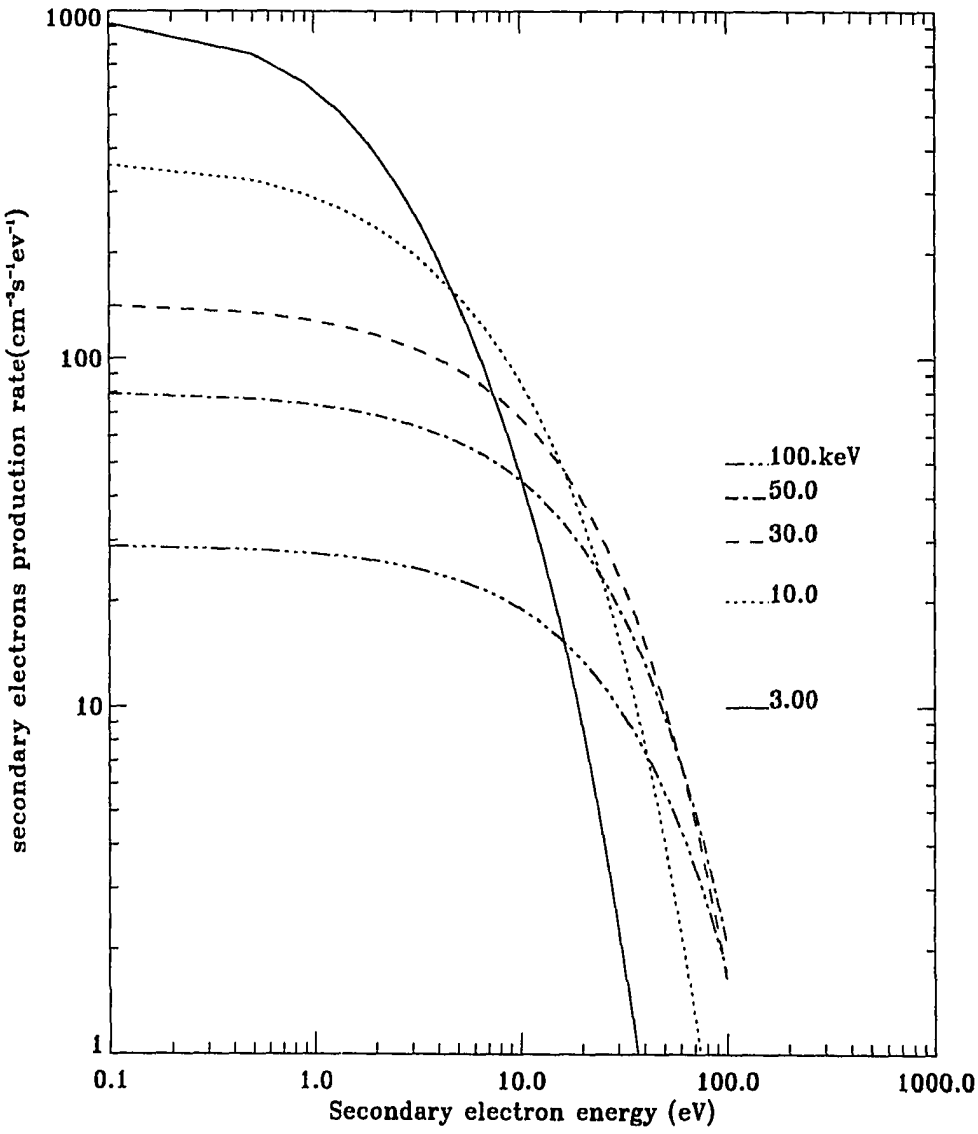

Figure 4.10: Secondary electron production rate at 120 km for Maxwellian proton energy spectra with different characteristic energies.

source in an electron aurora transport code (e.g. Lummerzheim, 1987) to calculate the electron flux due solely to proton precipitation, and to calculate optical emissions produced by the secondary electrons. The electron production rate in proton aurora can also be included in an electron transport code to study the coupled electron, proton and hydrogen atom aurora. It should be noted, however, that the electron production rate due to charge stripping of hydrogen atoms has been neglected in the present calculations because no information is available on the production spectrum of electrons. The magnitude of the charge stripping cross sections is similar to the impact ionization cross sections. Moreover, an electron produced by ionization of neutral species stripping the fast H will maintain a forward velocity component acquired from the H velocity, and is thus more energetic than electrons from ionization of neutral species by either H^+ or H impact. Experimental work is required to measure the electron production cross section due to charge stripping collisions of hydrogen with neutral atmospheric atoms and molecules.

4.6 Line Profile of H-Balmer Emissions

Auroral proton precipitation is a source of ionization, neutral heating, and excitation of both H atoms and atmospheric species. The velocity of the H atoms is sufficiently large to produce a Doppler shift in the H emissions. Indeed, observations of the Doppler shifted H-Balmer lines in the aurora half a century ago provided direct evidence for aurorally associated proton precipitation. The Doppler profile of the hydrogen lines has be used as a tool to study the distribution of protons in pitch angle and energy (Eather, 1966, 1967b; Omholt, 1971; Vallance Jones, 1974). Progress in developing a satisfactory proton aurora theory to explain the observed line characteristics has been very slow due to the complication of proton and hydrogen atom transport. It is now straightforward to calculate the Doppler profiles of the hydrogen lines and to compare the predicted profiles with observations by using the solution of transport equations.

(i)Magnetic-zenith profiles

With particle fluxes calculated from the transport equations (see chapter 3) and the emission cross sections summarized in preceding sections, total emission of hydrogen atoms can be calculated. Due to the motion of the emitters, an observer

sitting in a laboratory frame will see a Doppler shifted emission spectrum. For a hydrogen atom of velocity v at pitch angle μ, the nonrelativistic Doppler effect produces an observed wavelength that is related to the unshifted wavelength, λ_0, by

$$\begin{aligned} \lambda &= \frac{\lambda_0}{1-\frac{v_s}{c}} \\ &= \frac{\lambda_0}{1-\frac{v\mu}{c}} \end{aligned} \tag{4.7}$$

λ_0= 6563Å for H_α, and 4861Å for H_β, respectively. c is the speed of light, μ is the cosine of energetic H^+/H pitch angle. Negative μ represents downward moving particles which will produce a blue shift, while positive μ is for upward moving particles which gives a red shift. $v_s = v\mu$ is the velocity component of H^+/H along the line of sight. The velocity of v is related to the particle energy, E, by $E = \frac{1}{2}mv^2$. The Doppler shifted wavelength, λ, depends both on the velocity and on the pitch angle of energetic particles. For a given energy, the pitch angle distribution will form a set of wavelength distribution determined by equation 4.7. Using a finite difference method of solution, the emission due to a specific stream of pitch angle μ at a given altitude z and for a specific energy E_i can be calculated as follows:

$$g(z, E_i, \mu) = 2\pi n_s(z)\left\{\sigma^k_{s,p}(E_i) I_p(z, E_i, \mu) + \sigma^k_{s,H}(E_i) I_H(z, E_i, \mu)\right\}\Delta\mu \tag{4.8}$$

where $\Delta\mu$ is the finite grid size of μ. The emission can also be expressed in wavelength space as:

$$\phi(z, E_i, \lambda)\Delta\lambda \tag{4.9}$$

where $\Delta\lambda$ is the grid size of wavelength λ determined from equation 4.7 for a specific velocity v_i (energy E_i). Equations 4.8 and 4.9 represent functions in two different phase spaces that combine to yield the line profile $\phi(z, E_i, \lambda)$ as a function of wavelength at given energy E_i and altitude z,

$$\begin{aligned} \phi(z, E_i, \lambda) &= g(z, E_i, \mu)/\Delta\lambda \\ &= 2\pi n_s(z)\left\{\sigma^k_{s,p}(E_i) I_p(z, E_i, \mu) + \sigma^k_{s,H}(E_i) I_H(z, E_i, \mu)\right\}\frac{\Delta\mu}{\Delta\lambda} \end{aligned} \tag{4.10}$$

Summing $\phi(z, E_i, \lambda)$ over energy and altitude yields the magnetic zenith line

profile $\phi(\lambda)$. The normalized zenith profiles of H_α and H_β are shown in figures 4.11 and 4.12 for a proton input flux with a Maxwellian spectrum and isotropic pitch angle distribution. For different characteristic energies, the shift of the peak does not change, which is consistent with most observations (Eather, 1967b). The line shift is independent of the incident spectrum because precipitating protons penetrate into the lower atmosphere where energy degradation processes become important, and the resulting low energy component of the hydrogen intensity is independent of the initial proton energy spectrum. These low energy hydrogen atoms contribute most to the optical emissions. Figure 4.11 and 4.12 show an emission peak shift of about 3 Å for H_α and about 2Å for H_β, toward the blue side of the unshifted emission.

The computed emission on the red side of the unshifted line (vertical line in figure 4.11) is very small compared to the emission on the blue side, and only becomes apparent when the profile is displayed on a logarithmic scale, shown in figure 4.12. The calculations of the Doppler shift can not be carried below the energy cut-off at 0.1 keV adopted in the transport calculations. The Gaussian quadrature integration does not yield a point at exactly 90 degrees. The discontinuous inputs to the calculated profile result in a wavelength gap that include λ_0. Therefore, the diagonal lines which cross λ_0 in figures 4.11 and 4.12 are not real and only serve to guide the eye.

The calculated red shifted emission is much smaller than the observed H_α red shifted emission shown in figure 4.13. Figure 4.13 shows the zenith and horizon line profiles measured at the Poker Flat, Alaska, optical observatory on 20 January 1977, with a one meter Ebert-Fastie scanning spectrophotometer. Since the measured line profiles do not change much with the type or intensity of the aurora, it should be safe to compare the calculated line profiles with any measured one. This requires convolving the idealized profiles with the broadening function of the instrument. For an Ebert-Fastie spectrometer, the instrument function has a triangular shape, and can be represented analytically:

$$\begin{aligned} g(\lambda) &= \frac{1}{2\Delta\lambda}\left(1 - \frac{\lambda - \lambda_i}{\Delta\lambda}\right) \qquad (for \|\lambda - \lambda_i\| \leq \Delta\lambda) \\ &= 0 \qquad\qquad (for \|\lambda - \lambda_i\| > \Delta\lambda) \end{aligned} \tag{4.11}$$

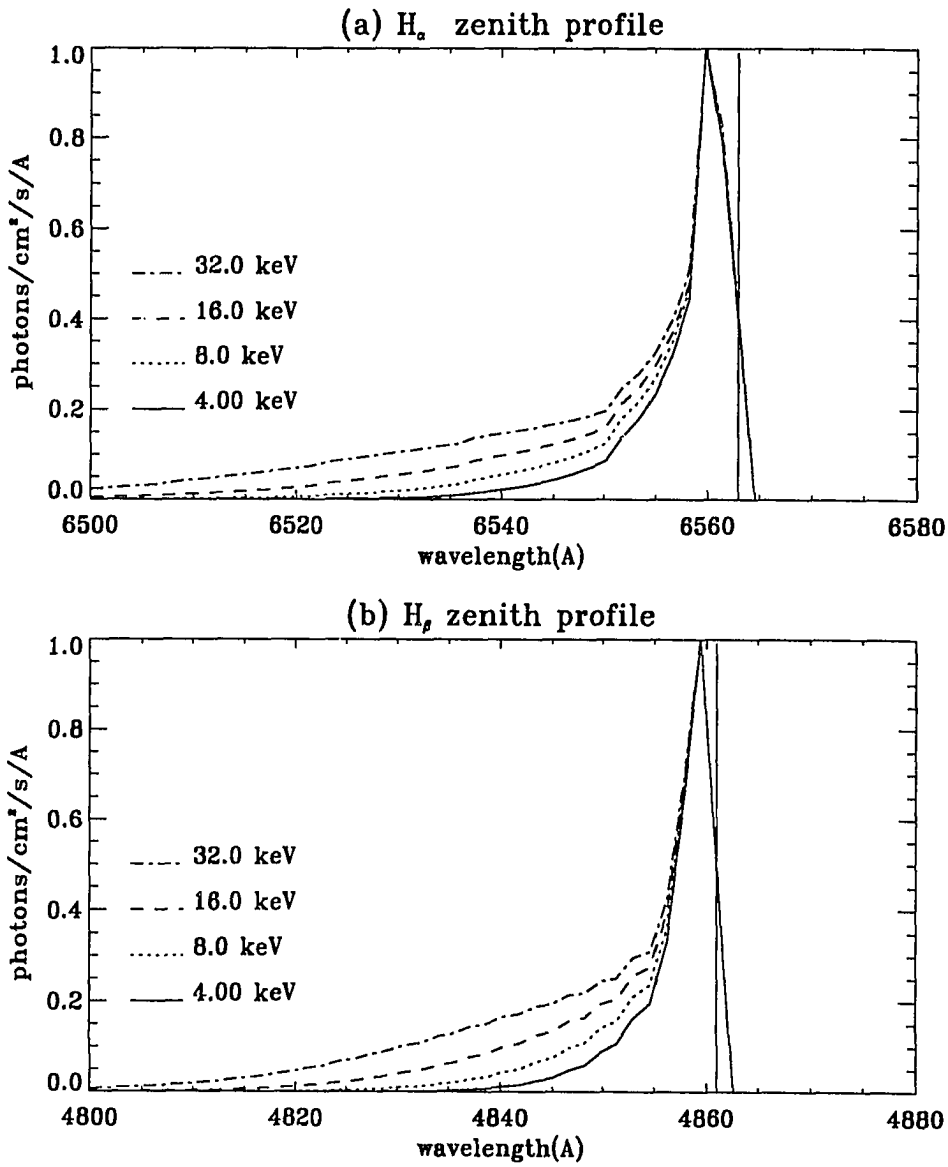

Figure 4.11: Normalized line profiles (in linear scale) of H_α and H_β calculated from an input of Maxwellian proton spectra with different characteristic energies E_0 = 4.0, 8.0, 16.0, and 32.0 keV and an isotropic pitch angle distributions.

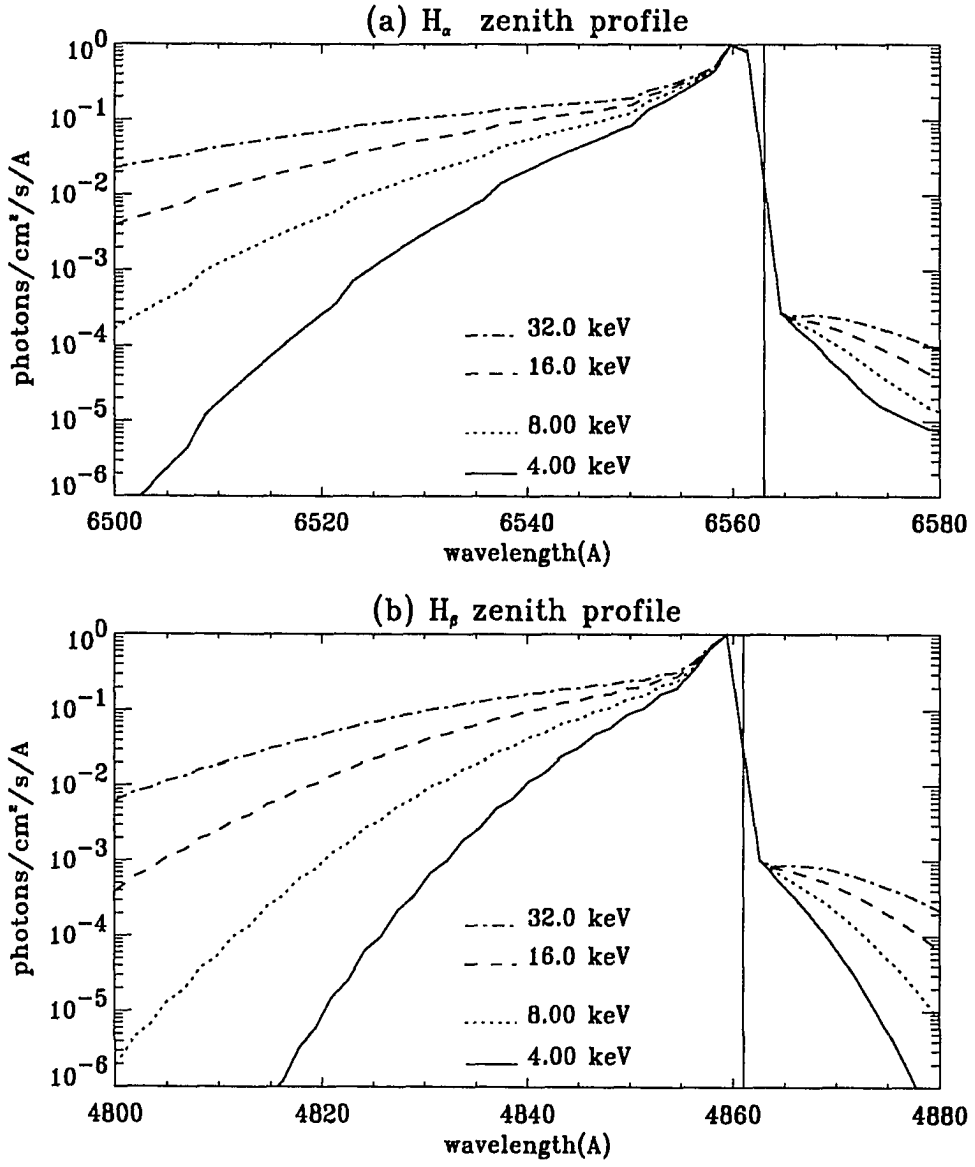

Figure 4.12: Normalized line profiles (in logarithmic scale) of H_α and H_β calculated from an input of Maxwellian proton spectra with different characteristic energies E_0 = 4.0, 8.0, 16.0, and 32.0 keV and an isotropic pitch angle distributions.

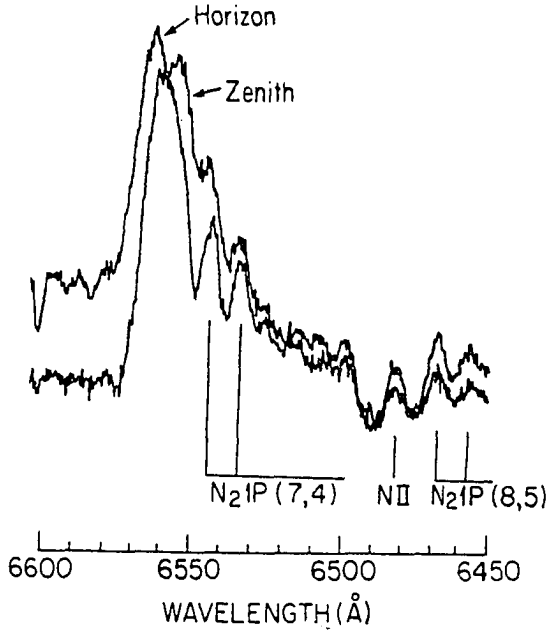

Figure 4.13: Experimental measurements of auroral hydrogen line profiles in the magnetic-zenith and -horizon directions. Curves are from Rees (1981).

where $\Delta\lambda$ is the bandwidth of the instrument. The bandwidth is a measure of the instrumental resolution, the larger the bandwidth $\Delta\lambda$, the lower the resolution of the instrument. Convolving equation 4.11 with the calculated line profile $\phi_z(\lambda_i)$ yields the profile that would be measured if the model is correct. Figure 4.14 shows the convolved line profiles for different instrumental resolutions. The solid line represents the non-broadened line . When the bandwidth of the instrumental transmission function increases from 0.0 to 10.0 Å the line width also increases, and the emission in the long wavelength wing of the unshifted line is visually comparable with the measurements shown in figure 4.13. The pitch angle effect was also studied by changing the pitch angle distributions of the input proton flux. The results showed that line profiles change very little with different pitch angle distributions. The reason is that mirror reflection is important high in the atmosphere, while the emission originates primarily in the lower atmosphere. However, if mirror reflection is eliminated from the transport equation, no emission will be obtained on the red

side of the unshifted line.

The comparison between figures 4.14(a) and 4.13 shows that the predicted profile on the long wavelength side of the unshifted line, after convolved with the instrument profile, is comparable to the observed. The mirror reflection can not be neglected in calculating auroral hydrogen emissions. However, the predicted profile on the blue side of the unshifted line disagrees with the observation.

(ii)Magnetic-horizon profiles

The magnetic-horizon in a converging magnetic field is defined as the direction for which the line of sight makes an angle of 90° with the field lines at about the height of the maximum of the hydrogen luminosity curve. The horizon profiles can be calculated in the same way as the zenith profiles except that the line-of-sight velocity now is: $v_s = v\sqrt{1-\mu^2}$. The line profiles for Maxwellian distributed input proton spectra with different characteristic energy E_0 are calculated and shown in figure 4.15. Similar to the magnetic zenith profiles, the magnetic horizon line profiles do not change much with the characteristic energy E_0, and the half width of the calculated horizon line profiles is very small compared with observed value. After being convolved with a triangular instrumental broadening function, the horizon line profiles are shown in figure 4.16 for different instrumental resolutions. An instrumental resolution of 10.0 Å about the resolution of the one meter Ebert-Fastie scanning spectrophotometer, gives a halfwidth for the calculated horizon profile of around 15 Å , comparable with that observed.

4.7 Comparison With Rocket Data

Using the model developed in this thesis, the predicted H_β emission is calculated and compared with observations acquired by a Norwegian rocket experiment in 1972 (Söraas et al., 1974). The rocket Proton I was launched from Andøya, Norway (69°18'N, 16°01'E), at 2329 UT (0020 local solar time), on February 13, 1972. The rocket reached a maximum height of 224 km and its altitude is known to an accuracy of 1 km throughout the flight. The field of view of the photometer on board the rocket was approximately 3° circular. The solid state detectors on board the rocket recorded both protons and hydrogen atoms so that the measurements represent the total H^+/H fluxes. The pitch angle distributions of protons measured by the

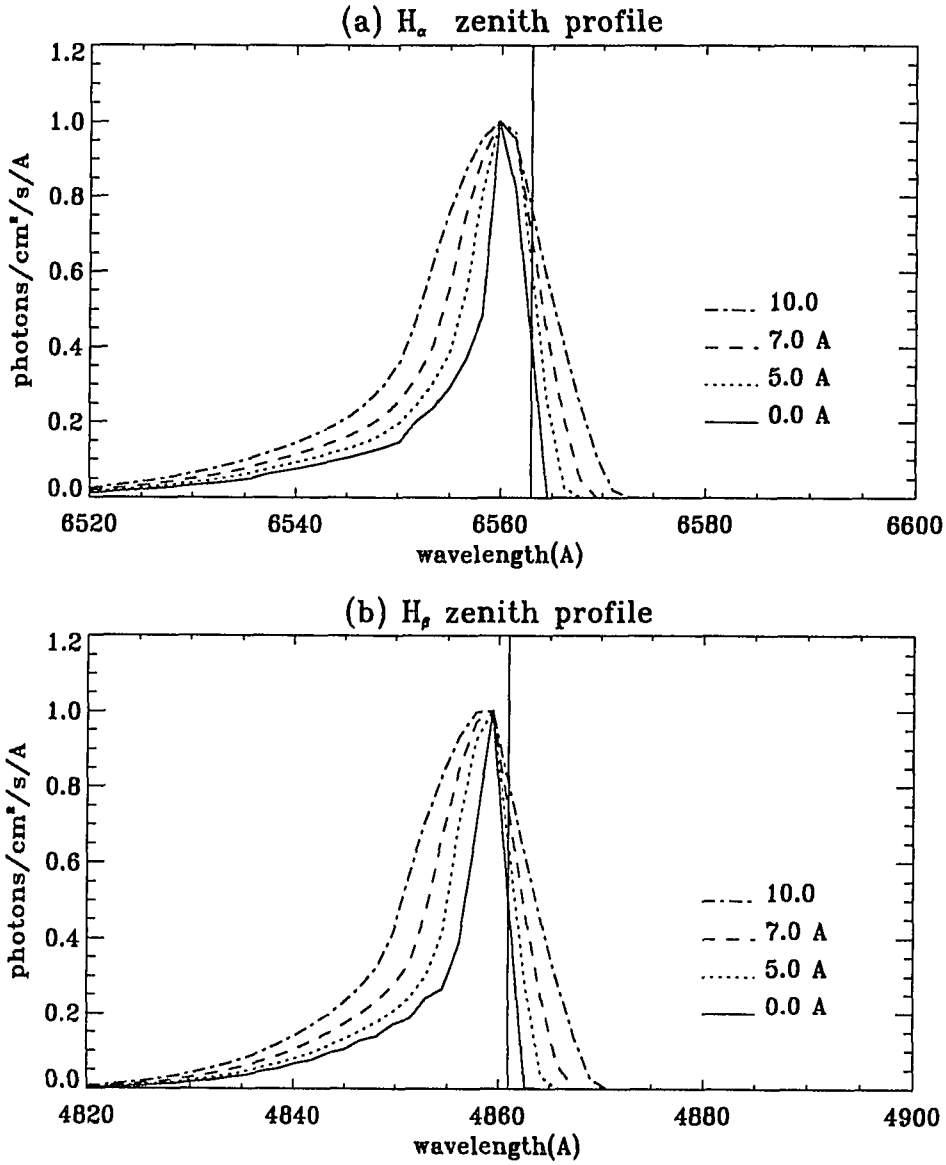

Figure 4.14: Predicted line profiles of H_α and H_β for instrument resolutions of 0.0, 5.0, 7.0, 10.0 Å , respectively. The input proton spectrum has a Maxwellian distribution of characteristic energy E_0=10.0 keV and an isotropic pitch angle distribution.

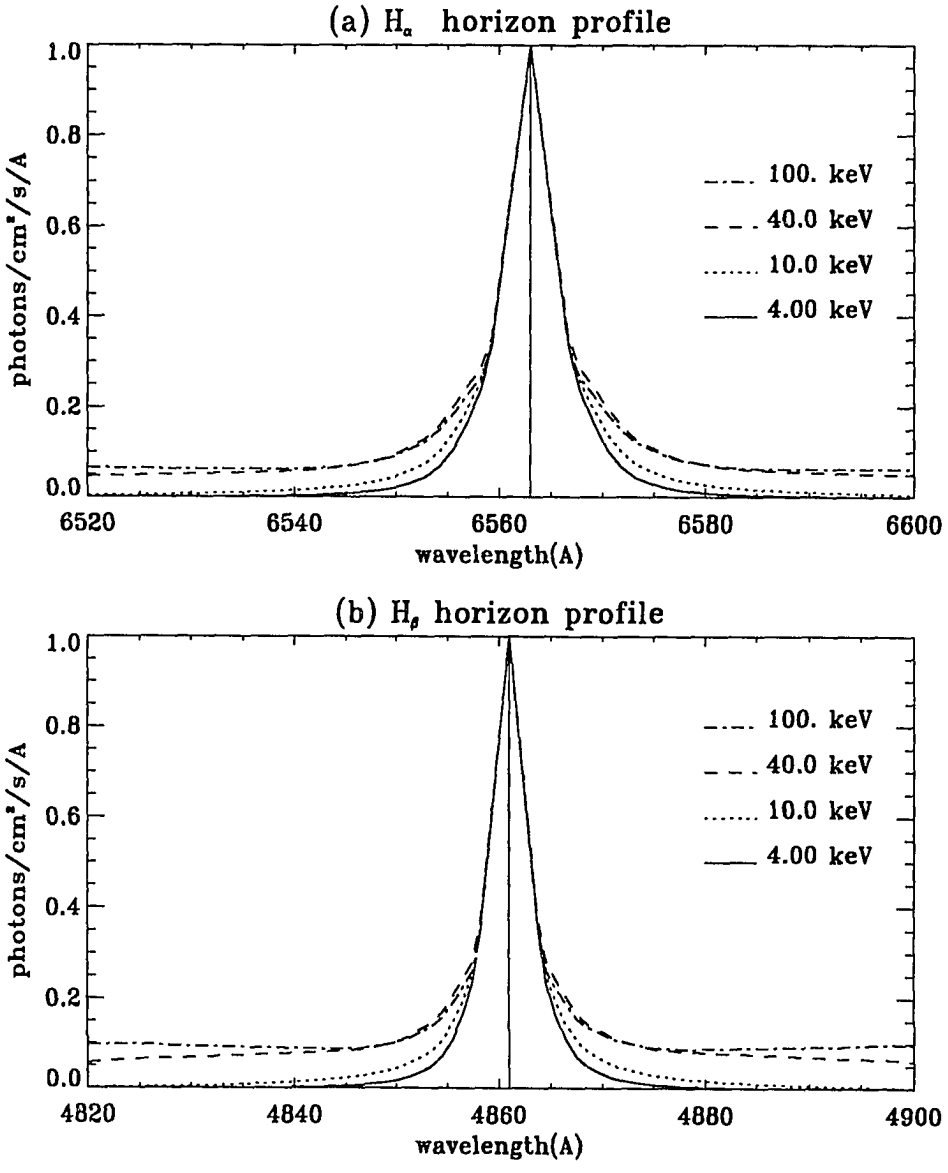

Figure 4.15: Horizon line profiles of H_α and H_β for Maxwellian input energy spectra with different characteristic energies E_0=4.0, 10.0, 40.0, and 100. keV. The pitch angle distribution is isotropic.

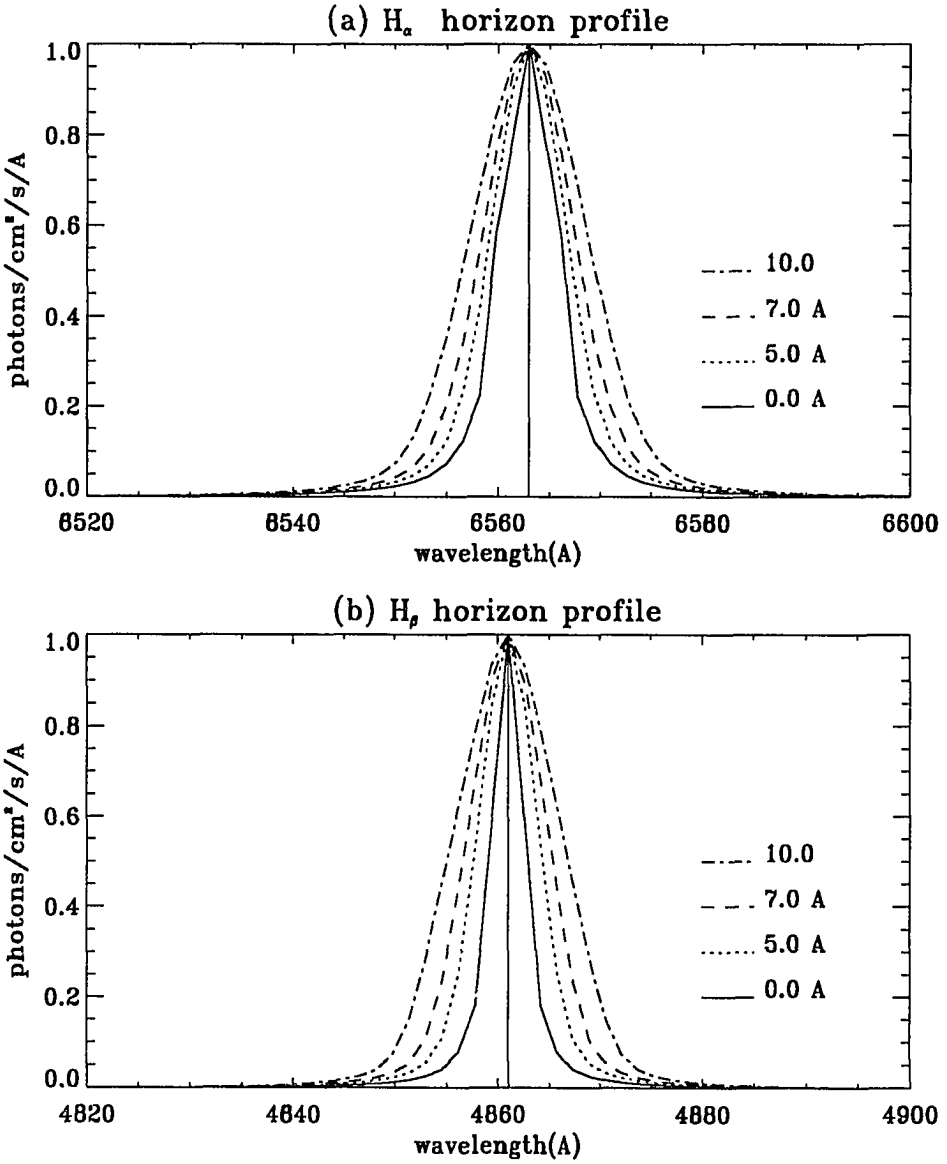

Figure 4.16: Predicted horizon line profiles of H_α and H_β for instrument resolutions of 0.0, 5.0, 7.0, 10.0 Å , respectively. The input proton spectrum has a Maxwellian distribution of characteristic energy E_0=10.0 keV and an isotropic pitch angle distribution.

detectors on board the rocket were isotropic. The particle flux was measured at 220 km. At this altitude protons should have reached an equilibrium distribution with hydrogen atoms. It is very difficult to estimate the input proton spectrum at the top of the atmosphere from the measured total proton and hydrogen atom flux at 220 km because energy degradation processes change the spectrum as protons reach this altitude. Söraas et al. (1974) converted the measured flux into the incident proton flux by using the extrapolated charge equilibrium fractions presented by Bernstein et al. (1969). The differential energy spectrum of protons converted to zero atmospheric depth is shown by the dotted line in figure 4.17. It can be fitted by the following analytical form (Söraas et al., 1974):

$$\frac{dj}{dE} = 8. \times 10^7 E^{-2} protons/cm^2\, s\, sr\, keV \quad for E \leq 100 keV \tag{4.12}$$

$$\frac{dj}{dE} = 2.2 \times 10^{17} E^{-6.67} protons/cm^2\, s\, sr\, keV \quad for E > 100 keV \tag{4.13}$$

This particle flux can be used as input at the top of the atmosphere to calculated the particle fluxes at all altitudes below.

4.7.1 Particle Flux Comparison

Using the proton differential energy spectrum from Söraas et al. (1974) (dotted line in figure 4.17) as input, H^+/H particle spectra are calculated at four altitudes at which measured particle spectra are shown in the Söraas et al. (1974) paper. These calculated spectra do not reproduce the observed values. The reason may be that the input proton spectrum was obtained by extrapolation without considering the energy degradation above 200 km. When particles undergo energy degradations, the spectrum will change. The proton spectra around 850 km measured by the NOAA 6 satellite show (Evans, 1989) a combination of Maxwellian and power law distributions. Using a proton spectrum that combines a Maxwellian and a power law distribution (solid line in figure 4.17) as input at 800 km, the particle fluxes at four different altitudes are calculated and compared with those measured by the proton I rocket detectors. The total input energy flux in the assumed proton spectrum is 2.46 ergs/$cm^2 s$. The integration of equations 4.12 and 4.13 gives a total input energy flux of 1.9 ergs/$cm^2 s$, while Söraas et al. (1974) reported that the total

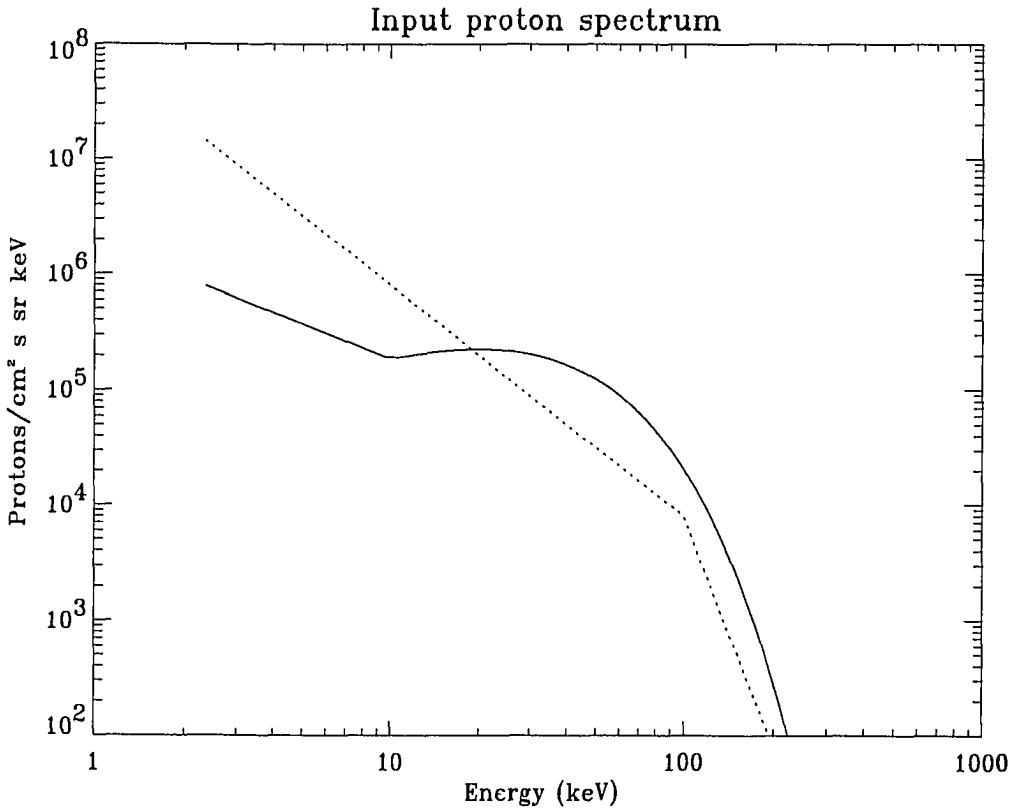

Figure 4.17: Input proton differential spectrum. The dotted line is the measured spectrum at 220 km corrected and for charge exchange to zero atmospheric depth, while the solid line is the inferred spectrum used in the calculations presented here.

energy flux carried into the atmosphere by protons of energies greater than 1 keV was 2.4 ergs/cm^2s. The computed H^+/H particle spectra are shown as solid lines in figure 4.18 at four altitudes with with measured H^+/H particle fluxes above 20 keV shown as diamonds. The comparisons show that the agreement above 20 keV is very good. Experimental data are not available for energies below 20 keV. One point worth mentioning is that in Söraas' paper, no distinction was made between protons and hydrogen atoms. The solid state detectors responded to the hydrogen atom flux as well as to the protons, so the measured particles were the sum of protons and hydrogen atoms.

4.7.2 Emission Intensity Comparison

The volume emission rate of H_β was calculated using the inferred proton differential spectrum (solid line in figure 4.17) as input. The integration of the volume emission rate over altitude gives the height profile of the emission intensity as shown in figure 4.19. The integrated H_β emission intensity observed by rocket Proton I is also shown in figure 4.19 for comparison with the model.

The input energy flux used in the numerical code is 2.46 ergs /cm^2s, yielding H_β emission of about 245 R. Therefore, the emission per unit energy flux is about 100R/(erg $cm^{-2}s^{-1}$). The measured total emission of H_β per unit energy flux is 180/2.4 = 75R/(erg $cm^{-2}s^{-1}$), smaller than the calculated 100R/(erg $cm^{-2}s^{-1}$). The beam spreading effect is not included in calculating the total emission. As shown in section 2.2, the H^+/H beam will spread with increasing atmospheric depth along the field line, due to charge exchange. Beam spreading reduces the proton intensity near the arc center, thus reduces the emission intensity of hydrogen atoms. For typical proton precipitation, the average energy of the input spectra is about 10.0 keV. From figure 2.4, a reduction factor of about 0.8 is expected for an arc width five times the scale height of the atmosphere. The calculated emission intensity of H_β line will be close to the measured value when the beam reduction factor is included in the calculation.

The average energy of the inferred proton differential energy spectrum is about 31 keV. The total emission per unit energy is estimated to be about 150R/(erg $cm^{-2}s^{-1}$) for a Maxwellian spectrum, from figure 4.7. The smaller emission per unit energy flux of 100R/(erg $cm^{-2}s^{-1}$) compared to 150R/(erg $cm^{-2}s^{-1}$) may be

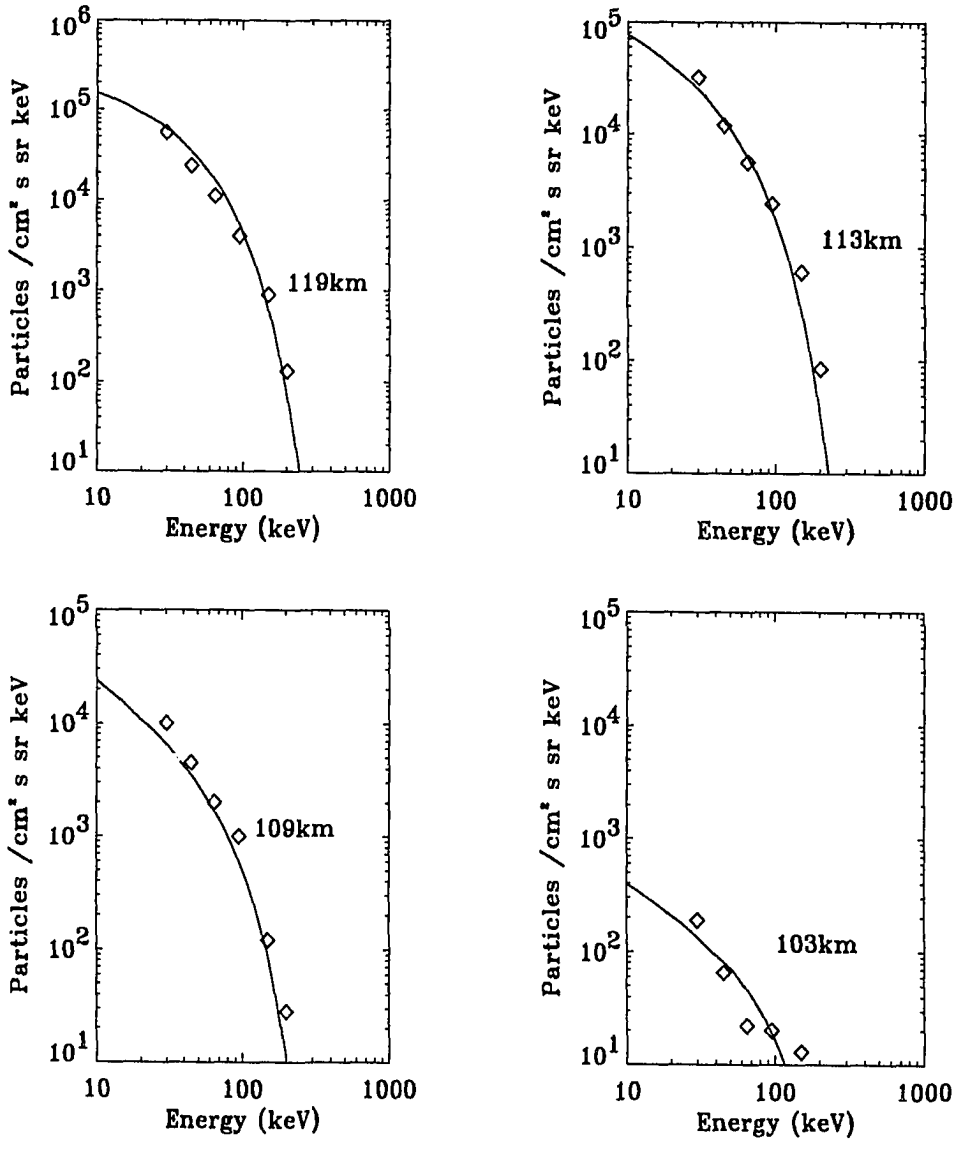

Figure 4.18: Comparison between measured and calculated particle differential intensities for energies above 20 keV at different altitudes. The solid lines show the calculated results and the diamonds show the rocket measured points.

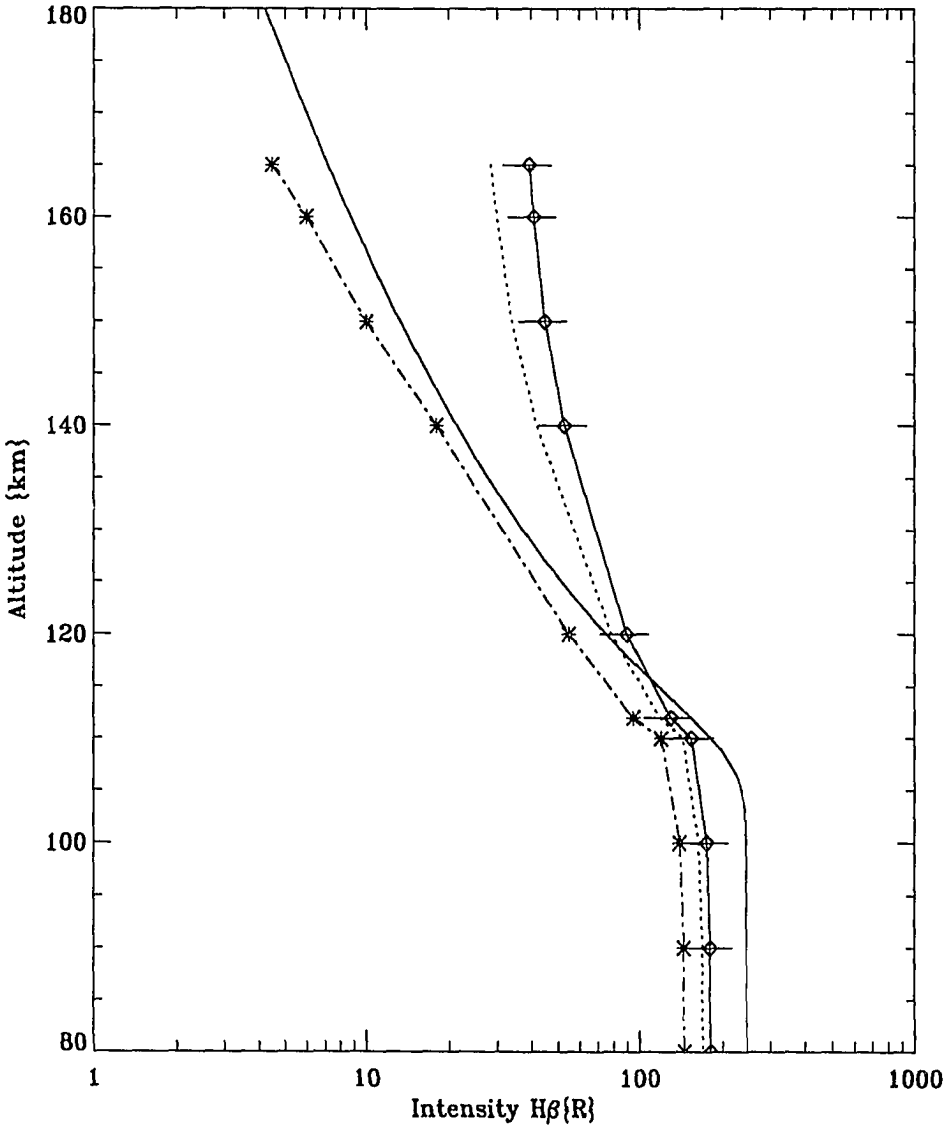

Figure 4.19: The predicted column emission rate is shown by the solid line and the diamonds ◇ show the rocket measurements. Dotted line is the height profile after subtracting 10R galactic contamination; $*$ is the height profile after subtracting 35R galactic contamination from the measured profile.

explained by noting that the input spectrum here is not Maxwellian.

As shown in figure 4.19, the calculated integrated emission intensity is larger than the measured value in the principal emission region. The larger calculated emission intensity may be explained by the beam spreading effect. However, above the maximum emission altitude, the calculated emission intensity is smaller than the measured one. The rocket measured height profile has a much larger slope than the calculated profile. The height profile of the hydrogen emission should be determined by the neutral gas scale height which has much smaller slope. Galactic contamination, which is independent of altitude, may contribute to the observed H_β height profile. Analysis of a sky map shows that the Milky Way, which is a strong galactic hydrogen emission source, was out of the rocket field of view. H_β emission from outside the galaxy is weak, of the order of 10R (Viereck, 1984). Subtracting this emission from the rocket measured height profile, a new height profile is obtained as shown by dashed line in figure 4.19. The new height profile has a smaller slope, but still larger than that of the calculated height profile. The galactic H_β could be larger than 10R (Montbriand et al., 1965), which would bring the measured profile in close agreement with the model results. For example, for a galactic background emission of 35R, the shape of the measured height profile is similar to the calculated one, as shown by the $*$ in figure 4.19. However, the galactic background H_β emission could not be so large because the instruments on board the rocket could not see the Milky Way during rocket flight period when viewing up the geomagnetic field. Therefore, although a correction of 35R for galactic contamination would have corrected the rocket data to agree with the calculations, this can not be justified, and the disagreement can not be resolved.

Chapter 5

Summary

A one dimensional, coupled H^+/H transport model is developed based on Boltzmann's kinetic equation. Proton and hydrogen atom transport through the atmosphere is described by separate but coupled equations. The coupled integro-differential transport equations are reduced to two coupled partial differential equations with the forward scattering approximation. A numerical code is developed to obtain particle fluxes as a function of altitude, energy and pitch angle for any specified incident proton flux. It is assumed that protons and hydrogen atoms can only lose energy in collisions but do not gain energy by any process.

A second order implicit numerical method is chosen to solve the coupled partial differential equations. Stability is maintained in this numerical scheme, regardless of the thickness of each layer; the efficiency and accuracy of the numerical scheme have proven to be very good. Since transport and energy degradation processes occur simultaneously, the thickness of each layer limits the choice of energy grid points. The energy grid point distribution is selected very carefully to avoid extrapolation for given altitude grid points in order to maintain energy conservation in the system. Energy is conserved to within 5% in the numerical scheme, but the accuracy of the results is determined by the accuracy of the input parameters in addition to the numerical scheme itself.

It has been suggested earlier that hydrogen emissions on the long wavelength side of the unshifted lines are produced by particles that have been magnetically

reflected back by the converging field lines. Earlier models, however, have not been able to reproduce the observed effects. In this thesis magnetic mirror reflection is included in the coupled proton and hydrogen atom transport equations to explain the observed optical emissions on the long wavelength side of the unshifted hydrogen atomic lines.

Both downward and upward particle fluxes are calculated as a function of altitude, energy and pitch angle. The altitude and energy profiles of particle fluxes show clearly the particle conversion process between protons and hydrogen atoms. Particle fluxes measured by instruments on board a rocket payload are well reproduced by the current transport model. Particle intensities are the fundamental quantities derived from transport equations. Energy deposition and ionization rates are calculated using the calculated particle fluxes. Charge stripping processes are included in the ionization calculation for the first time.

Numerical results show that mirror reflection does produce upward moving particles. The reflectivity is defined as the ratio of total reflected flux to total input flux at the top of the atmosphere. It is around 10% for isotropic pitch angle distributions and Maxwellian energy spectra. The reflectivity is a function of both pitch angle and energy of the input H^+ flux, but is more sensitive to the pitch angle distribution. The upward moving particles are responsible for the emissions on the long wavelength side of the unshifted hydrogen atomic lines.

Particle fluxes obtained from the numerical code are used to calculate the volume emission rates of hydrogen Balmer lines and first negative band emission of nitrogen molecules. The column emission rate which is the integration of the volume emission rate over altitude of H_β was calculated and compared with measured rocket data. A discrepancy at high altitudes can be resolved if a galactic component of about 35R is subtracted from the H_β profile measured on board the rocket. However, since the Milky Way was out of the rocket field of view during rocket flight period, such a large background H_β emission from outside the galaxy could not be justified and the disagreement remains unsolved.

The line profiles of H_α are calculated for comparison with observed profiles. The predicted profile on the long wavelength side of the unshifted line, when convolved with the instrument profile, compares well with a Doppler profile observed at the Poker Flat, Alaska, Optical observatory on 20 January 1977 (Rees, 1981), with

a one meter Ebert-Fastie scanning spectrophotometer. However, the blue shifted part of the predicted profile shows less blue shift than most observations. Since the observed Doppler profiles do not change much with different types of aurora, this observation is taken as representative for proton aurora. The numerical model is successful in explaining the red shift of the observed optical emission features of hydrogen atomic lines in proton precipitation and can be used as a working model to calculate ionospheric and thermospheric quantities in proton aurora. Following this work, an attempt could be made to couple the numerical model of proton transport with electron transport to solve the coupled electron, proton and hydrogen atom transport equations, and to develop a unified auroral theory to cover both electron and proton auroral emissions.

Appendix A

Inelastic Cross Sections of Neutral Species

The inelastic cross sections of neutral species under the impact of protons and hydrogen atoms are summarized in the following tables A.1 to A.3 for some specific energies.

Table A.1: H^+/H impact cross sections on N_2

E (keV)	σ_p^i (cm^2)	σ_p^{ex} (cm^2)	σ^{10} (cm^2)	σ_H^i (cm^2)	σ_H^{ex} (cm^2)	σ^{01} (cm^2)
1.0e-1	6.5e-18	2.0e-19	1.6e-17	1.5e-18	1.0e-18	9.0e-18
2.0e-1	1.4e-17	4.0e-19	6.0e-17	4.0e-18	2.0e-18	3.0e-17
4.0e-1	2.7e-17	8.5e-19	2.3e-16	1.1e-17	3.0e-18	7.3e-17
6.0e-1	4.0e-17	1.3e-18	4.0e-16	1.8e-17	5.0e-18	1.2e-16
1.0e+0	6.6e-17	2.0e-18	7.2e-16	3.5e-17	8.0e-18	1.6e-16
2.0e+0	1.1e-16	4.5e-18	1.1e-15	1.0e-16	1.0e-17	2.2e-16
4.0e+0	1.7e-16	8.5e-18	1.2e-15	2.5e-16	2.3e-17	2.7e-16
6.0e+0	2.3e-16	1.3e-17	1.2e-15	3.2e-16	2.1e-17	2.9e-16
1.0e+1	3.0e-16	2.1e-17	1.1e-15	4.0e-16	2.0e-17	3.2e-16
2.0e+1	4.3e-16	3.5e-17	9.0e-16	4.5e-16	1.2e-17	4.2e-16
4.0e+1	5.3e-16	4.8e-17	5.0e-16	4.4e-16	6.0e-18	4.8e-16
6.0e+1	5.6e-16	5.0e-17	2.9e-16	4.0e-16	3.5e-18	4.8e-16
1.0e+2	5.3e-16	4.5e-17	1.1e-16	3.2e-16	1.6e-18	4.6e-16
2.0e+2	4.2e-16	3.5e-17	1.3e-17	2.4e-16	5.0e-19	3.6e-16
4.0e+2	2.9e-16	2.2e-17	1.0e-18	1.7e-16	1.3e-19	2.5e-16
6.0e+2	2.2e-16	1.6e-17	3.5e-19	1.3e-16	7.0e-20	2.0e-16

Table A.2: H^+/H impact cross sections on O_2

E (keV)	σ_p^i (cm^2)	σ_p^{ex} (cm^2)	σ^{10} (cm^2)	σ_H^i (cm^2)	σ_H^{ex} (cm^2)	σ^{01} (cm^2)
1.0e-1	2.1e-18	1.2e-17	1.8e-15	8.0e-18	9.0e-18	8.0e-18
2.0e-1	4.6e-18	1.7e-17	1.7e-15	2.0e-17	1.2e-17	2.7e-17
4.0e-1	1.1e-17	2.4e-17	1.5e-15	3.7e-17	1.8e-17	6.0e-17
6.0e-1	1.7e-17	2.9e-17	1.3e-15	5.5e-17	2.1e-17	9.0e-17
1.0e+0	3.1e-17	3.7e-17	1.2e-15	8.0e-17	2.8e-17	1.2e-16
2.0e+0	5.7e-17	5.1e-17	1.1e-15	1.4e-16	3.9e-17	1.7e-16
4.0e+0	1.1e-16	7.1e-17	1.0e-15	2.1e-16	5.3e-17	2.3e-16
6.0e+0	1.5e-16	8.5e-17	9.5e-16	2.7e-16	6.4e-17	2.8e-16
1.0e+1	2.2e-16	1.0e-16	8.1e-16	3.1e-16	7.8e-17	3.2e-16
2.0e+1	3.6e-16	1.3e-16	5.9e-16	3.6e-16	9.5e-17	3.9e-16
4.0e+1	4.8e-16	1.4e-16	3.8e-16	4.2e-16	1.0e-16	4.4e-16
6.0e+1	5.3e-16	1.3e-16	2.6e-16	4.3e-16	9.7e-17	4.5e-16
1.0e+2	5.2e-16	1.1e-16	1.2e-16	3.5e-16	8.5e-17	4.4e-16
2.0e+2	4.2e-16	8.2e-17	2.2e-17	2.5e-16	6.1e-17	3.5e-16
4.0e+2	3.0e-16	5.4e-17	2.0e-18	1.6e-16	4.0e-17	2.9e-16
6.0e+2	2.3e-16	4.0e-17	5.0e-19	1.2e-16	3.0e-17	2.3e-16

Table A.3: H^+/H impact cross sections on O

E (keV)	σ_p^i (cm^2)	σ_p^{ex} (cm^2)	σ^{10} (cm^2)	σ_H^i (cm^2)	σ_H^{ex} (cm^2)	σ^{01} (cm^2)
1.0e-1	5.0e-19	5.0e-19	6.7e-16	6.0e-19	3.0e-18	5.0e-18
2.0e-1	1.3e-18	1.0e-18	6.2e-16	1.5e-18	5.0e-18	2.0e-17
4.0e-1	2.7e-18	2.1e-18	5.7e-16	3.3e-18	1.1e-17	4.5e-17
6.0e-1	4.3e-18	3.1e-18	5.4e-16	5.4e-18	1.7e-17	6.5e-17
1.0e+0	7.6e-18	5.2e-18	5.0e-16	6.0e-18	2.7e-17	1.0e-16
2.0e+0	1.6e-17	1.0e-17	4.6e-16	2.1e-17	4.9e-17	1.4e-16
4.0e+0	3.4e-17	2.0e-17	4.1e-16	4.5e-17	7.2e-17	1.8e-16
6.0e+0	5.2e-17	3.0e-17	3.9e-16	7.0e-17	7.6e-17	2.0e-16
1.0e+1	8.8e-17	4.8e-17	3.6e-16	1.1e-16	6.4e-17	2.5e-16
2.0e+1	1.7e-16	8.0e-17	3.2e-16	1.8e-16	3.8e-17	3.1e-16
4.0e+1	2.6e-16	9.5e-17	2.8e-16	2.0e-16	2.0e-17	3.5e-16
6.0e+1	2.9e-16	8.5e-17	1.7e-16	1.8e-16	1.4e-17	3.5e-16
1.0e+2	2.8e-16	6.1e-17	9.0e-17	1.4e-16	8.0e-18	3.4e-16
2.0e+2	2.0e-16	3.4e-17	2.2e-17	8.8e-17	4.0e-18	2.9e-16
4.0e+2	1.3e-16	1.7e-17	1.0e-17	5.3e-17	2.0e-18	2.1e-16
6.0e+2	9.6e-17	1.2e-17	6.0e-18	3.9e-17	1.3e-18	1.7e-16

Appendix B

Details of the Solutions to the Transport Equations

Transport equations 3.1 and 3.2 can be simplified by interpolating the off grid point intensities, such as $I_p(z, E + W^k_{s,p}(E), \mu)$, $I_H(z, E + W^k_{s,H}(E), \mu)$, to grid point intensities $I_p(z, E, \mu)$ and $I_H(z, E, \mu)$. Two point linear interpolation is applied to energy grid points to map the off-grid value of all intensities onto grid point values at all of the $E \times z$ grid points for each value of pitch angle μ as follows:

$$I_\beta(z, E_n + W^j_{s,\beta}(E_n), \mu) = \left[1 - \frac{W^j_{s,\beta}(E_n)}{\Delta E_n}\right] I_\beta(z, E_n, \mu) + \frac{W^j_{s,\beta}(E_n)}{\Delta E_n} I_\beta(z, E_{n+1}, \mu) \quad \text{(B.1)}$$

where β represents either proton or hydrogen atom, j represents different inelastic processes, and $\Delta E_n = E_{n+1} - E_n$ is the energy step size at point E_n. The energy step size ΔE_n is chosen so that interpolation is both optimized and minimized. The energy grid size is chosen such that for particles moving from altitude z_m to z_{m+1}, the energy loss due to all energy degradation processes will be smaller than the grid size $\Delta E_n = E_{n+1} - E_n$. The interpolation between energy grid points E_n and E_{n+1} can then be used. The procedure for establishing the energy and altitude grid points is given in the main text. The transport equations at a single energy E_n can be written using equation B.1.

$$
\begin{aligned}
\mu\frac{\partial I_p(z,E_n,\mu)}{\partial z} &= -\sum_s n_s(z)\Bigg\{\sigma_{s,p}(E_n) \\
&- \sum_k \sigma^k_{s,p}(E_n+W^k_s(E_n))\left(1-\frac{W^k_s(E_n)}{\Delta E_n}\right)\Bigg\} I_p(z,E_n,\mu) \\
&+ \sum_s n_s(z)\sum_k \sigma^k_{s,p}(E_n+W^k_s(E_n))\frac{W^k_s(E_n)}{\Delta E_n} I_p(z,E_{n+1},\mu) \\
&+ \sum_s n_s(z)\sigma^{01}_s(E_n+W^{01}_s(E_n))\left(1-\frac{W^{01}_s(E_n)}{\Delta E_n}\right) I_H(z,E_n,\mu) \\
&+ \sum_s n_s(z)\sigma^{01}_s(E_n+W^{01}_s(E_n))\frac{W^{01}_s(E_n)}{\Delta E_n} I_H(z,E_{n+1},\mu) \\
&+ \frac{(1-\mu^2)}{2B(z)}\frac{\partial B}{\partial z}\frac{\partial I_p(z,E,\mu)}{\partial \mu} \qquad \text{(B.2)} \\
\mu\frac{\partial I_H(z,E_n,\mu)}{\partial z} &= -\sum_s n_s(z)\Bigg\{\sigma_{s,H}(E_n) \\
&- \sum_k \sigma^k_{s,h}(E_n+W^k_s(E_n))\left(1-\frac{W^k_s(E_n)}{\Delta E_n}\right)\Bigg\} I_H(z,E_n,\mu) \\
&+ \sum_s n_s(z)\sum_k \sigma^k_{s,H}(E_n+W^k_s(E))\frac{W^k_s(E_n)}{\Delta E_n} I_H(z,E_{n+1},\mu) \\
&+ \sum_s n_s(z)\sigma^{10}_s(E_n+W^{10}_s(E_n))\left(1-\frac{W^{10}_s(E_n)}{\Delta E_n}\right) I_p(z,E_n,\mu) \\
&+ \sum_s n_s(z)\sigma^{10}_s(E_n+W_s10(E_n))\frac{W^{10}_s(E_n)}{\Delta E_n} I_p(z,E_{n+1},\mu) \qquad \text{(B.3)}
\end{aligned}
$$

Equations B.2 and B.3 are equivalent to equations 3.3 and 3.4 with the coefficients defined as follows:

$$
\begin{aligned}
A_p &= \sum_s n_s\left\{\sigma_{s,P}(E_n) - \sum_k \sigma^k_{s,p}(E_n+W^k_s(E_n))\left(1-\frac{W^k_s(E_n)}{\Delta E_n}\right)\right\} \qquad \text{(B.4)} \\
B_p &= \sum_s n_s(z)\sum_k \sigma^k_{s,p}(E_n+W^k_s(E_n))\frac{W^k_s(E_n)}{\Delta E_n} \qquad \text{(B.5)} \\
A_H &= \sum_s n_s(z)\sigma^{01}_s(E_n+W^{01}_s(E_n))\left(1-\frac{W^{01}_s(E_n)}{\Delta E_n}\right) \qquad \text{(B.6)} \\
B_H &= \sum_s n_s(z)\sigma^{01}_s(E_n+W^{01}_s(E_n))\frac{W^{01}_s(E_n)}{\Delta E_n} \qquad \text{(B.7)} \\
C_H &= \sum_s n_s\left\{\sigma_{s,H}(E_n) - \sum_k \sigma^k_{s,H}(E_n+W^k_s(E_n))\left(1-\frac{W^k_s(E_n)}{\Delta E_n}\right)\right\} \qquad \text{(B.8)}
\end{aligned}
$$

$$D_H = \sum_s n_s(z) \sum_k \sigma^k_{s,H}(E_n + W^k_s(E_n)) \frac{W^k_s(E_n)}{\Delta E_n} \tag{B.9}$$

$$C_P = \sum_s n_s(z) \sigma^{10}_s(E_n + W^{10}_s(E_n)) \left(1 - \frac{W^{10}_s(E_n)}{\Delta E_n}\right) \tag{B.10}$$

$$D_p = \sum_s n_s(z) \sigma^{10}_s(E_n + W^{10}_s(E_n)) \frac{W^{10}_s(E_n)}{\Delta E_n} \tag{B.11}$$

Equations B.2 and B.3 are regular partial differential equations. The intensities on both side of equations B.2 and B.3 are at the same energy E_n, the intensities at the higher energy E_{n+1} on the right hand side are the local boundary conditions. The task is to solve for intensities at energy E_n and altitude z for each pitch angle μ. The equations can be written in the following forms:

$$\frac{\partial I_p(z, E, \mu)}{\partial z} = F(I_p(z, E_n), I_H(z, E_n)) \tag{B.12}$$

$$\frac{\partial I_H(z, E, \mu)}{\partial z} = G(I_p(z, E_n), I_H(z, E_n)) \tag{B.13}$$

Where $F(I_p, I_H)$ and $G(I_p, I_H)$ are just two linear functions of $I_p(z, E, \mu)$ and $I_H(z, E, \mu)$. Applying second order implicit method to equations B.12 and B.13 yields:

$$I^{m+1}_p = I^m_p - \frac{1}{2}\Delta z_m \left\{F(I^m_p, I^m_H) + F(I^{m+1}_p, I^{m+1}_H\right\} \tag{B.14}$$

$$I^{m+1}_H = I^m_H - \frac{1}{2}\Delta z_m \left\{G(I^m_p, I^m_H) + G(I^{m+1}_p, I^{m+1}_H\right\} \tag{B.15}$$

where $\Delta z_m = z_{m+1} - z_m$ is the altitude grid size at point z_m. Equations B.14 and B.15 are two algebraic matrices. Solving the above two matrix equations yields the intensities I^{m+1}_p and I^{m+1}_H as function of intensities I^m_p and I^m_H, at previous altitude z_m. $m = 1$ corresponds to the boundary condition on the top of the atmosphere.

Bibliography

Bagariatskii, B. A., Soviet Astron. AJ (English Transl.)2, 87, 1958

Barat, M., J.C. Brenot, and J. Pommier, *Effect of u-g symmetry on direct and exchange excitations in ion-atom scattering*, J. Phys. B, 6, L105, 1973.

Basu, B., J.R. Jasperse, R.M.,Robinson, R.R. Vondrak, and D.S. Evans, *Linear transport theory of auroral proton precipitation: A comparison with observations*, J. Geophys. Res., 92,5920, 1987.

Basu, B., J.R. Jasperse, and N.J. Grossbard, *A Numerical solution of the coupled proton-H atom transport equations for the proton aurora*, J. Geophys. Res., 95, 19069, 1990.

Baudon, J., M. Barat, and M. Abignoli, *Differential scattering measurements on ion–atom collisions in the energy range 500–3000 eV I. He^+ - He collision*, J. Phys. B, 1, 1083, 1968.

Bennett, W.H. and E.O.Hulburt, *Magnetic self-focused ion streams as the cause of aurora*, J. Atm. Terr. Phys. 6, 200, 1954a

Bennett, W.H. and E.O. Hulburt, *Theory of aurora based on magnetic self-focusing of solar ion streams*, Phys. Rev. 95, 315, 1954b

Bernstein, W., G.T. Inouye, N.L. Sanders, and R.L. Wax, *Measurements of precipitated 1- to 20-keV protons and electrons during a breakup aurora*, J. Geophys. Res., 74, 3601, 1969.

Birely, J.H., *Formation of $N_2^+ B^2\Sigma_u^+$ and $N_2 C^3\Pi_u$ in collisions of H^+ and H with N_2*, Phys. Rev. A 10, 550, 1974.

Bray, A.V., D.S., Neuman, and E. Pollack, *Inelastic collisions in the $He^+ + H_2$ system at low-keV energies*, Phys. Rev.A, 15, 2261, 1977.

Carleton, N.P. and T.R. Lawrence, *Absolute cross sections for excitation of nitrogen by protons of a few keV energy*, Phys. Rev. 109, 1159, 1958.

Chamberlain, J.W., *The excitation of hydrogen in aurorae*, Astrophys. J., 120, 360, 1954a.

Chamberlain, J.W., *On the production of auroral arcs by incident protons*, Astrophys. J., 120, 566, 1954b.

Chamberlain, J.W., *Physics of the aurora and airglow*, Academic Press, NY, 1961.

Dahlberg, D.A., D.K. Anderson, and I.E. Dayton, *Optical emission produced by proton and hydrogen atom impact on nitrogen*, Phys. Rev. 164, 20, 1967.

Davidson, G.T., *Expected spatial distribution of low energy protons precipitated in the auroral zones*, J. Geophys. Res., 70, 1062, 1965.

Dose, V. and G. Sele, *Das elektronische Bremsvermögen von Stickstoff und Sauerstoff für niederenergetische Protonen*, Z. Phys. A, 272, 273, 1975.

Eather, R.H., *Red shift of auroral hydrogen profiles*, J. Geophys. Res., Vol.71, 5027, 1966.

Eather, R.H., *Secondary processes in proton aurora*, J. Geophys. Res., 72, 1481,1967a.

Eather, R.H, *Auroral Proton precipitation and hydrogen emissions*, Rev. Geophys., Vol. 5, 207, 1967b.

Edgar, B.C.,W.T. Miles, and A.E.S. Green, *Energy deposition of protons in molecular nitrogen and applications to the proton auroral phenomena*, J. Geophys. Res., 78,6595, 1973.

Edgar, B.C. H.S. Porter, and A.E.S. Green, *Proton energy deposition in molecular and atomic oxygen and applications to the polar cap*, Planet. Space Sci., vol.23, 787, 1975.

Evans, D.S., private communication, 1989.

Everhart, E., *Analysis of the He^+ on He collision*, Phys. Rev., 132, 2083, 1963

Flannery, M.R., *The binary encounter theory for general interaction*, J. Phys., B. 4, 892, 1971.

Fleischmann, H.H., C.F. Barnett, and J.A. Ray, *Small-angle scattering in stripping collisions of hydrogen atoms having energies of 1–10 keV in various gases*, Phys. Rev. A, 10, 569, 1974.

Galperin, Yu. I., *Proton bombardment in aurora*, Planetary Space Sci., 10, 187, 1963

Gao, R.S., L.K. Johnson, D.E. Nitz, K.A. Smith, and R.F. Stebbings, *Absolute differential cross sections for small angle elastic scattering in helium–rare-gas collisions at keV energies*, Phys. Rev. A, 36, 3077, 1987.

Gao, R.S., L.K. Johnson, D. A. Schafer, J.H. Newman, K.A. Smith, and R.F. Stebbings, *Absolute differential cross sections for small angle He^+ - He elastic and charge transfer scattering at keV energies*, Phys. Rev. A, 38, 2789, 1988.

Gao, R.S., L. K. Johnson, K. A. Smith, and R. F. Stebbings, *Collisions of keV energy H atoms with the rare gases: Absolute differential cross sections at small angles*, Phys. Rev. A 40, 4914, 1989.

Gao, R.S., L.K. Johnson, C.L. Hakes, K.A. Smith, and R.F. stebbings, *Collisions of kilo-electron-volt H^+ and He^+ with molecules at small angles: Absolute differential cross sections for charge transfer*, Phys. Rev. A, 41, 5929, 1990.

Green, A.E.S. and R.J. McNeal, *Analytical cross sections for inelastic collisions of protons and hydrogen atoms with atomic and molecular gases*, J. Geophys. Res., 76, 133, 1971.

Iglesias, G.E. and R.R. Vondrak, *Atmospheric spreading of protons in auroral arcs*, J. Geophys. Res., 79,280, 1974.

Jasperse, J.R. and B. Basu *Transport theoretic solutions for auroral proton and H atom fluxes and related quantities*, J. Geophys. Res., 87, 811, 1982.

Johansen, O.E. and A. Omholt, *Variations in the Doppler profile of H_α in aurorae*, Planet. Space Sci.,11, 1223, 1963

Johnson, L.K., R.S. Gao, K.A. Smith, and R.F. Stebbings, *Absolute differential cross sections for very-small-angle scattering of keV H and He atoms by H_2 and N_2*, Phys. Rev.A, 38, 2794, 1988.

Johnson, L.K., R.S. Gao, R.G. Dixson, K.A. Smith, N.F. Lane, and R.F. Stebbings, *Absolute differential cross sections for small-angle H^+ – He direct and charge-transfer scattering at keV energies*, Phys. Rev. A, 40, 3626, 1989.

Johnstone, A.D., *The spreading of a proton beam by the atmosphere*, Planet. Space Sci., 20, 192, 1972.

Lorents, D. C. and W. Aerth, *Elastic differential scattering of He^+ ions by He in the 20-600 eV range*, Phys. Rev. 139, A1017, 1965.

Lummerzheim, D., *Electron transport and optical emissions in the aurora*, Ph.D. thesis, University of Alaska, Fairbanks, December 1987.

Marchi, R.P. and F.T. Smith, *Theory of elastic differential scattering in low-energy He^+ + He collisions*, Phys. Rev., 139, A1025, 1965.

McDaniel, E. W., *Atomic collisions: Electron and photon projectiles*, John Wiley & Sons, Inc., 1989.

McNeal, R.J. and D.C. Clark, *Ionization and excitation of nitrogen by protons and hydrogen atoms in the energy range 1-25keV*, J. Geophys. Res., 74, 5065, 1969.

McNeal, R.J. and J.H. Birely, *Laboratory studies of collisions of energetic H^+ and hydrogen with atmospheric constituents*, Rev. of Geophys. and Space Phys., 11, 633, 1973.

Meredith, L.H., M.G. Fottlieg, and J.A. Van Allen, *Direct detection of soft radiation above 50 kilometers in the auroral zone*, Phys. Rev., 97, 201-5, 1955.

Miller, J.R. and B.A. Whalen, *Characteristics of auroral proton precipitation observed from sounding rockets*, J. Geophys. Res., 81, 147, 1976.

Montbriand, L.E.J., B.A. Tinsley, and A. Vallance Jones, *Galactic hydrogen as a hazard in auroral spectroscopy*, Can. J. Phys., 43, 782, 1965.

Nagy, S.W., S. M. Fernandez, and E. Pollack, *Small-angle charge exchange scattering of He^+ by He, Ne, and Kr at energies between 1.00 and 3.00 keV*, Phys. Rev. A 3, 280, 1971.

Newman, J.H., Y.S. Chen, K.A. Smith, and R.F. Stebbings, *Differential cross sections for scattering of 0.5-, 1.5-, and 5.0-keV hydrogen atoms by He, H_2, N_2, and O_2*, J. Geophys. Res., 91, 8947, 1986.

Nitz, D.E, R.S. Gao, L.K. Johnson, K.A. Smith, and R.F. Stebbings, *Absolute differential cross sections for very small angle elastic scattering in He + He collisions at keV energies*, Phys. Rev. A, 35, 4541, 1987.

Omholt, A., *The Optical aurora*, Springer-Verlag, New York, 1971.

Philpot, J. L., and R. H. Hughes, *Spectroscopic study of controlled proton impact on molecular nitrogen*, Phys. Rev., 133, A107, 1964

Potter, D., *Computational physics*, J. Wiley Comp., 1972.

Rees, M.H., *Spectroscopic diagnostic of the formation of auroral arcs*, Physics of Auroral arc formation, ed., S.-I. Akasofu and J. Kan, Geophysical Monograph Series, Vol. 25, 1981.

Rees, M.H., *On the interaction of auroral protons with the earth's atmosphere*, Planet. Space Sci., 30, 463, 1982.

Rees, M.H., *Physics and chemistry of the upper atmosphere*, Cambridge University Press, Cambridge, UK, 1989.

Rudd, M.E., *Energy and angular distributions of secondary electrons from 5–100 keV proton collisions with hydrogen and nitrogen molecules*, Phys. Rev. A, 20, 787, 1979.

Rudd, M.E., and D.H. Madison, *Comparison of experimental and theoretical electron ejection cross sections in helium by proton impact from 5 to 100keV*, Phys. Rev.A, 14, 128, 1977.

Rudd, M.E., and J.S. Risley, J. Fryar, and R.G. Rolfes, *Angular and energy distribution of electrons from 15- to 100-keV H^0 + He collisions*, Phys. Rev. A, 21, 206, 1980.

Rudd, M.E, D.H., Madison, and J.W. Gallagher, *Electron production in proton collisions: total cross sections*, Rev. of Modern Phys., 57, 965, 1985.

Rudd, M.E., Y.-K. Kim, D.H. Madison and T.J. Gay, *Electron production in proton collisions with atoms and molecules: energy distributions*, Rev. of Modern Phys., 64, 441, 1992.

Schowengerdt, F.D. and John T. Park, *Energy-loss spectra and collision cross sections for impact of 20-120keV positive ions on molecular nitrogen*, Phys. Rev. A, 1, 848, 1970

Sheridan, W.F., O. Oldenberg, and N.P. Carleton, *Excitation of nitrogen by fast protons and electrons*, J. Geophys. Res., 76, 2429, 1971.

Sigernes, Fred, Private communication, 1992

Singh, V., *Energy loss of protons in molecular oxygen*, Planet. Space Sci.,29, 261, 1981.

Singh, V. and R.P. Singhal, *Binary encounter calculations of proton energy deposition on N_2*, J. Geophys. Res., 83, 1655, 1978.

Söraas, F., H.R. Lindalen, K. Mäseide, S. Egeland, and A. Sten, *Proton precipitation and the H_β emission in a postbreakup auroral glow*, J. Geophys. Res., 79, 1851, 1974 .

Störmer, C., *The polar aurora*, Clarendon Pess, Oxford, 1955.

Swings, P., *Spectra of the night sky and of the aurorae*, Publ. Ast. Soc. Pacif. 60, 18-26, 1948.

Tanaka, Y., *Absorption spectrum of nitrogen in the region from 1075 to 1650Å*, J. Opt. Soc. Am. 45, 663, 1955.

Taulbjerg, Knud, *Electron capture and energy-gain spectroscopy*, AIP Conference Proceedings, Physics of Electronic and Atomic Collisions, XVI International Conference, New York, p. 273-9, 1990.

Thomas, E.W., *Excitation in heavy particle collisions*, John Wiley & Sons, Inc., 1972.

Thomas, E.W., G.D. Bent, and J.L. Edwards, *Cross sections for the formation of excited states in a nitrogen target by the impact of 0.15 -1.0keV protons*, Phys. Rev., 165, 32, 1968.

Urban, A., *Measurements of low energy auroral ions*, Planet. Space Sci., 29, 1353, 1981.

Vallance Jones, A., *Aurora*, D. Reidel Publ. Co., Dortrecht, Holland, 1974.

Van Zyl, B., *Charge-state equilibrated H^+/H flux fractions for analysis of the hydrogen aurora*, Rep. UAG R-265, Geophys. Inst., University of Alaska, College, 1978.

Van Zyl,B., and H. Neumann, *H_α and H_β emission cross sections for low energy H and H^+ collisions with N_2 and O_2*, J. Geophys. Res., Vol.85, 6006, 1980.

Van Zyl, B., H.Neumann, T.Q. Le, and R.C. Amme, *$H + N_2$ and $H + O_2$ collisions: Experimental charge-production cross sections and differential scattering calculations*, Phys. Rev. A, 18, 506, 1978.

Van Zyl, B., M.W. Gealy, and H. Neumann, *N_2^+ first-negative emission cross sections for low-energy H^+ and H impact on N_2*, Phys. Rev. A, 28, 2141, 1983.

Van Zyl, B., M.W. Gealy, and H. Neumann, *Prediction of photon yields for proton aurorae in an N_2 atmosphere*, J. Geophys. Res., 89, 1701, 1984.

Vegard, L., *Hydrogen showers in the auroral region*, Nature 144, 1089, 1939.

Vegard, L., Proc. I.U.G.G. Conf. in Oslo, 1948.

Viereck, R.A., *Pulsating aurora and its relationship to the H_β hydrogen emission*, M.S. thesis, University of Alaska Fairbanks, 1984.

von Engel, *Ionized gases*, Clarendon Press, Oxford, 1965.

Whalen, B.A., and I.B. McDiarmid, *Further low-energy auroral ion composition measurements*, J. Geophys. Res., 77, 191, 1972.

Würm, K., *Polarlichtspektrum und Natur der anregenden solaren Korpuskeln*, Z. Astrophys., 25, 28-57, 1948.

Yousif, F.B., J. Geddes, and H.B. Gilbody, *Balmer α emission in collisions of H, H^+, H_2^+ with N_2, O_2 and H_2O*, J. Phys. B, 19, 217, 1986.